

2008

# [PARTICLES IN EUROPE (PIE)]

-A workshop on the measurement and observation of suspended particles in coastal waters.

ISMAR-CNR  
Via Gobetti 101  
40129 Bologna  
Italy  
13-14 October 2008





# Particles in Europe (PiE) workshop

Mon-Tue 13-14 October 2008

Istituto di Scienze Marine (ISMAR) - ([Click for map](#))

Via Gobetti 101

40129 Bologna

Italy

## Monday 13 October 2008

9:00-9:30	Registration
9:30-10:10	OA Mikkelsen, YC Agrawal: Welcome, purpose of workshop, introduction to LISST technology
10:10-10:45	<b>X Casamitjana: Particle concentration in Lakes and Coastal zones: Case Studies.</b>
10:45-11:10	F. Gentile, T. Bisantino, R. Corbino, F. Milillo, G. Romano, G. Trisorio Liuzzi: Use Of An Infrared Light Sensor For Suspended Solids Monitoring In Rivers.
11:10-11:40	<i>Coffee</i>
11:40-12:05	M Guerrero: Field Measurements Of Suspended Sediment Transport With Acoustic Multi Frequencies Technique.
12:05-12:30	PD Thorne, R Meral: An assessment of the acoustic scattering properties of suspended sandy sediments and the implications for measuring suspension particle size and concentration.
12:30-12:55	BD Moate, PD Thorne: Measurements Of The Acoustic Backscattering Characteristics Of Sediment Suspensions Having Broad Particle Size Distributions.
12:55-13:20	D Doxaran, M Babin, K Ruddick, Y Park, M Fettweis: Tidal Variations Of Particle Size Distribution And Optical Properties In Turbid Coastal Waters. Perspectives For Ocean Colour Remote Sensing.
13:20-13:30	Discussion
13:30-14:30	<i>Lunch</i>
14:30-14:55	KM Braithwaite, DG Bowers.: A Comparison Of Predicted And Measured Scattering Of Light By Marine Particles.
14:55-15:20	TS Kostadinov, DA Siegel, S Maritorena: Determination Of The Particle Size Distribution Using Satellite Ocean Color Imagery: Applications And Assessment Of Uncertainty.
15:20-15:45	BD Moate: Measuring the Mass Specific Absorption Spectra of Organic Detritus.
15:45-16:05	<i>Coffee</i>
16:05-17:00	OA Mikkelsen: Technical presentation: Demo of new LISST-SOP software. LISST-100X, LISST-Portable, LISST-StreamSide and LISST-SL will be on display for hands-on experiences
20:00	<i>Dinner</i>



TURN THE PAGE







## A Comparison of Predicted and Measured Scattering of Light by Marine Particles

**KM Braithwaite<sup>1</sup>, DG Bowers<sup>1</sup>**

1. School of Ocean Sciences, University of Wales Bangor, Menai Bridge, Anglesey, United Kingdom LL59 2EY, k.m.braithwaite@bangor.ac.uk

Measurements of the specific scattering coefficient ( $b^*$ ) and particle size have been made in turbid coastal waters around the UK. Particle size spectra were measured using a LISST 100 while  $b^*$  data were obtained from a PRR (Profiling Reflectance Radiometer), a pair of Trios hyperspectral radiometers and a transmissometer. Comparisons were made of these three determinations of  $b^*$ , and the relationship between  $b^*$  and particle size has been investigated for varying particle size concentrations, distributions and densities.

Mie theory has also been used to compare the observed value of  $b^*$  with that predicted by applying scattering theory to the measured particle size spectra. The effect of the range of the particle sizes measured and the refractive index of the particles, on the scattering properties of the water have been investigated and the importance of the shape of the size distribution examined. Estimations have been made of the concentration of very small particles present and of their theoretical and actual contribution to the measured scattering. The density of flocs and their particle to water ratios have also been determined and the differences in their optical properties investigated.



## Particle concentration in Lakes and Coastal zones: Case studies

X Casamitjana<sup>1</sup>

1. Physics Department, University of Girona, Spain, xavier.casamitjana@udg.edu

Although the measurement of the particle concentration in lakes, or in marine environments, is an important parameter to estimate the water quality, only since few years ago the particle concentration is directly measured. Here we present three study cases where the laser instrument Lisst-100 was used to estimate the dynamic of particles in water environments.

### Case 1: The formation of an hydrothermal plume in a karstic Lake

A chronic hydrothermal turbid plume has been found to develop in the karstic Lake Banyoles. The lake is formed by 6 basins and the hydrothermal plume was located in the main basin of the Lake. Water enters the Lake by the underground and resuspends sediments up to a sediment interface, called the lutocline which separates the region of clean water above, from the high sediment concentration region below. The temperature of the water at the lutocline level is warmer than the hypolimnetic water immediately above and this difference in temperature generates the convection process that drives the hydrothermal plume. The plume develops upwards carrying a suspension of particles from the lutocline up to an equilibrium depth, i.e. forming a turbid hydrothermal plume. At the equilibrium depth, the water spreads laterally forming a turbidity current.

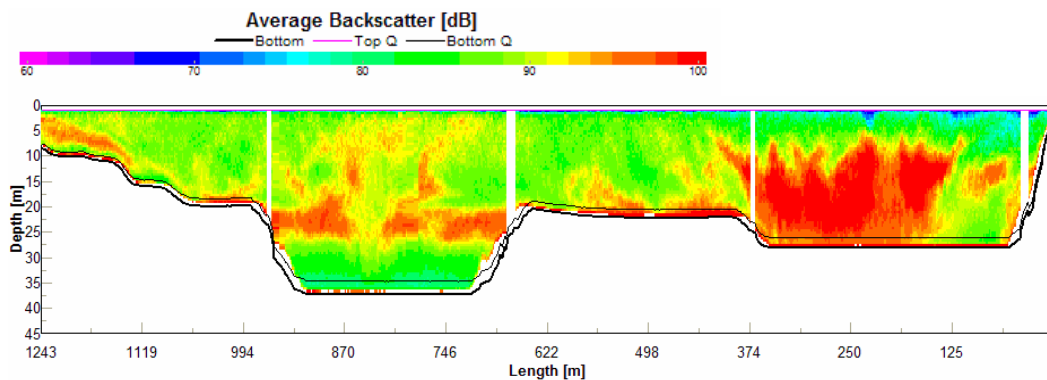


Figure 1: The average backscatter obtained with the ADCP illustrates the formation of the hydrothermal plume (see the red coloured zone)

### Case 2: A study of the evolution of a particle boundary layer in a reservoir, using laser particle sizing

A layer of particles was found at the bottom of Boadella reservoir from summer until the end of the year, when the reservoir was fully mixed. Most of the particles in this layer are remnants of the summer algae bloom and are trapped in the boundary layer due to the thermal stratification. The phytoplankton bloom is mainly composed of diatoms, with diameter  $d \approx 3 \mu\text{m}$  and green algae with diameter  $d \approx 15 \mu\text{m}$ . Inorganic particles and decomposed organic particles with  $d < 3 \mu\text{m}$  are also encountered in the boundary layer. On the other hand, particles with diameter between  $30 \mu\text{m}$  and  $100 \mu\text{m}$  are mostly found in the epilimnion of the reservoir. These are a mixture of aggregates of inorganic particles, colonies of phytoplankton, zooplankton, detritus, etc. Different mixing events occurring during autumn resuspended the small particles in the boundary layer, while

the greater particles settled down. The extent of the resuspension has been parameterized with a non-dimensional number that balances the stress across the interface and the strength of the stratification.

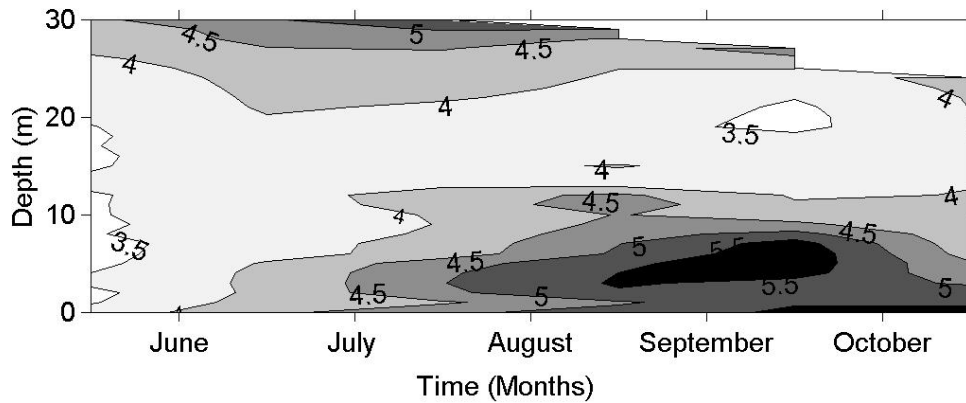


Figure 2: Isolines of Particle concentration in Boadella reservoir. The isolines refer to log-contours

### Case 3: Particle resuspension in a marine environment

The role of the flow field on the horizontal and vertical distributions of different phytoplankton populations thriving in the water column of a shallow coastal ecosystem has been analyzed. Two extreme flow conditions are illustrated. The first was a low energetic flow, under calm meteorological conditions and a stratified temperature of the water column. The second flow, coincident with the passage of a storm front, was more energetic resulting in increased mixing that homogenized the temperature in the whole water column.

Although the mixing level homogenized the temperature of the water column in the high-energy period, it was not enough to homogenize the temperature in the low-energy period. In contrast, in both periods, the mixing level was enough to homogenize the vertical distribution of particles. A decrease in the concentration of particles from the calm period to the high-energy period was attributed to an advection event with warmer water of lower plankton concentration that resulted in a decrease of the total concentration of suspended particles in the water column.

### References

Colomer, J, Serra, T., Piera, J., Roget, E. and Casamitjana, X. Observations of an hydrothermal plume in a karstic lake. *Limnology and Oceanography*. 46 (1), 197-203, 2001.

Casamitjana, X., Serra, T., Soler, M., Colomer, J. *Water Research*. Vol: 36 (17), 4293-4300, 2002

Serra, T., T. Granata, J. Colomer, A. Stips, F. Møhlenberg and X. Casamitjana. The Role of Advection and turbulent Mixing in the Vertical distribution of Phytoplankton. *Estuarine, Coastal and Shelf Science*, 54, 2002

**Tidal variations of particle size distribution and optical properties in turbid coastal waters:  
Perspectives for ocean colour remote sensing.**

David Doxaran<sup>1</sup>, Marcel Babin<sup>1</sup>, Kevin Ruddick<sup>2</sup>, Younge Park<sup>2</sup> and Michael Fettweis<sup>2</sup>

1. Laboratoire d'Océanographie de Villefranche, UMR 7093 - CNRS / UPMC, Villefranche-sur-Mer, France, doxaran@obs-vlfr.fr
2. Management Unit of the North Sea Mathematical Models (MUMM, BMM, UGMM, RBINS, Brussels, Belgium

Measurements of surface water turbidity, inherent optical properties (IOPs), suspended particle concentration and size distribution were carried out in Belgian coastal waters during a 12 hours tidal cycle. The IOPs (namely the light absorption, attenuation and scattering coefficients) were measured using a Wetlabs field spectrophotometer designed with three visible and six near-infrared spectral channels, and a short pathlength appropriate for turbid coastal waters. Particle size distributions were measured using a LISST-100X (Sequoia Scientific). Additional measurements provided by field (temperature, salinity, water depth, current velocities and seawater reflectance) and ocean colour satellite (MODIS<sup>1</sup> and SEVIRI<sup>2</sup>) data are used to describe the dynamics of the study area

Results show a clear 6-hour cycle in parameters related to suspended matter concentrations, i.e. water turbidity, light absorption, attenuation and scattering coefficients. Moreover, the spectral slopes of the attenuation and scattering coefficients, expected to be particle size-related, also exhibit variations indicating particle sorting over the tidal cycle, i.e. settling of coarse particles at slack tide and resuspension at mid-tides.

We first analyze how the spectral variations of the IOPs reflect changes in the shape of the particle size distribution. Based on bio-optical modelling and field measurements, we then determine how changes in the shape of the particle size distribution can be detected from the seawater reflectance. We finally discuss the potential of ocean colour remote sensing data in order to retrieve information on the size of particles suspended in turbid coastal waters.

---

<sup>1</sup> Moderate Resolution Imaging Spectroradiometer

<sup>2</sup> Spinning Enhanced Visible and InfraRed



# Uncertainty Of Excess Density And Settling Velocity Of Mud Floes Derived From In Situ Measurements.

Michael Fettweis<sup>1</sup>

1. Royal Belgian Institute of Natural Science, Management Unit of the North Sea Mathematical Models, Gulledele 100, 1200 Brussels, Belgium, m.fettweis@mumm.ac.be

## 1. Introduction

Flocculation is the process of floc formation and break-up and has a direct impact on settling velocity. The settling velocity is a function of the particle size and effective density, and can be described by Stokes' law under the assumption that the particle Reynolds number is smaller than one and that the particles are spherical and non porous. However, because the Suspended Particulate Matter (SPM) consists of a population of floes with heterogeneous sizes, density, and shape, the settling velocity of mud floes in real environments may vary. Experimental observations are always subject to uncertainties that can be typically attributable to random measurement errors (lack of precision), systematic errors (lack of accuracy), human error, and intrinsic variable stochasticity.

Within the field of flocculation of cohesive sediment dynamics, stochastic uncertainty is of primary importance as recently recognised in the works by Lee and Matsoukas (2000), Jackson (2005), Khelifa and Hill (2006) and Maggi (2007) who studied the fluctuations of the average and median floc size over time. Measurements of effective density and settling velocity are inherently associated with uncertainties (errors). These are linked with a lack of accuracy of the measuring instruments, a lack of precision of the observations and the statistical nature of the variables (floc size, primary particle size and primary particle density). When using observations some understanding of the uncertainties is needed.

Based on the theory of error propagation the error of the effective density and the settling velocity of mud floes has been estimated using the measurement data of OBS, SPM filtration, LISST100C, CTD and Sedigraph. The measurements have been carried out between 2003 and 2005 in the southern North Sea during 8 tidal cycles, (Figure 1). An extended presentation of the results can be found in Fettweis (2008).

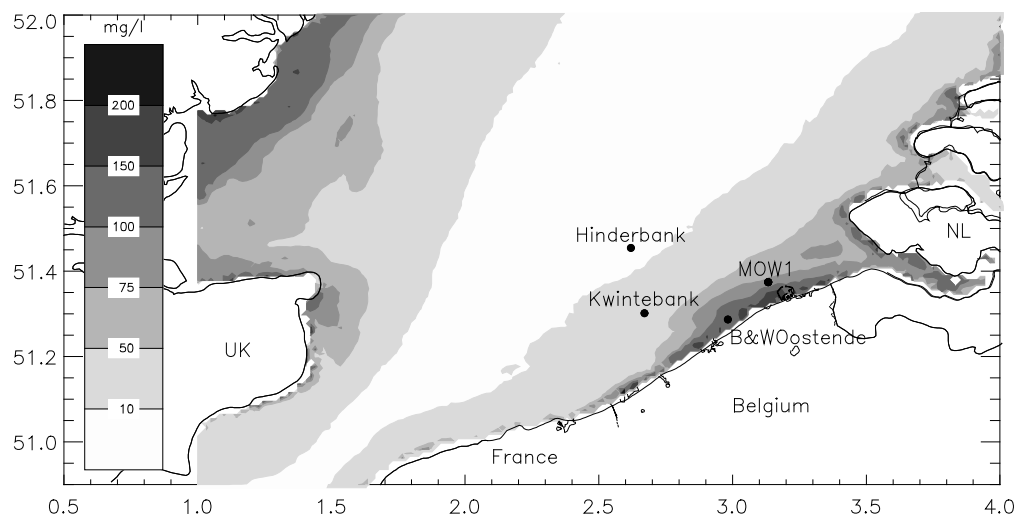


Figure 1: Yearly averages of vertically averaged SPM concentration in the southern North Sea derived from 362 SeaWiFS images (1997-2004), see Fettweis et al. (2007). Also shown are the locations of the tidal measurement stations. The coordinates are latitude (°N) and longitude (°E).

## 2. Calculation of fractal dimension, effective density and settling velocity

By describing mud floes with the fractal theory (Meakin, 1991, Van Leussen, 1994), the floc effective density can

be written as (Kranenburg, 1994):

$$\rho = \rho_f - \rho_w = (\rho_p - \rho_w) \left[ \frac{D_f}{D_p} \right]^{nf-3} \quad (1)$$

where  $\rho$  is the effective density;  $\rho_f$ ,  $\rho_w$ , and  $\rho_p$  are the floc, water, and primary particle densities, respectively;  $D_f$  and  $D_p$  are the floc and primary particle sizes, respectively, and  $nf$  is the floc fractal dimension. The primary particle is defined as the first-order constituent of a floc and may consist of clay or other silicate minerals, carbonate and organic particles.  $D_p$  can be represented by the median diameter of mineral grains in the flocs. Because  $\rho_p$ ,  $\rho_w$  and  $D_p$  can be considered independent variables, Eq. 1 can be reduced to

$$\rho = k_a D_f^{nf-3} \quad (2)$$

with  $k_a$  a correlation parameter. If  $\rho$  and  $D_f$  are known then the fractal dimension can be derived using a linear regression on a log-log plot. By doing so, it is assumed that  $nf$  is constant, this assumption has recently been questioned (e.g. Khelifa and Hill, 2006; Maggi et al., 2007 and Maggi, 2007). The effective floc density can be calculated if the floc and water density are known (see Mikkelsen and Pejrup, 2001). The water density has been derived from conductivity, temperature, and pressure measured by the CTD. The floc density can be expressed as:

$$\rho_f = \frac{M_f}{V_f} \quad (3)$$

with  $V_f$  the floc volume and  $M_f$  the floc mass concentration per unit volume. The water and primary particle mass can be written as  $M_w = \rho_w V_w$  and  $M_p = \rho_p V_p$ , respectively, with  $V_w$  and  $V_p$  the water and primary particle volumes in the floc. The floc density (Eq. 3) can eventually be calculated with  $M_f$  written as:

$$M_f = M_p + M_w = M_p + \rho_w (V_f - V_p) = M_p + \rho_w \left( V_f - \frac{M_p}{\rho_p} \right) \quad (4)$$

The fall velocity,  $w_s$ , for flocs with fractal structure can be written as (Winterwerp, 1998):

$$w_s = \frac{\alpha}{18 \beta} \frac{(\rho_p - \rho_w)}{\eta} g D_p^{3-nf} \frac{D_f^{nf-1}}{1 + 0.15 \text{Re}^{0.687}} \quad (5)$$

where  $\text{Re}$  is the floc-Reynolds number,  $g$  is the gravitational acceleration,  $\eta$  is the molecular viscosity of water ( $\approx 1.4 \times 10^{-3}$  kg/ms), and  $\alpha$  and  $\beta$  are shape factors.

$M_p$  has been measured with an OBS and through filtration;  $V_f$  and  $D_f$  have been measured with a LISST 100C and  $D_p$  with a Sedigraph. In Figure 2 typical distributions of  $D_f$  measured with the LISST 100C are shown. The density of primary particles,  $\rho_p$ , has been calculated, based on an analysis of the floc constituents. The density was obtained from the primary particle size distribution and the  $\text{CaCO}_3$  and total organic content (TOC) content. In figure 3 primary particle size distribution measured of the mineral fraction by the Sedigraph are presented. The fractal dimension was derived from a linear regression on a log-log plot of effective density and floc size.

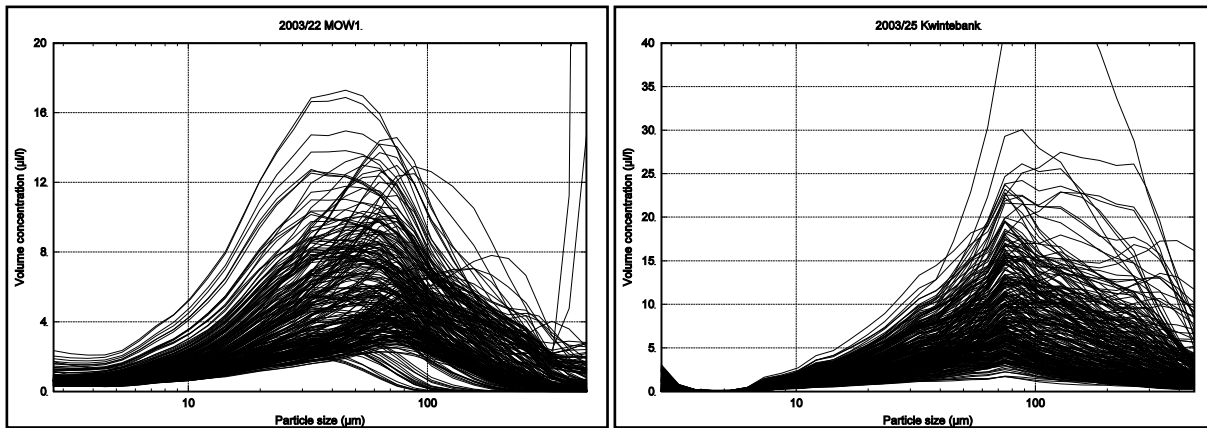


Figure 2: Particle (floc) size distribution of the SPM measured by the LISST 100C as a function of volume concentration. Only the distributions with a transmission greater than 20% are shown.

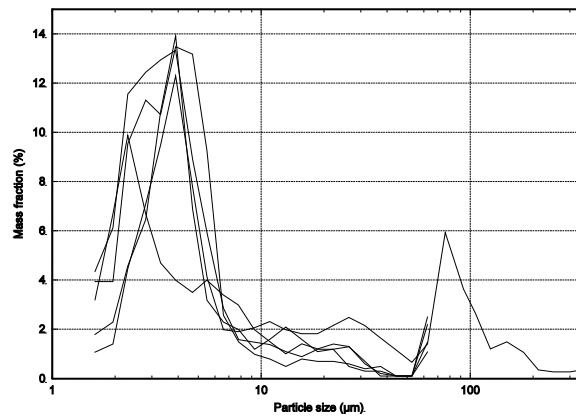


Figure 3: Primary particle size distribution of the mineral fraction of the SPM measured with a Sedigraph 5100 and sieving. The rising tail at 62.5 µm in 4 out of 5 spectra comprises the sand fraction without further detail.

### 3. Estimates and origin of uncertainties

The errors have been estimated based on the theory of error propagation (see e.g. chapter 14.2 of Numerical Recipes, Press et al., 1989). The results indicate that major sources of uncertainties are from the primary particle and floc sizes, the primary particle density, and the SPM concentration from filtration and from OBS. The relative standard deviations for effective density, fractal dimension and settling velocity are about 10%, 2.5% and 100%, respectively. These uncertainties should rather be regarded as lower limits of the real error, because the errors due to lack of accuracy of the OBS, LISST and Sedigraph have been omitted as they are unknown.

The origin of the error on the settling velocity is mainly due to uncertainties on the primary particle size  $D_p$  and the floc size  $D_f$ . These results are complementary to those of Khelifa and Hill (2006), who have underlined the dominant effect that primary particle size has on the effective density and thus on the settling velocity. The results from the error analysis have shown that the statistical uncertainties on the settling velocity will always be high when dealing with natural flocs or particles and that they cannot be reduced by increasing the accuracy of the instruments, the way of measuring or the method to calculate the settling velocity. In other words, they are always the dominating ones. These actions will however increase the reliability of the settling velocity – in the sense that the value corresponds better with reality - as systematic errors are reduced or precision is increased.

### 4. Conclusions

Measurements of settling velocity are inherently associated with uncertainties due to lack of accuracy of the

measuring instruments and due to the statistical nature of particle size distributions (and effective densities) in the suspended matter. These errors occur when using direct or indirect method to obtain settling velocities, the conclusions are:

- (1) The relative standard deviation on settling velocity due to statistical uncertainties is minimum 100%. The origin of the error is mainly from uncertainties of the primary particle and the floc sizes, respectively. These statistical uncertainties will always be high when dealing with natural flocs or particles and cannot be reduced by increasing the accuracy of the instruments;
- (2) The statistical error on the effective density is mainly due to uncertainties of the SPM concentration and of the primary particle density;
- (3) More reliable values of settling velocity can be obtained by e.g. increasing the precision of the measurements, the accuracy of the instruments and not assuming self-similarity of floc structures;
- (4) It is crucial to have data on primary particle size and density at the same moment as floc size and SPM concentration data, as these parameters are of major importance to calculate the effective density and the settling velocity. Measurements of suspended matter should include an analysis of its major constituents (organic matter,  $\text{CaCO}_3$  and silicate minerals) and the grain size.

An important part of our understanding of flocculation and cohesive sediment dynamics (deposition and erosion) is based on measurements. The uncertainties associated with indirect (or direct) settling velocity measurements are very high due to their statistical nature; the total error will be even higher because systematic errors due to a lack of accuracy of the measuring instruments are not included.

## References

- Fettweis, M., Nechad, B., Van den Eynde, D. 2007b. An estimate of the suspended particulate matter (SPM) transport in the southern North Sea using SeaWiFS images, in situ measurements and numerical model results. *Cont. Shelf Res.* 27: 1568-1583.
- Fettweis, M. 2008. Uncertainty of excess density and settling velocity of mud derived from in situ measurements. *Est., Coast. Shelf Sci.*, 78, 426-436.
- Jackson, G. A. 2005. Coagulation theory and models of oceanic plankton aggregation. In: *Flocculation in Natural and Engineered Environmental Systems*. Droppo, I., Leppard, G., Liss, S., Milligan, T. (eds.). CRC Press, 271-292.
- Khelifa, A., Hill, P.S. 2006. Models for effective density and settling velocity of flocs. *J. Hydr. Res.* 44: 390-401.
- Kranenburg, C. 1994. On the fractal structure of cohesive sediment aggregates. *Est. Coast. Shelf Sci.* 39: 451-460.
- Lee, K., Matsoukas, T. 2000. Simultaneous coagulation and break-up using constant-N Monte Carlo. *Powder Techn.* 110, 82-89.
- Mikkelsen, O.A., Pejrup, M. 2001. The use of a LISST-100 laser particle sizer for in-situ estimates of floc size, density and settling velocity. *Geo-Mar. Let.* 20: 187-195.
- Maggi, F. 2007. Variable fractal dimension: a major control for floc structure and flocculation kinematics of suspended cohesive sediments. *J. Geoph. Res.* 112, C07012.
- Maggi, F., Mietta, F., Winterwerp, J.C. 2007. Effect of variable fractal dimension on the floc size distribution of suspended cohesive sediment. *J. Hydr.* 343: 43-55.
- Meakin, P. 1991. Fractal aggregates in geophysics. *Rev. Geophys.* 29: 317-354
- Press, W.H., Flannery, B.P., Teukolsky, S.A., Vetterling, W.T. 1989. *Numerical recipes: The art of scientific computing (Fortran Version)*. Press Syndicate of the University of Cambridge, 702pp.
- van Leussen, W. 1994. *Estuarine macroflocs and their role in fine-grained sediment transport*. Ph. D. Thesis, Univ. Utrecht, The Netherlands.
- Winterwerp, J. 1998. A simple model for turbulence induced flocculation of cohesive sediments. *J. Hydr. Res.* 36: 309-326.

## USE OF AN INFRARED LIGHT SENSOR FOR CONTINUOUS SUSPENDED SOLIDS MONITORING IN RIVERS

F. Gentile, T. Bisantino, R. Corbino, F. Milillo, G. Romano, G. Trisorio Liuzzi

1. PROGESA Department, University of Bari, Via Amendola 165/A Bari-Italy

### Introduction

Erosion and solid transport are particularly important in the north-western area of Puglia Region (Southern Italy), where the main watersheds are located: Candelaro (1777.9 km<sup>2</sup>), Cervaro (539.2 km<sup>2</sup>), Carapelle (714.9 km<sup>2</sup>) and Ofanto (2702.8 km<sup>2</sup>).

In the study area the sediment transport processes were monitored by the National Hydrographic Service and largely consisting of suspended materials, with top concentrations reaching 90 g/l. The measurements, available from 1933 to 1989, were later interrupted.

In order to measure in continuous the suspended sediment concentration, an experimental station was set up in the Carapelle torrent (basin area=506 km<sup>2</sup>, fig. 1) (Bisantino et al., 2006). The station is equipped with a dual function infrared sensor (turbidity/suspended solids), a remote data acquisition system, an electromechanical and an ultrasound stage meter.

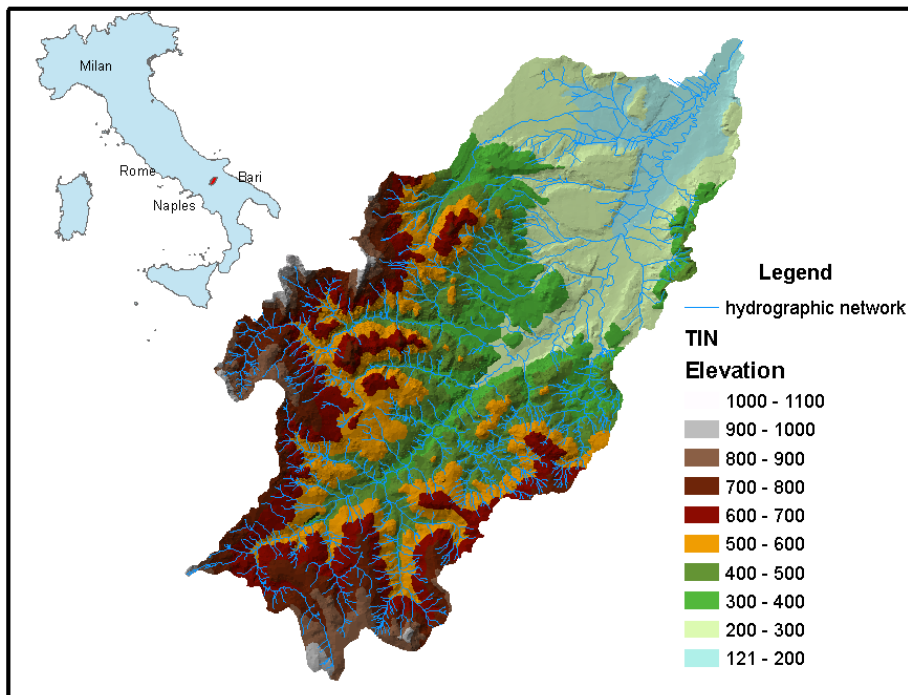


Figure 1. Watershed of the Carapelle torrent.

The instrument was tested in the laboratory using mixtures of different grain size distributions and sediment concentrations. The aim was to determine the existing relationship between the optical and the gravimetric data and to assess how the instrument responded to the varying granulometric content of the mixtures. Afterwards, the instrument was field-tested to verify, through a calibration stage, the housing device and the relationship between the optical sediment concentration and that measured in the laboratory from samples collected during flood events.

## Materials and methods

### *Station measuring suspended sediment concentration*

The experimental station measuring suspended sediment concentration (fig. 2) is located in the Carapelle (Ortona-Castelluccio dei Sauri bridge), one of the main rivers in Puglia Region. It originates from flyschoid formations of the Daunia Mountains and develops into the alluvial fan of the Tavoliere plain. The plain and the low hilly areas are mainly used for olive growing, whereas the higher slopes are occupied by woods and pasture. The climate is typically Mediterranean, with rainfalls ranging from 450 to 800 mm/year and average temperatures ranging from 10 to 16 °C.



Figure 2. Sediment transport measuring station, optical probe housing (right, below) and data acquisition system (right, above).

The station is equipped with a remote data transmission ultrasound stage meter and a stage recorder. In addition, an infrared optic probe (Hach-Lange SOLITAX Hs-line) was selected for the measurement of the suspended sediment concentration. The instrument is housed in a shelter tube through a pulley, a float and a counterweight group. The housing device, anchored to a bridge pier, protects the instrument from the impact of any flowing coarse material and prevents any potential measuring errors caused by incident radiant energy straying into the infrared field. Solar infrared radiation decreases of approximately 63% below 50 mm of clean water, and this information is important particularly in regard to surveys carried out near surface level (Downing, 1991; Lewis & Eads, 2001; Orwin & Smart, 2005). The instrument is controlled through a data acquisition system that was power supplied by a solar panel.

### *Functional characteristics of the optical probe*

The optical instruments are based on the theory that an incident beam in a mixture is subject to absorption, scatter and transmission due to the presence of suspended particles. The light scattered by the particles can be measured by one or more electronic photodetectors positioned at a  $\alpha=90^\circ$  (*side scattering* or *nephelometric scattering*),  $\alpha<90^\circ$  (*forward scattering*) or at  $\alpha>90^\circ$  (*backscattering*) with respect to the direction of the incident beam. The light source can be white, infrared, laser.

The optical technique is susceptible to the granulometric variations which occur with heterogeneous soil and time of erosion, and increased quantities of coarse sediment loads during floods. Variations in turbidity, associated with these phenomena, can lead to non-linear turbidity/SSC relationships (Lewis, 1996; 2003).

Further interferences associated with optical measuring consist of the colour of the particles and the watery

medium which causes the luminous energy to be absorbed in some bands of the visible spectrum, altering the characteristics of the transmitted light. Another interference that affects the spatial distribution of the light scattered by the particles is caused by the ratio between their size and the wavelength of the incident beam: particles of a size comparable to that of the incident beam wavelength scatter light symmetrically, whereas larger particles scatter an irregular light in all directions. The scattered light, the density of the particles and the content of dissolved particles such as pollutants, and organic matter can lead to errors of measurement since they interfere with the diffusion of light between the particles and the photodetector (Gippel, 1989; Foster et al., 1992; Sadar, 1998).

Several measuring techniques have been developed with a view to minimising some of these interferences. Among these the use of an alternate light source (LED) that does not interfere with the absorption spectrum of the sample and a combined system of photometers (*ratio detection system*) capable of compensating for any absorption loss as well as being able to measure elevated turbidity (Sadar, 1999). This technique is adopted by the Hach-Lange SOLITAX probe which is based on the emission of a LED infrared light beam. The probe has a dual function: it measures turbidity, when only the nephelometric photodetector (positioned at 90° respect to the incident beam direction) is active, or suspended sediment when the backscattering photodetector (positioned at 140° respect to the incident beam direction) also works. This method enables a broad range of suspensions (0.001-4000 NTU for turbidity and 0-150 g/l for suspended solids) to be examined and compensates for the effects of light, organic matter and colour. Furthermore, the instrument is fitted with a programmable interval screen wiper.

#### *Laboratory testing*

67 suspensions were constituted using a sample of material taken from the riverbed of the Carapelle stream (fig.3). Before starting the tests, the entire sample was sifted (d=2 mm - UNI, BS Standards) to remove the gravel fraction. No further removal operations were executed on the cementing substances (organic matter, carbonates, ferrous oxide and aluminium) so as not to alter the structural order of the mixture.

After thorough mixing, the sample was split into three batches. The first one (OW—Original Wet) was kept wet and in its original granulometry, the second one (OD—Original Dried) was kept in its original granulometry too but it was oven-dried at 110°C, the third one (SD—Separated Dried) was split into its fine and sand fractions.

#### *Field calibration*

The purposes of the field calibration were: to evaluate the efficacy of the housing system; to identify a calibration curve of the instrument for the specific torrent; to compare the results with those obtained during the laboratory testing.

The instrument was set up in suspended sediment mode (*ratio detection system*) and, during the flood events occurred during the winter-spring season 2006-2007, a programme of physical sampling was carried out. Eight flood events were monitored and 65 physical samples were collected using the “Magistrato” sampler, that belongs to the “thief sampler” category (Holmes et al., 2001). It consists of a horizontal Van Dorn bottle closed by a float mechanism, with a 15 kg ballast and a flip. The samples mainly consisted of fine materials (fig.3).

With regard to the housing system, 17 pairs of samples were taken outside and inside the tube and their solid concentrations were compared in order to find out any alterations in the flow caused by the protective tube.

With regard to the calibration of the instrument, the sediment concentrations of all the collected samples were measured gravimetrically and compared with the data observed by the optical probe.

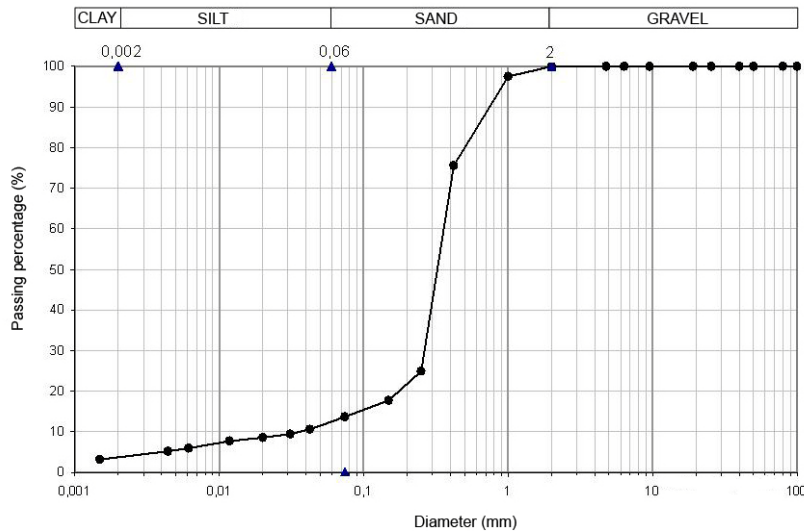


Figure 3. Granulometric curve of the sample material taken from the Carapelle stream.

## Results

### Laboratory testing

The final goal of the first test was to investigate the response of the probe to SSC variations.

The 31 display readings of OD and OW batches were used as input. The analysis of these suspensions show that, plotting the turbidity versus sediment concentrations, the measurement increases up to a top SSC-value ranging between 40-50 g/l (fig. 4).

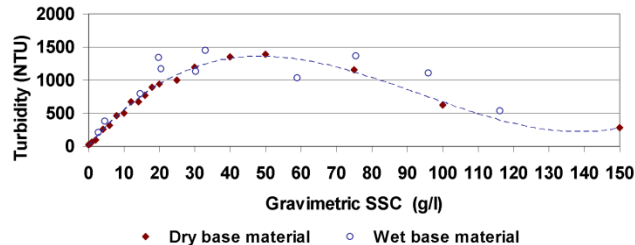


Figure 4. Relationships between the turbidity measured by the instrument and gravimetric SSC (OW and OD batches).

As the concentrations further increase, the measurements decrease. This trend reveals the probe blindness occurring in concentrated suspensions. In suspended sediment mode, on the other hand, blindness does not occur, and the measurement has a linear increment with the sediment concentration (fig.5).

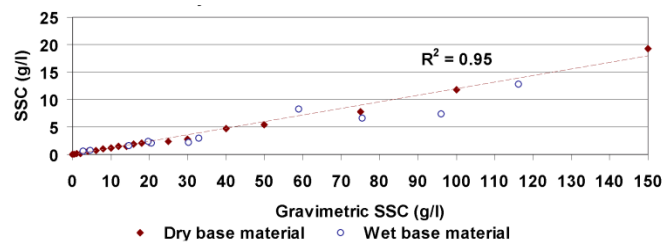


Figure 5. Relationships between the SSC measured by the instrument and gravimetric SSC (OW and OD batches).

The aim of the second laboratory test was to analyze the influence of the grain size composition on the instrument's response. The test was carried out on the 36 SD mixtures, containing the same silt/clay ratio but different percentages of sand. The results show that, for mixtures having the same concentrations, the

instrument's response varies in relation to the percentage of sand.

As expected according to the literature (Foster et al., 1992), the signal was greater in the fine material suspensions (fig.6, fig.7), except for the turbidity mode in the curve limbs affected by probe blindness (fig. 6, falling limbs). In particular, in the turbidity mode, probe blindness occurs even at low concentrations, the phenomenon being more evident at small grain sizes, where it occurs at concentrations as small as 7-8 g/l. This phenomenon decreased considerably in mixtures with larger sand fraction.

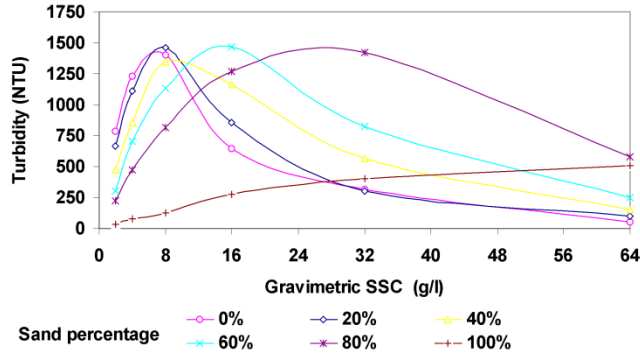


Figure 6. Relationships between turbidity as measured by the instrument and gravimetric SSC.

On the contrary, the suspended sediment optical values always increase with the sediment concentration (fig.7). They have higher values in mixtures with high percentages of fine material than in those that are predominantly sandy. Thus one single conversion factor can be used for mixtures having the same granulometric composition with varying sediment concentration.

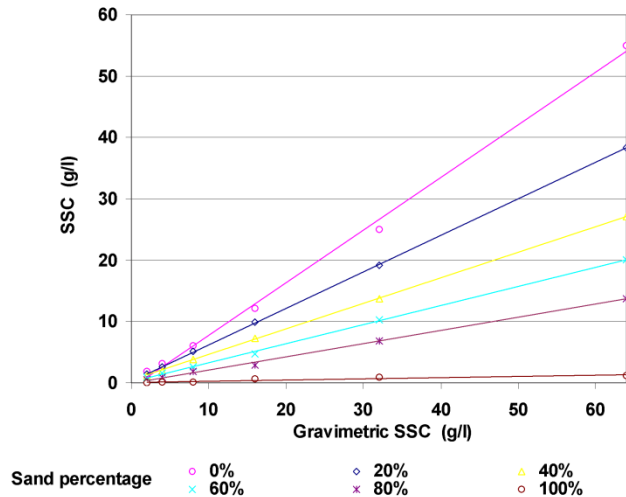


Figure 7. Relationships between SSC as measured by the instrument and gravimetric SSC.

**Field testing**

A comparison of the sediment concentrations inside and outside the protective tube was made, by taking 17 pairs of simultaneous samples. The graph showing the external concentrations as related to the internal ones is well interpolated by a linear function and this confirms that the instrument housing device did not bias the measuring process in any way. This result allows us to consider the samples taken from both positions as part of the series of data used during the calibration stage of the instrument (fig.8).

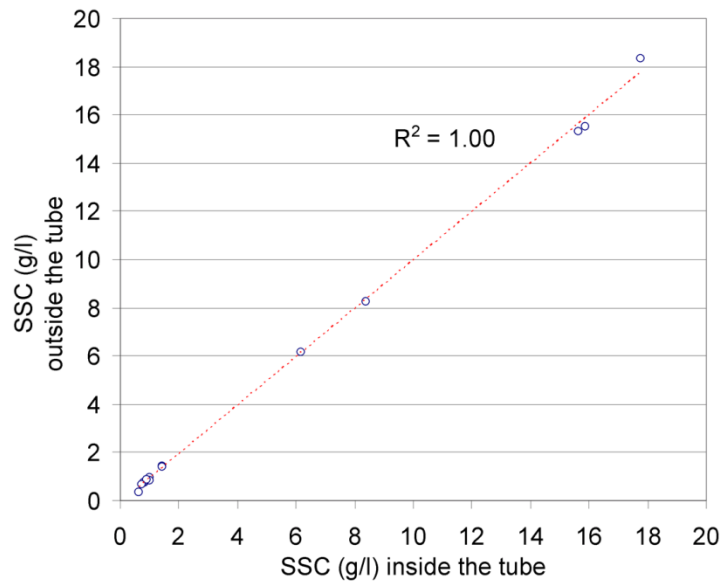


Figure 8. Comparison between the concentrations observed inside and outside the protective tube.

The second analysis carried out during the field stage was the calibration of the instrument. 65 samples, in which the greater part of the sediment consisted of fine material, were taken during 8 flood events. The sediment concentrations of all the samples, measured in laboratory with the gravimetric method, were correlated with the instantaneous data measured by the instrument. Figure 9 shows the graph of the interpolating function ( $R^2 = 0.99$ ). The results confirmed that, in the range of the monitored discharge and for the 2007 sampling campaign, there was a linear relationship between the gravimetric and the optical data. The grain size distribution of the first 28 samples collected during the flood events, and joined together in order to obtain enough material to be able to carry out the analysis, reveals that the material contains a much higher percentage of clay than that taken from the riverbed, as it was to be expected (fig. 3).

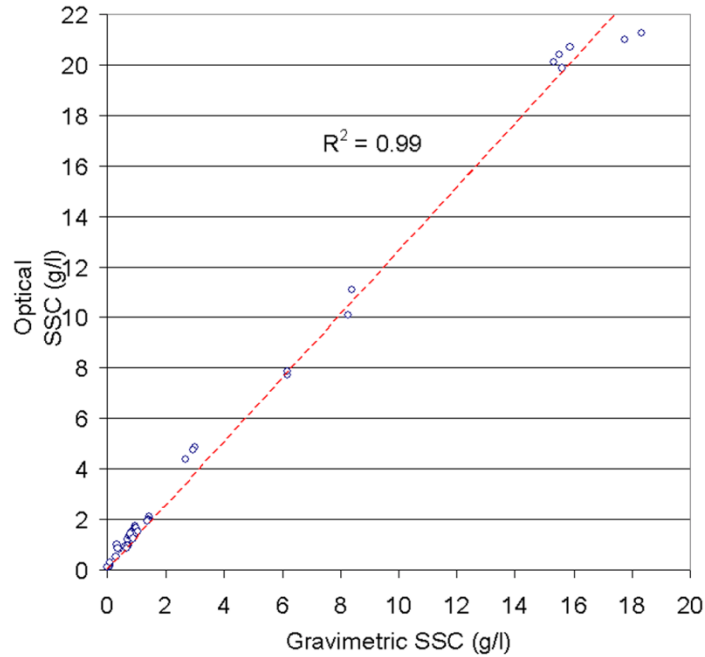


Figure 9. Linear relationship existing between the optical suspended sediment concentration (SSC) measured in field and the gravimetric data.

In order to compare the results of the field tests to those obtained in the laboratory, the relationships between the suspended sediment concentration (SSC) measured by the instrument and that observed by means of the gravimetric method were plotted with reference to the clay content. The graph in figure 10 shows that the field calibration curve, sitting above the other curves, accords perfectly with the laboratory results.

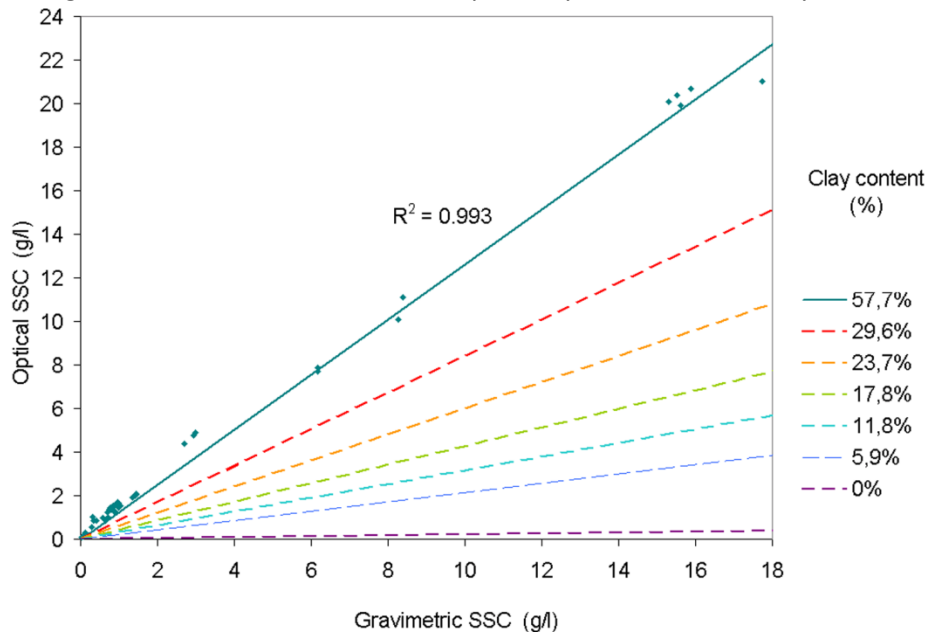


Figure 10. Comparison between the field results and the laboratory analysis.

### **Analysis of flood events**

This section reports a short summary of the analysis of nine flood events occurred in 2007-2008 and having peak discharges between 0.94 and 44.62 m<sup>3</sup>/s. The relationship between sediment concentration and discharge revealed the existence of clockwise, counterclockwise and mixed-shaped hysteretic loops (figs. 11-12-13).

In most cases counterclockwise hysteresis prevails (hydrograph peaks before sedigraph) and this is related to the events of moderate intensity that occur during the entire flood period. During these events (fig. 11) the sediment concentration increases in the falling limb of the hydrographs due to the distance between the sediment sources and the measuring station (Brasington and Richards, 2000).

The most intense events are characterized by a clockwise (fig. 12) or mixed loop (fig. 13). The clockwise loop (sedigraph peaks first) occurs during a simple flood while the mixed loop seems to be typical of graded floods. The advance of the sediment concentration peak can be explained because the sediment availability decreases during the event. If the sediment concentration decreases before the falling limb of the hydrograph, the sediment source areas can be considered limited. This type of loop frequently occurs at the end of the rainy season as they are influenced by the depletion of sediments produced by the previous floods (Campbell, 1985).

### **Conclusions**

This work reports an experimental study about sediment transport monitoring in a river of Northern Puglia (Southern Italy). The measuring instrument was an optical immersion probe which measures the turbidity or the concentration of suspended solids.

The results of the laboratory testing stage show that when optical instruments are used to measure suspended sediments in rivers, a ratio detection system should be preferred, while a single 90° photodetector produces imprecise measurements that are not monotonically dependent on the real value, because of the phenomenon of attenuation of light which occurs with certain concentrations. When the probe was employed in suspended sediment mode a linear relationship between the probe data and the gravimetric ones emerged. Furthermore, with equal levels of concentration, the measurement tended to become greater as the fine fraction content increased.

The field testing stage confirmed the results achieved in the laboratory, evidencing a linear relationship between the optical measurement of suspended sediment and the gravimetric data measured on the turbidity samples. The curve trend agrees with the laboratory observations, since the sample material contained a greater percentage of clay than the material used in the laboratory tests. The instrument housing device did not interfere with the measuring process in any way. The technology adopted made it possible to investigate the relationships between solid and liquid flow during some floods.

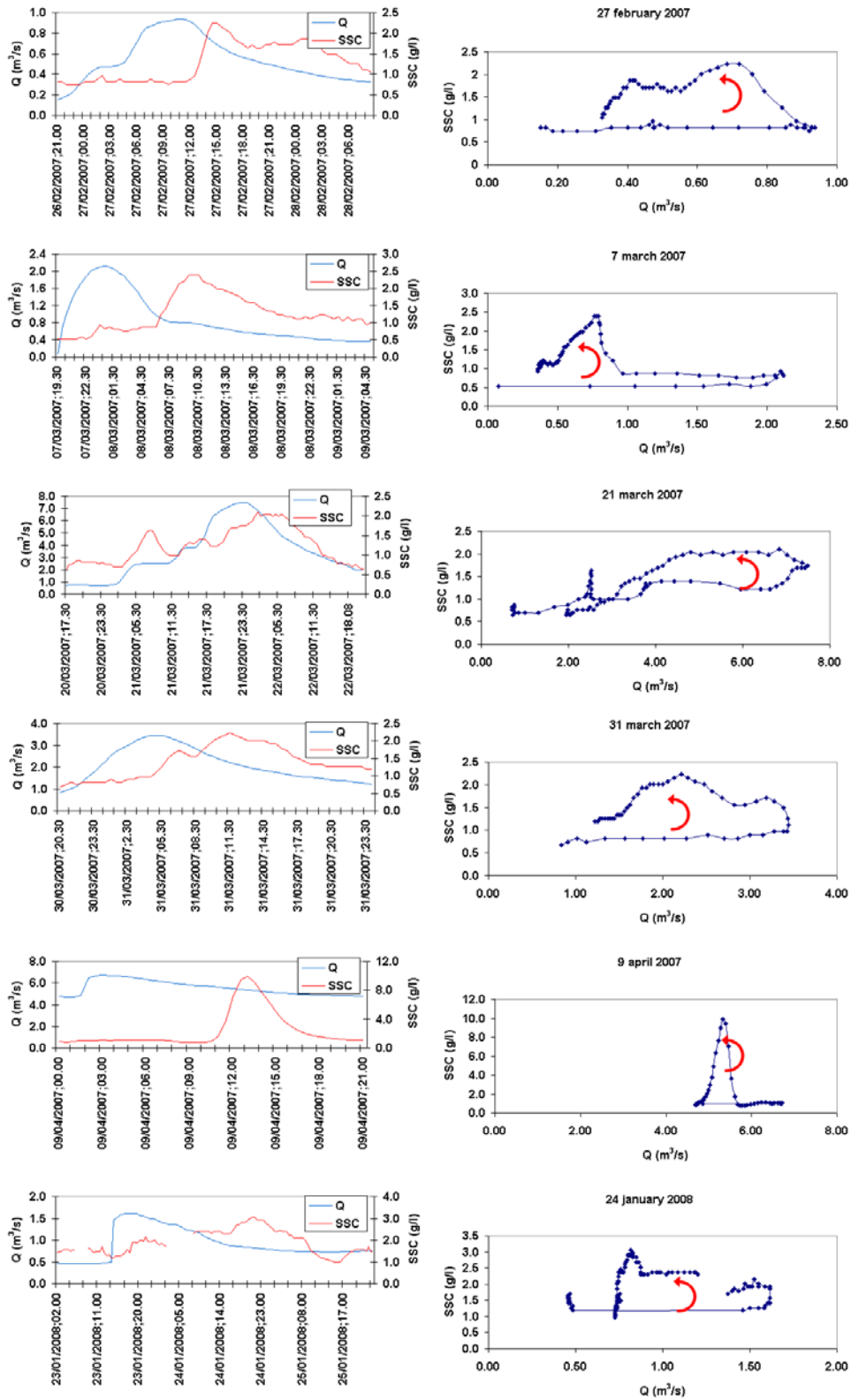


Figure 11. Counterclockwise loops.

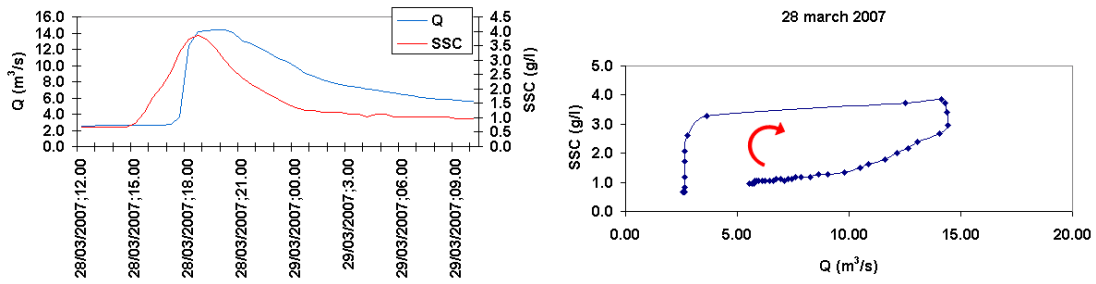


Figure 12. Clockwise loop.

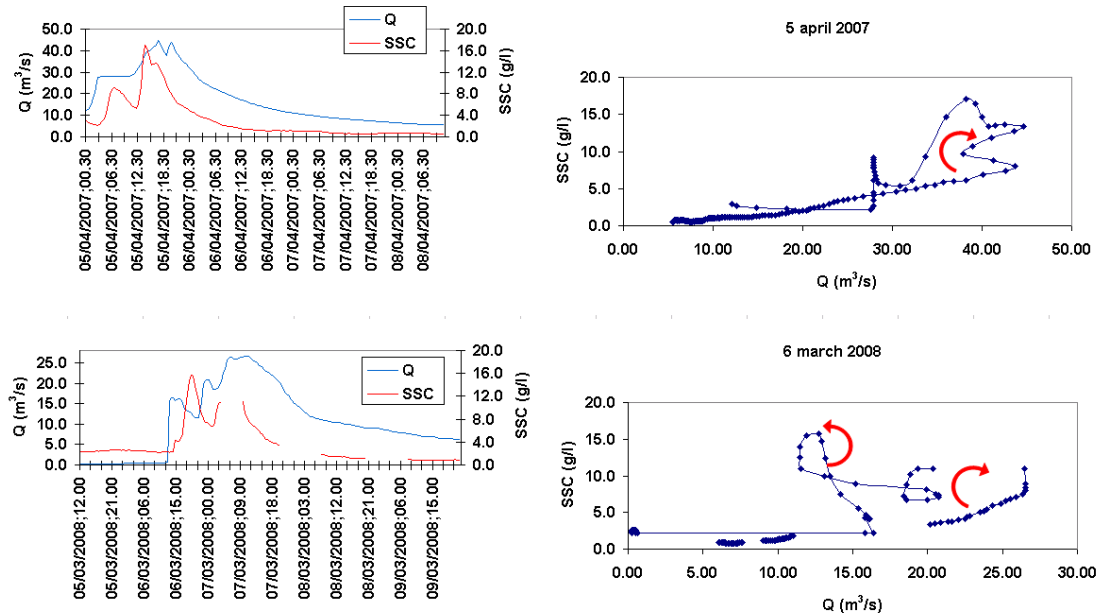


Figure 13. Mixed loops.

## References

Bisantino T; Corbino R; Gentile F; Grittani A; Milillo F; Romano G; Trisorio Liuzzi G; Zanframundo P (2006). Monitoraggio del trasporto solido nei bacini della Puglia settentrionale tra il Candelaro e l’Ofanto. Quaderni di Idronomia Montana 26, 193-204.

Brasington J; Richards K (2000). Turbidity and suspended sediment dynamics in small catchments in the Nepal Middle Hills. *Hydrol. Process.* 14, 2559–2574.

Campbell G S (1985). *Soil Physics with Basic Transport Models for Soil-Plant Systems*. Developments in Soil Science 14, Elsevier New York.

Downing J P (1991). *Instruction Manual: OBS-1 & 3 suspended solids and turbidity monitor*. D&A Instrument. Washington State.

Foster I D L; Millington R; Grew R G (1992): The impact of particle size controls on stream turbidity measurement; some implications for suspended sediment yield estimation, *Erosion and Sediment Transport Monitoring Programmes in River Basins*, 210, 51-62.

Gippel C J (1989). The use of turbidity instruments to measure stream water suspended sediment concentration, Monograph Series No. 4, Dept of Geography and Oceanography, University College, University of New South Wales, Australian Defence Force Academy, Canberra, 204pp.

Holmes R R Jr.; Terrio P J; Harris M A; Mills P C (2001). Introduction to field methods for hydrologic and environmental studies. U.S. Geological Survey, Open-File Report 01-50, Urbana, Illinois, 245 pp. <http://onlinepubs.er.usgs.gov/djvu/>

Lewis J (1996). Turbidity-controlled suspended sediment sampling for runoff-event load estimation. Water Resour. Res. 32(7), 2299-2310.

Lewis J (2003). Turbidity-controlled sampling for suspended sediment load estimation. In: Bogen J Tharan Fergus and Des Walling (eds.), Erosion and Sediment Transport Measurement in Rivers: Technological and Methodological Advances (Proc. Oslo Workshop, 19-20 June 2002). IAHS Publ. 283, 13-20.

Lewis J; Eads R (2001). Turbidity threshold sampling for suspended sediment load estimation. Proceedings of the Seventh Federal Interagency Sedimentation Conference, March 25 to 29, 2001, Reno, Nevada.

Orwin J F; Smart C C (2005). An inexpensive turbidimeter for monitoring suspended sediment. Geomorphology, 68(1-2):3-15.

Sadar M J (1998). Turbidity science. Technical Information Series, Hach Company, 26 pp. <http://www.hach.com/fmmimghach?/CODE:L7061549%7C1>

Sadar M J (1999). Turbidimeter Instrument Comparison: Low-level Sample Measurements. Technical Information Series, Hach Company, 56pp. <http://www.hach.com/fmmimghach?/CODE%3AL7063548%7C1>



## The Application of Holography to the Analysis of Size and Settling Velocity of Suspended Cohesive Sediments.

Graham, G.W.<sup>1\*</sup> and Nimmo Smith, W.A.M.<sup>1</sup>

<sup>1</sup>School of Earth, Ocean and Environmental Sciences, University of Plymouth, UK;  
george.graham@plymouth.ac.uk

Suspended cohesive sediments, typically in flocculated form, are ubiquitous throughout the entire fluvial to marine continuum. Understanding the behaviour of flocculated particles is of fundamental importance in understanding dynamics of cohesive suspensions since the process of flocculation dramatically increases the settling velocity and mass settling flux in comparison to single particle settling. The formation of large porous aggregates from smaller particles complicates the prediction of the behaviour of cohesive suspensions since settling cannot be related simply to particle size. Simultaneous observation of both the size and the still water settling velocity of flocculated particles is crucial if settling fluxes are to be accurately estimated. Knowledge of these parameters allows excess, or effective, densities to be estimated and thus mass fluxes derived for the suspensions. A number of optical – principally video based – methods have been developed for the simultaneous measurement of size and settling velocity of flocculated particles. These include the University of Plymouth's INSSEV (Fennessy et al., 1994; Manning and Dyer, 1999), INSIPID (Benson and French, 2007), DFC (Mikkelsen et al, 2004) and DIPSTIC (Kim and Sanford, 2007) to name but a few. Optical systems are generally limited to a small depth of field since the focal plane of video systems capable of imaging particles on the micron to millimetre scale is narrow. As a consequence the total sampling volumes of such instruments are small and the size of suspended particles outside the focal plane may not be accurately represented during analysis. In addition video based methods have traditionally had long data processing times since particle parameterisations are derived manually. Recently, however, there has been a drive towards semi-automation in certain systems (Fox et al, 2004) with full, real time particle sizing and tracking in others (Kim and Sanford, 2007).

Holography is a promising technique for high resolution imaging of small objects and in-line systems are proven for imaging marine particles in-situ (Malkiel et al, 1999; Owen and Zozulya, 2000; Watson et al, 2001). A novel digital in-line holography system has been developed at the University of Plymouth to obtain synoptic in-situ measurements of suspended particle size, shape and concentration. We present details of an experimental modification to this system which enables the measurement of both size *and* settling velocity of cohesive sediments in a fully automated manner. The optical setup for the in-line holographic system is illustrated in Figure 1A. Diffraction created by particles settling through a collimated laser beam (532nm, 100mW) generates interference fringes (Figure 1B and 2A) which are recorded by CCD with a field of view of 7.4mm by 7.4mm (1002 by 1004 pixels, 7.4 µm per pixel).

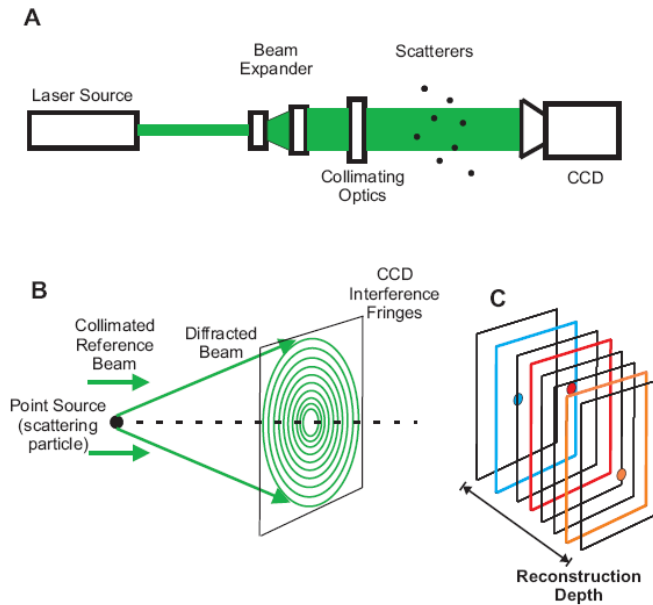


Figure 14 Schematics of simplified optical setup for digital in-line holography (A), diffraction by particle and the creation of interference fringes on the CCD (B) which are numerically reconstructed to produce in-focus images of the scatterers within the sampling volume (C).

Individual frames are numerically reconstructed using a Fresnel transformation in the spectral domain (Milgram and Li, 2002; Sheng, 2006) to produce, from a single 2D image, a stack of plane slices through the sampling volume (Figure 1C). Objects within the sampling volume can be focused individually to produce sharp, in-focus particle images at high resolution (Figure 2B) over a substantial depth of field, resulting in an effective sampling volume of  $7.4\text{cm}^3$ . From these images size and shape metrics can be derived.

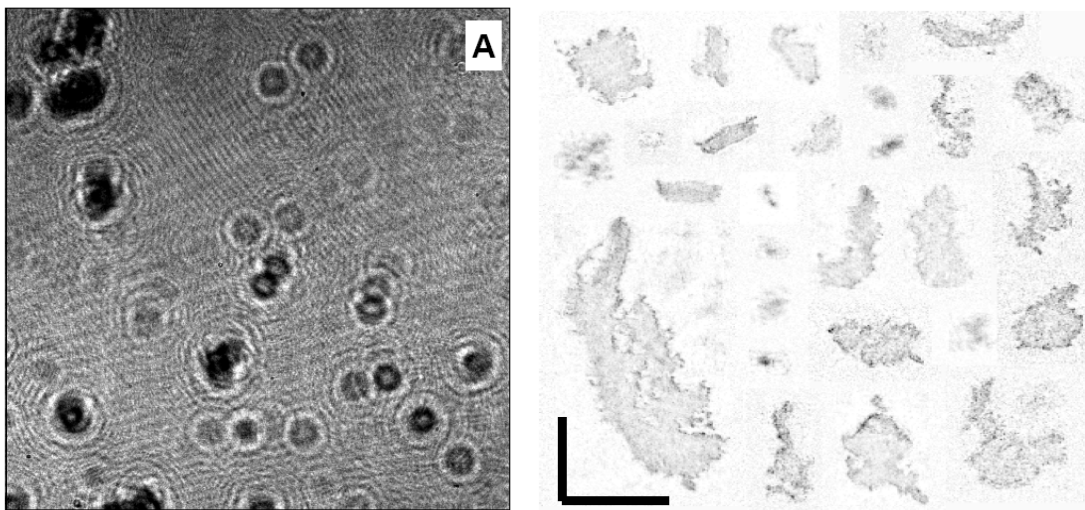


Figure 2 'Raw' hologram demonstrating interference fringes around scatterers in field of view (A) and montage of reconstructed, in-focus, flocculated particles extracted from randomly selected holograms (B). Notice the pronounced non-sphericity and the 'ragged' perimeters characteristic of flocculated particles. Scale bar in (B) is  $500\mu\text{m}$ .

For the purpose of settling velocity estimation, particle settling must be observed in still water so the digital in-line holographic system (which was initially designed for submersible imaging of marine particles) has been equipped with a settling column for ex-situ sampling of suspended sediments (Figure 3 A and B). A small volume of turbid suspension is withdrawn from a source (in this case a large annular flume) using a wide bore

pipette, to minimize disruption to fragile, flocculated aggregates, in a similar manner to the methodology of Manning et al. (2007). The particulates are then allowed to settle through the laser beam which crosses the settling column. Images of settling particles are captured at 10Hz for duration of approximately 150 seconds and are stored for post-processing.

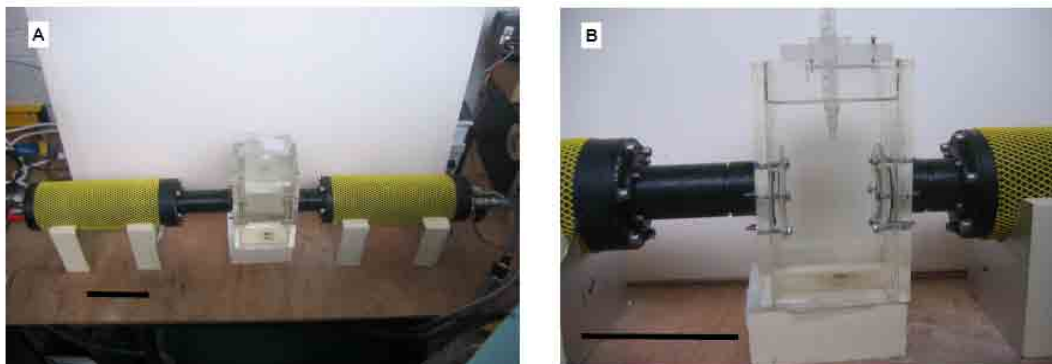


Figure 3 Ex-situ setup of digital in-line holographic system (A) with close up of settling column (B). Perspex column dimensions are  $w=100, d=100, h=1900\text{mm}$ . 45mm diameter sapphire glass ports allow the laser beam entry and exit to the column. Black horizontal bars in both images are approximately 100mm in length.

Image time stacks are processed in a fully automated manner to derive particle size and settling velocity distributions. Image reconstruction is followed by analysis of the spatial variation in the standard deviation of intensity values through the reconstructed image to identify the approximate 2D position of objects within the sampling volume. Global segmentation of the resulting map over the entire field of view, using the method of Lintern and Sills (2006), allows the approximate location and size of objects in the image to be identified. Regions of interest are generated around each identified object in the field of view and in-focus particle images are extracted from variable depths within the reconstructed image. Each of these sub-images of individual particles (Figure 4A) is subjected to a sequence of edge detection (Figure 4B), morphological closure (4C) and convex hull estimation (4D) in order to derive the projected area of the particle (4E).



Figure 4 Processing sequence for projected area estimation (E) from in-focus particle image (A).

Projected area estimates are used to define a spherical equivalent particle size. The spatial co-ordinates of the particles centroid, relative to the field of view, is established and the particle trajectory is then tracked across multiple frames using a combination of logic and 2D gray-scale cross correlation. Cross correlation between successive particle images enables sub-pixel accuracy of particle motion and reduces the likelihood of spurious particle matches between frames. Figure 5A illustrates the trajectory of a single particle moving across the field of view, which has been successfully tracked over 11 consecutive frames. Particle specific statistics (such as the projected area, Figure 5B) are calculated for each of the 11 particle realisation (in-focus images of the particle are illustrated in Figure 5C to confirm that the same particle is tracked over all frames). Some variation in the projected area estimated can be observed over the trajectory. This is associated with particle size and shape

change due to variability in the result of segmentation (Figure 5D).

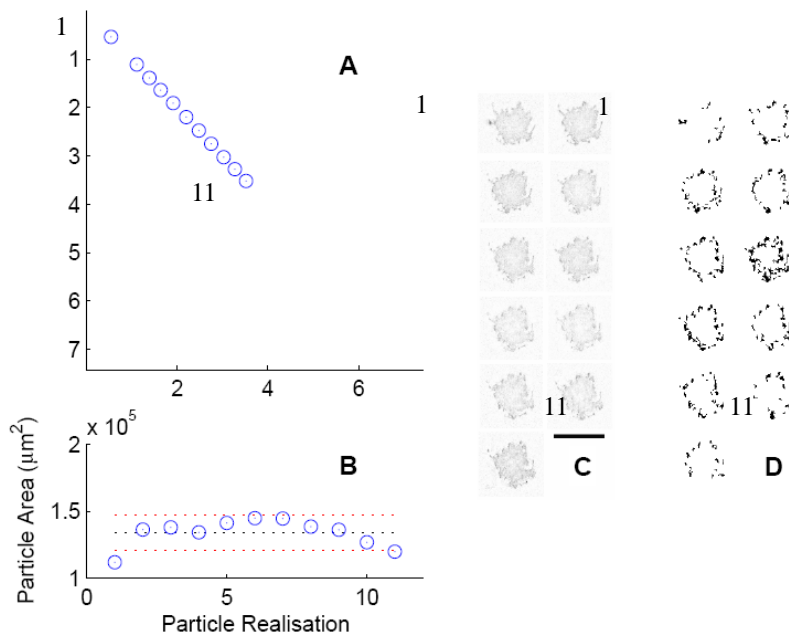


Figure 5 Graphical illustration of particle tracking across field of view (A). Projected area variations over the trajectory are shown in (B). The black dashed line indicated the trajectory averaged projected area (i.e. arithmetic mean of 11 realisations). The red dashed line indicates  $\pm 10\%$  of the trajectory averaged value. Individual, in-focus particle images (C) and their segmented counterparts, prior to convex hull fitting (D) are also shown.

One significant benefit of a tracking method that generates particle statistics over multiple particle realisations is that trajectory averaged particle statistics can be generated with associated error estimates. Particle settling velocity is calculated from the frame-to-frame displacement of a tracked particle and trajectory averaged estimates and confidence intervals similarly generated. The algorithms utilised by Fennessy et al. (1994) and further modified by Manning (2004) are used to calculate values of effective density, dry mass, porosity and mass settling flux for each particle within a sample. These parameters are also trajectory averaged. As an illustration of the power of this technique, results from a single settling experiment are presented in Figure 6. A total of 671 separate particles have been individually tracked and are presented as two distinct size fractions (micro flocs  $< 160 \mu\text{m}$  and macrofloc  $> 160 \mu\text{m}$ ) based on the distinction proposed by Manning (2001). The settling population is heavily dominated by the microfloc fraction ( $> 80\%$  by number).

Trajectory averaged settling velocities of this sample range from  $0.01 - 5.72 \text{ mm s}^{-1}$  and calculated effective densities range from  $11.48 - 1580.71 \text{ kg m}^{-3}$ . The distributions of settling velocity and effective density as functions of particle size ( $30.07 - 443.05 \mu\text{m}$  equivalent spherical diameter) conform to power law relations, typical of flocculated suspensions. Figure 6C clearly shows a polymodal particle size distribution, skewed towards the slow settling microfloc fraction. Sample averaged settling velocities for microflocs are  $0.57 \text{ mm s}^{-1}$  and for macroflocs are  $2.05 \text{ mm s}^{-1}$ . Although the macrofloc fraction comprises only a relatively small number of individual particles, their large size means they are dominant in terms of the mass distribution. Greater settling velocities than the microfloc fraction means macroflocs dominate the mass settling flux (Figure 6E) which is calculated for the sample as the product of size-band-averaged settling velocity and mass concentration estimates.

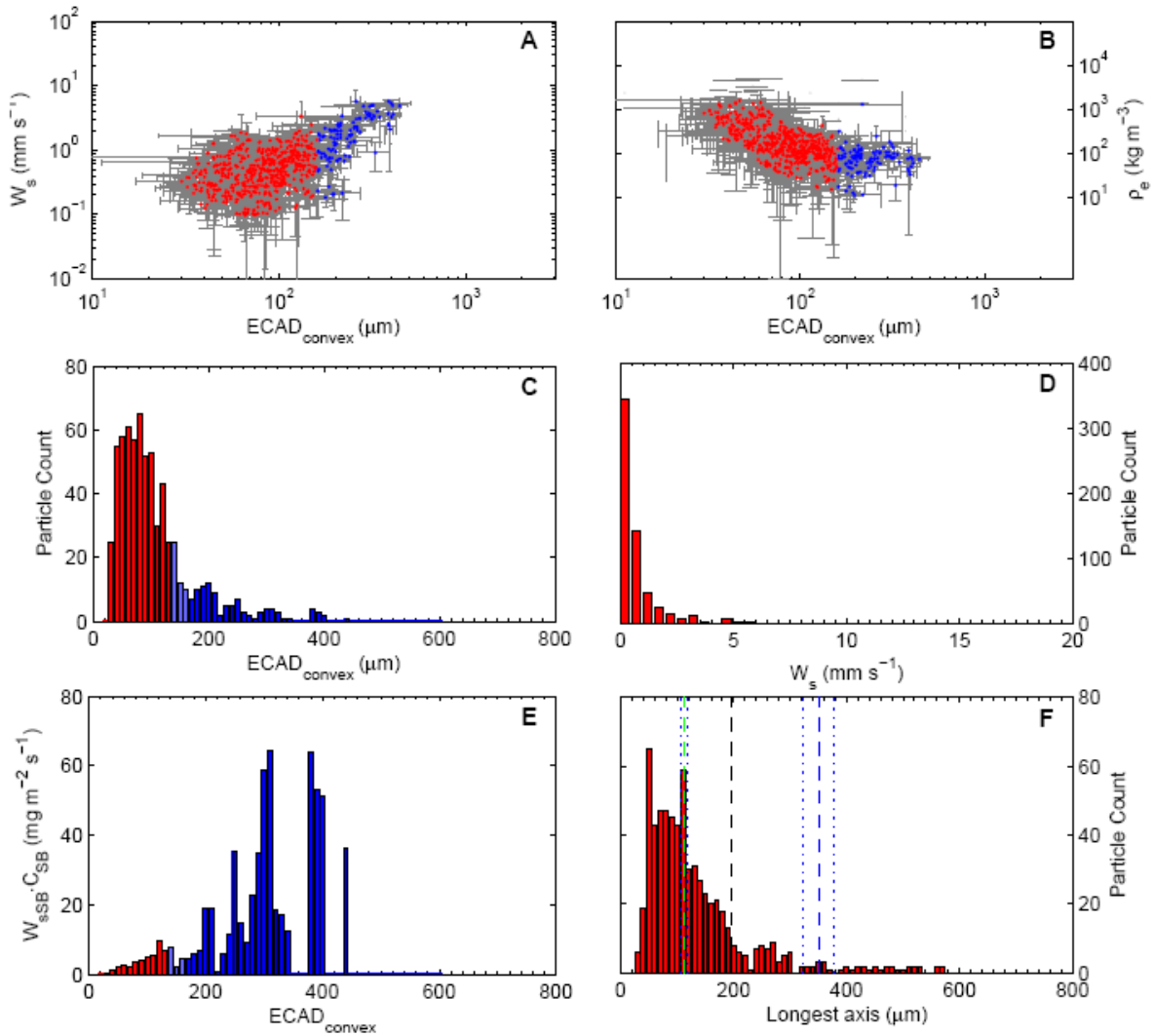


Figure 6 Illustration of particle statistics automatically derived from a single holographic settling experiment. Trajectory averaged particle settling velocity (A) and effective density (B) as functions of spherical equivalent particle diameter (error bars indicate CI of average at  $\alpha = 0.05$ ). Size banded particle size (C), settling velocity (D) and mass settling flux (E) distributions. Red coloration indicates microfloc, and blue the macrofloc fraction.

As an experimental extension of an existing digital in-line holographic particle imaging system, automated settling velocity determination has proven to be extremely effective. This technique allows settling particles (approximately 10 - 7500 $\mu\text{m}$ ) to be tracked at high frequency within a sample volume of 7.4 $\text{cm}^3$ . At present only laboratory settling data are available but the system produces particle sizes, settling velocities and effective densities which are comparable to previously published research. It is conceivable that, with only minor modifications to the existing holographic system, in-situ size and settling velocity information could be obtained and processed in an autonomous fashion. The major, potential, benefits over existing video based systems that measure size and settling velocity are two fold. Firstly, the greatly enlarged sampling volume and the ability to sharply focus particles anywhere within this volume allows accurate representation of particle properties without bias by out-of-focus particles. Secondly, image reconstruction, particle identification, sizing and tracking is fully automated. The automated analysis is carried out on a 1.6GHz T2050 (1Gb RAM) and speed up in 'per sample' analysis time by approximately a factor of 10 over manual particle sizing and tracking is achieved. Further reductions in the time delay between image acquisition and the generation of particle size and settling velocity statistics are envisaged as massive parallelisation of the reconstruction and size/settling velocity extraction algorithms are investigated using a distributed computational grid available at the University

of Plymouth and recent developments in GPU processing.

## References

- Benson, T., and French, J.R. 2007. *Journal of Sea Research*:
- Fennessy, M., Dyer, K.R., and Huntley, D. 1994. *Marine Geology*: **117**, 107-117
- Fox, J., Hill, P., Milligan, T., Ogston, A., and Boldrin, A. 2004. *Continental Shelf Research*: **24**, 1699 – 1715.
- Kim, Y.H., and Sanford, L.P. 2007. *Proceedings of INTERCOH '07*, 113 – 114.
- Lintern, D., and Sills, G. 2006. *Journal of Sedimentary Research*: **76**(10), 1183 – 1195.
- Malkiel, E., Alquaddodmi, O, and Katz, J. 1999. *Measurement Science and Technology*: **10**, 1142 – 1152.
- Mikkelsen, O. A., T. G. Milligan, P. S. Hill, and D. Moffatt. 2004. *Limnology and Oceanography. Methods*: **2**, 226–236.
- Mikkelsen, O.A., Milligan, T.G., Hill, P.S., Chant, R.J., Jago, C.F., Jones, S.E., Krivstov, V. and Mitchelson-Jacob, G. 2008. *Limnology and Oceanography. Methods*: **6**, 133 - 143.
- Milgram, J.H., and Li, W.C. 2002. *Applied Optics*: 41, 835 – 864.
- Manning, A.J., and Dyer, K.R. 1999. *Marine Geology*:**160**, 147 – 170.
- Manning, A.J. 2001. *PhD Thesis*, University of Plymouth.
- Manning, A.J. 2004. *Technical Report TR145*, HR Wallingford, UK.
- Manning, A.J., Friend, P.L., Prowse, N. and Amos, C.L. 2007. *Continental Shelf Research*: **27**(8), 1080-1095.
- Owen, R.B., and Zozulya, A.A. 2000. *Optical Engineering*: **39**(8), 2187 – 2197.
- Sheng, J. 2006. *PhD Thesis*, John Hopkins University.
- Watson, J. et al. 2001. *Measurement Science and Technology*: **12**(8), L9 – L15.

## Field measurements of concentration and mean grain size using 2 ADCP working at different frequencies

M Guerrero, A Lamberti<sup>1</sup>

1. Hydraulic Laboratory- DISTART Department, Bologna University, Bologna, Italy, massimo.guerrero@mail.ing.unibo.it, tel.:+390512093757

### Introduction

Some experiences of suspended sediment investigation with ADCP are already available in the literature, a good example could be found in Hoitink and Hoekstra (2004). These investigation were carried out in marine environment and with the hypothesis of sediment grain size uniformity among the whole field. Relying on that hypothesis only few water-sediment samples are needed in order to calibrate backscattering power.

In many environments characterized by stratification and sediments sorting, grain size uniformity along vertical profiles and furthermore among some kilometers long reach seems hard to believe. The grain size field heterogeneity would force to get many on filed samples in order to assure a reliable calibration among the whole surveyed area, but loosing the ADCP survey advantages: dynamism, velocity, resolution and coverage.

Using many acoustics frequencies gives a different approach to the problem. In fact in that case is possible to solve the sonar equation for both the unknowns: grain size and concentration of scattering particles; Thorne and Hanes (2002). Examples using multi-frequency technique already exist (Traykovski, Wiber and Geyer, 2007), but with dedicated acoustic devices in fixed position and that are not able to simultaneously asses velocity field. Furthermore RDI ADCPs using fore transducer, broadband technology, and characterized by narrow beams and strong acoustic penetration, assure the highest range flexibility and accuracy for echoes and time lag data (RD Instruments 1996).

The carried out surveys on Po river and Tirreno sea using two Teledyne RDI ADCPs working at different frequencies on the same water column is an application of the multi-frequency method. A moving vessel, ADCPs equipped, surveyed the whole velocity and sediment fields in short time.



*Figure 1. Two ADCP at different frequencies installation and in action.*

Figure 1 shows the ADCPs installation and a phase of the carried out dynamic measurements.

The two following chapters will describe the acoustic method used for concentration and grain size profile assessments (chapter 2) and the resulting evidences on velocity and concentration field and on processes taking place during fluvial and sea surveys (chapter 3).

## Acoustic Method

Backscattering power of an acoustic beam propagating in water depends also on numerosness and scattering size of suspended particles inside the sound covered water volume; Thorne and Hanes (2002). Knowing that some equations can be developed relating received echo features to suspended sediment mass, scattering particle dimension and quantity.

Any acoustic backscattering method for concentration assessment is founded on the sonar equation, Medwin and Clay (1998). The simplified form of the sonar equation follows, Deines (1999), with backscattering power  $S_v$  expressed by the main environment and electrical acoustic ADCP features, RD Instruments (1996):

$$S_v = C + 10 \cdot \log_{10}(T + 273.16) \cdot R^2 - L - P + 2\alpha R + K_c \cdot (E - E_r) \quad (1)$$

In equation (1)  $S_v$  is the backscattering power in dB,  $C$  is the instrumental coefficient that holds the in factory ADCP features [dB],  $T$  is the transducer temperature in [C°],  $R$  is the distance along the beam [m],  $L$  is  $10 \cdot \log_{10}$  of transmitted wave length in meters,  $P$  is  $10 \cdot \log_{10}$  of transmitted power in watts,  $\alpha$  is the sound absorption coefficient [dB/m],  $K_c$  is the conversion factor between instrumental counts and dB,  $E$  is the ADCP measured echo intensity [counts],  $E_r$  is the measurable by ADCP minimal echo [counts].

The electrical acoustic instrumental features:  $C$ ,  $L$ ,  $P$ ,  $K_c$  and  $E_r$  must be know, some approximate value can be found in literature, Deines (1999), and they can be measured in laboratory with some specific acoustic devices, Deines (1999).

The backscattering power can be evaluated knowing the surveyed with ADCP data:  $T$ ,  $R$  and  $E$ , and the sound attenuation coefficient  $\alpha$ .

Unfortunately backscattering power and sound absorption are both dependent on scattering size and particle concentration. Therefore having two unknowns, the method needs at least two equations to be written, corresponding to backscattering power at two different frequencies.

The one frequency method asses concentration using the sonar equation (1) and fixing in advance a uniform scattering size. In fact calling  $s$  the backscattering power, not more in dB, the following expression, Thorne and Hanes (2002), can be written for the suspended mass  $M$ :

$$M = \frac{s}{\sigma} \cdot \rho_s \cdot \frac{4}{3} \pi \cdot a^3 \quad (2)$$

where the scattering particle numerosness for unit volume is written as the ratio between backscattering power and the mean scattering size  $\sigma$ .

Working with two frequencies on the same water column, equations (2) and (1) can be written two times obtaining the needed relations. In particular the second one gives the solving equation:

$$\frac{s_1}{s_2} = \frac{\sigma_1}{\sigma_2} \quad (3)$$

where the mean grain size is the only unknown.

Functions relating acoustic parameters  $\sigma$  and  $\alpha$  to suspended mixture features and carrying frequency have been studied since many years, Thorne and Hanes (2002).

In order to have an univocal solution for equation (3), both frequencies must be sensitive to suspended particles. In fact form and attenuation factors have a low threshold for acoustic sensibility to suspended particles, and on the other side high threshold for  $x$  dependence, being  $x$  the product between acoustic wave number and particle grain size.

Instrumental frequencies choice became important not only for the maximal expected depth range, but also for the ability to investigate different grain sizes. In practice the multi-frequencies method using commercial ADCP frequencies is able to investigate concentration and grain size field inside the silt-sand range, with typical acoustic shadow zones for finer and/or too far fraction and for coarser and/or too near sand.

### Survey Results

The surveyed Po branch is  $8 \times 10^3$  m long and 270 m wide, two hundreds kilometers from the mouth, in the Boretto zone where the catchments basin is 55 thousands of square kilometers, the 75% of the whole. The mean flow is south-east oriented. The experimental survey stage condition was a low stage ( $1000 \text{ m}^3/\text{s}$ ), with a frequency of about three months in the period 1944-1989 and of only 1.5 month in 2007.

The ADCPs and DGPS equipped vessel followed longitudinal and transversal tracks (figure 2) in order to map the whole concentration field.

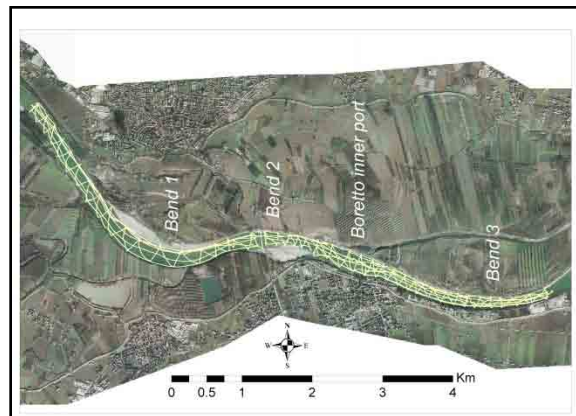


Figure 2. Acoustic survey tracks carried out on Po river at Boretto.

The vertical averaged values are meaningful in order to characterize the suspended sediment transport field, see maps in figure 3 and 4.

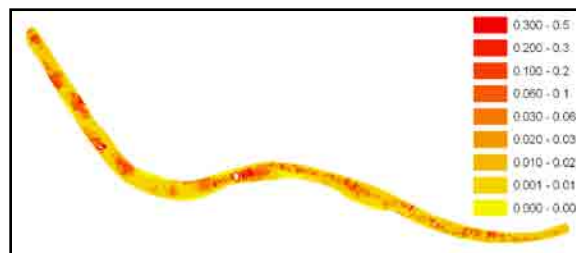


Figure 3. Concentration [kg/m<sup>3</sup>] map from acoustic multi frequencies survey.

The upstream branch up to the first bend is strongly characterized by the alternative bars morphology that can be seen also looking at bathymetry simultaneously surveyed with Multibeam, figure 5. Bar morphology drives high concentration,  $0.2 \text{ kg/m}^3$ , of finer material,  $2 \times 10^{-4} \text{ m}$ , on low depth area corresponding to bar toss face.

The strong current taking place in the first bend seems to erase alternative bars concentration field, instead it gives rise to high concentration in the following inflection point after the current impact on the outer side of

the first bend. Then current and suspended sediment transport remain strong up to the following wide and low depth area.

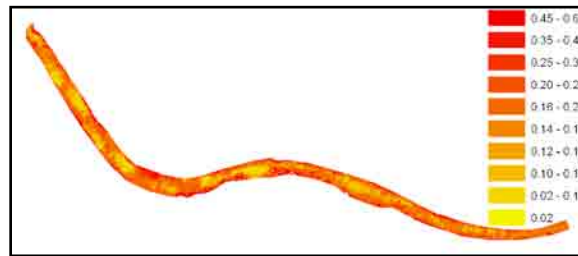


Figure 4. Mean grain size [ $10^{-3}$  m] map from acoustic multi frequencies survey.

The downstream bend shows some concentration of coarse grain in its upstream side at the wide area junction. In that area the convex angle at right side gives rise to a strong current from right to left, which is able to suspend bed sediments. Then the alternative bar behavior, with high concentration related to low depth, arises one more time but in a less enhanced way despite the upstream branch.

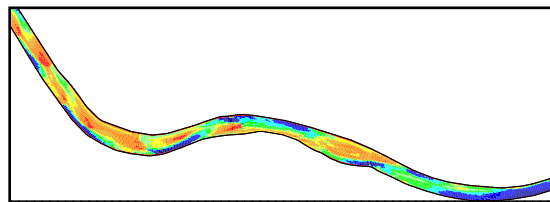


Figure 5. Multibeam bathymetry.

ADCP suspended sediment transport and velocity surveys are useful also for concentration and velocity field analysis along vertical sections. As example is described a longitudinal transect of the upstream branch up to the flex between the two consecutive central bends. As already underlined enhanced alternative bars characterize the upstream straight reach. The maximal concentrations take place at top and ridge top bars where velocity increase is cause of finer material suspension, figure 6. High depth and low velocity and concentration follow. In practice a typical riffle and pool morphology at low stage, Richards (1982), takes place, which drives high velocity, roughness and concentration at riffle location; that location probably changes at high stage condition.

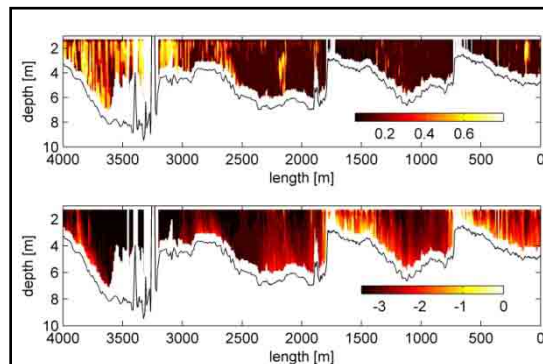


Figure 6. Mean grain size [ $10^{-3}$  m] and concentration  $\log_{10}[\text{kg}/\text{m}^3]$  for the longitudinal transect.

Two well defined exceptions take place at 2100 and 4000 longitudinal coordinates, which show high concentration of coarser grain size at high depths, in fact these are two velocity field singularities. The first exception is related to a strong vertical up velocity (fig.7-below). The downstream velocity singularity is the

maximal magnitude velocity located at the outer side of the bend (fig.7-above). The velocity field singularities produce coarser grain suspension.

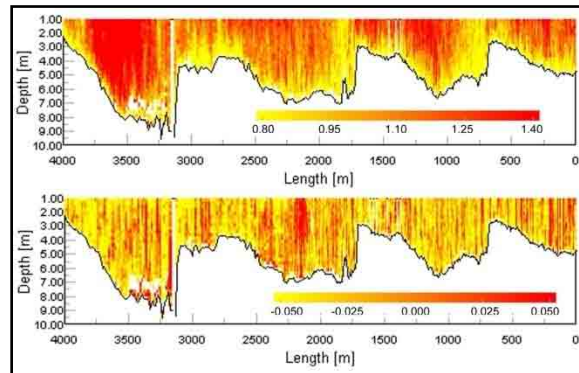


Figure 7. Magnitude velocity and vertical up velocity [m/s] for the longitudinal transect.

Aim of the Mediterraneo sea survey was to investigate the turbidity diffused by dredging works. In order to test the multi frequencies method, a calibrated Multi Parametric Probe (MPP) was employed, almost simultaneously and on the same water column sound irradiated by ADCPs.

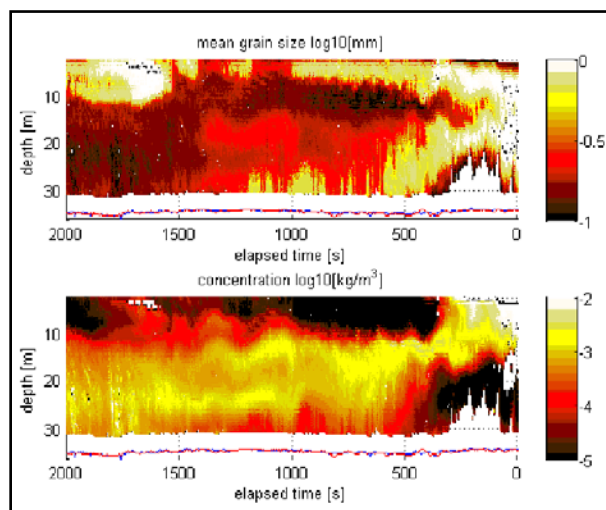


Figure 8. Mean grain size  $\log_{10}[10^{-3}m]$  and concentration  $\log_{10}[kg/m^3]$  for sea survey.

One example of the outcomes of the analysis is given in figure 8. Time increases toward left. The diffusion of sediments through the water column is visible from the surface on the right, where the dredging boat dumped some material. Higher concentrations of 100 mg/l near surface, also visible on field as very turbid water, are fast spread towards deeper layers by the mean principal current depth of 15-20 m. A bifurcation is evident in concentration and diameter patterns, showing finer material less than 0.2 mm being suspended by the current and coarser material sinking down. Some resuspension phenomena is also visible above -10 m. These could be related to dredging boat and monitoring vessel wakes. Indeed figure 9, presenting the ADCP velocity transects, shows some wakes at the same time and positions.

The simultaneously acquired MPP profile shows a peak concentration of 2.5 mg/l between -10 and -15 m depth. Figure 10 shows a good agreement between calibrated MPP concentration profile and the ADCPs concentration profile, averaged in time during MPP acquisition. Looking at mean diameter ADCP profile, it is evident that dredging activities give rise to fine sand turbidity clouds (0.65-0.20 mm), where the coarser scattering particles are related to natural organic material (in low concentrations).

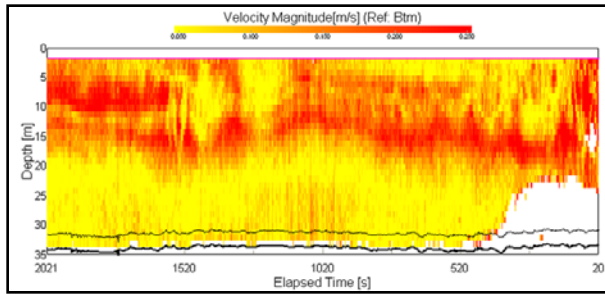


Figure 9. Magnitude velocity [m/s] for sea survey.

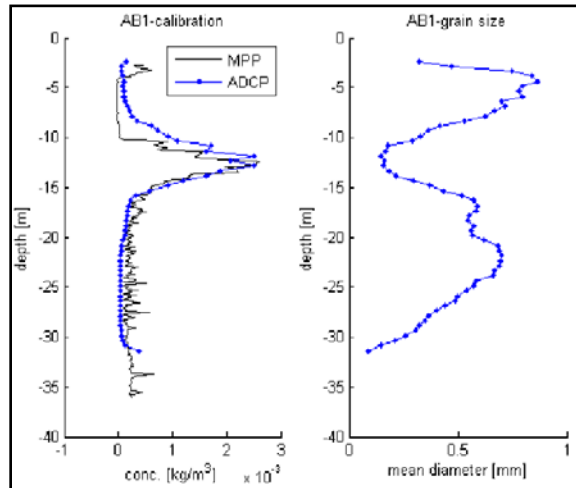


Figure 10. ADCPs and MPP profile

## Conclusion

Concentration and mean grain size fields can be surveyed simultaneously using at least two ADCPs working at different frequencies.

The main advantage of the method is the ability to investigate suspended mixture features also in strong sorted environments, without making any hypothesis regarding grain size field uniformity as single frequency method does.

The available commercial ADCPs drive frequencies choice only on few values spaced of 500-600 kHz, and designed for different maximal depths. In the view of sediment investigation frequency choice-availability became important also in order to univocally estimate mean grain size. In fact backscattering power coming from coarser mean grain size are not more dependent on high frequencies, and on the other hand to low frequencies are not sensitive to finer material. Concluding can be said that the double frequencies advantage could be lost outside silt-sand range, depending also on in situ concentration. In those cases the single frequency method is still useful to estimate concentration by introducing some hypothesis regarding unknown mean grain size.

## References

Deines K.L., 1999. Backscattering Estimation Using Broadband Acoustic Doppler Current Profilers. IEEE conference, San Diego.

Hoitink A.J.F., Hoekstra P., 2004. Observation of suspended sediment from ADCP and OBS measurements in a mud-dominated environment. Coastal Engineering 52 (2005) 103-118. Elsevier B.V.

- Medwin H., Clay C.S., 1998. Fundamentals of Acoustical Oceanography. Academic Press. London.
- RD Instruments. 1996. Acoustic Doppler Current Profiler, Principles of Operation A Practical Primer. San Diego.
- Richards K.,1982. Rivers form and process in alluvial channels. Methuen & Co. Ltd. New York
- Thorne P.D., Hanes D.M., 2002. A review of acoustic measurement of small-scale sediment processes. Continental Shelf Research 22(2002) 603-632. Elsevier Science Ltd. Pergamon.
- Traykovski P., Wiber P.L., Geyer W.R., 2007. Observation and modelling of wave-supported sediment gravity flows on the Po prodelta and comparison to prior observation from the Eel shelf. Continental Shelf Research 27(2007), 375-399. Elsevier Science Ltd. Pergamon.



## Particles size characteristics of the Rhone river and Plume suspended matter

Stéphanie Jacquet<sup>1</sup>, Olivier Radakovitch<sup>1</sup>

1. CEREGE, UMR 6635, Eurôpe de l'Arbois, BP80, 13545 Aix en Provence, France

### Why are we interested in measuring *in situ* particles size?

#### 1. CHACCRA project-Objectives

The coastal zone is a vulnerable area which undergoes increasing anthropogenic pressures due to the population growth. The impact of agriculture in upstream regions associated with fertilizer use or deforestation along with the development of hydro-electric power stations have brought important changes in the quantity and quality of dissolved and particulate matter carried by rivers to the sea. The coastal zone is also a rich and diversified oceanic region where highly productive ecosystems are maintained by continental inputs: dissolved nutrients allow phytoplankton production while particulate carbon directly feeds the sediment fauna. These inputs also determine the role of the coastal region in the global carbon (C) cycle. In the coastal C budget, while continental shelves are considered to date as sink areas for CO<sub>2</sub>, uncertainties concerning near shore regions and especially estuaries and river-connected coastal areas are large. This is partly due to the complexity of processes and the temporal and spatial variations of particulate and dissolved materials supplied by rivers. Indeed, river floods may carry from 50 to 70% of annual particulate inputs. A first attempt to integrate near shore region in coastal zone C budget indicates that it could be a source of CO<sub>2</sub> of similar magnitude as the continental shelf sink. Therefore quantifying near shore C fluxes is crucial to determine the importance of coastal zones at a global scale. Furthermore, climate change will alter coastal ocean C budgets: water warming and stratification could stimulate production and mineralization whereas an increase in frequency and intensity of extreme events (storms and floods) could strengthen the particulate transport. This in turn will modify C fluxes and ecosystems functioning.

The present work is part of an integrated study CHACCRA (**C**limate and **H**uman-induced **A**lterations in **C**arbon **C**ycling at the **R**iver-se**A** connection) which aims to determine the impact of these anthropogenic and climate alterations on the carbon mass balance and ecosystem functioning at the river-sea interface. CHACCRA intends to study C fluxes and simulate their modification at the Rhone river outlet, the major river in the western Mediterranean Sea, and in the Gulf of Lion, its adjacent shelf. The specific goal of CHACCRA is to provide the first detailed modelling scenarios of C cycle alterations by integrating to a coupled physico-chemical model three different components of the Rhone-Mediterranean interaction: the river inputs, the plume processes and the benthic recycling. In particular, our objectives are to characterize the Rhone river particles and their behavior and variability on the adjacent shelf. By applying a multi-tool approach, we confront particles size distributions and concentrations to determine the fate of fine grain-sized fluvial particles transferred seaward at short time-scales. Particular focus is made on floods and extreme events periods.

#### 2. The Rhone river

The Rhone river (France) represents the major fresh water input and SPM transfer to the Gulf of Lions, with a mean solid discharge around  $7.4 \cdot 10^6$  T/y and an interannual variability ranging from  $1.2$  to  $19.7 \cdot 10^6$  T/y. It is usually assumed that the Rhone fluvial particulate matter rapidly accumulates in the prodelta (where recent accumulation rates range from 30 to 50 cm/y at the river mouth) and that particulate transfer on the shelf mainly occurs via nepheloid layers. However, little is still known on the fate of fine grain-sized fluvial particles transferred seaward and on their behaviour at short time-scales during more important river discharge. It is also particularly less known in the area of transition between low-salinity and marine waters (i.e. along the saltwedge) which is the site of important processes which significantly change the nature and fate of materials entering the coastal zone. The salt induced flocculation process is often referred to explain bottom nepheloid

layer near the Rhône river mouth, even it has not been clearly demonstrated yet. During low to medium water discharge periods, the salt intrusion can extend up to 20 km inland, while during medium and high water discharge periods the location of the salt wedge is pushed seaward to the river mouth and over sea, forming a plume flowing over salt water, as recently observed last May 2008 (Figure 1).



Figure 1: Transition between Rhône plume waters and seawater in the Gulf of Lions.

### 3. Our sampling strategy

Subsurface water sampling for suspended matter are conducted in the Rhône river at the gauging Arles station (Kilometric Point Pk 285; 47.5 km upstream from the river mouth; Figure 2) and at different Pks between Arles and the river mouth. The Arles station is located in the “Grand Rhône” which accounts for 90% of the Rhône water discharge. Different hydrodynamic flow regimes are studied: low water discharge periods ( $<1000 \text{ m}^3/\text{s}$ ; samples monthly recorded), medium water discharge periods (from 1000 to  $3000 \text{ m}^3/\text{s}$ ; samples monthly recorded) and high water discharge periods ( $>3000 \text{ m}^3/\text{s}$ ; samples daily recorded). Water samples are collected at Arles using an autonomous pumping system and at the different Pks using a bucket.

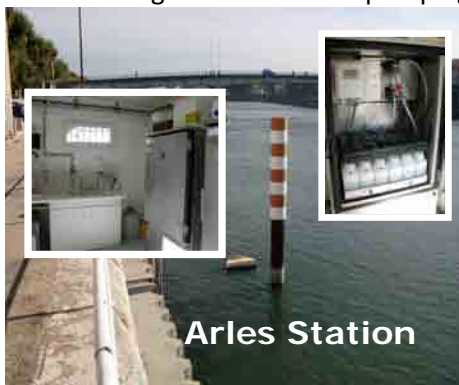


Figure 2: The gauging Arles station

Water column sampling for suspended matter are also conducted in the Rhône river plume on the continental shelf in the Gulf of Lions. A first survey, RHOFIBENT, was carried out in fall 2007 (1-13/11/07; R/V Europe) and a second, PLUME, in spring 2008 (15-19/05/08; R/V Tethys II). RHOFIBENT occurred during a very low discharge period ( $500 \text{ m}^3/\text{s}$ ) and PLUME during a medium period ( $1300 \text{ m}^3/\text{s}$ ). The sampling strategy during the RHOFIBENT and PLUME cruises was to first cover a grid of stations in the region of the fresh water influence (transects crossing the plume seaward from the river mouth). The second step was to follow the low-salinity water plume dilution seaward using buoyant sediment traps. Water samples were collected at 4 to 8 depths using a CTD rosette equipped with Niskin bottles.

### 4. Our multi-tool approach- Expectations

The Rhône river inputs and plume processes are investigated using a multi-tool approach including a particles

counter (Met-one; Hach), a laser size analyser (Malvern mastersizer S) and an in situ laser diffraction particle sizer (LISST-100 type B). During the PLUME cruise (May 2008), an intercalibration was moreover performed with IFREMER (P. Bassoullet and coll.) by deploying next to our LISST a second LISST instrument (type C) and a video profiler. Our aim is to confront the particles size distributions and concentrations obtained from these different instruments:

(1) The particles counter Met-one gives the concentration of particles for 5 size classes ranging from 2 to 200  $\mu\text{m}$ . This instrument is adapted to low discharge periods. To be correctly analysed samples concentration should not exceed 15000 particles/mL. Dilution is rapidly required for river water samples during flood events (where values can reach up to  $5 \times 10^6$  particles/mL), as well as for nepheloid or highly productive seawater samples. Two applications of the Met-one are shown in Figures 3 and 4. Figure 3 shows total particles concentration for stations sampled along the river plume at sea during RHOFIBENT. Particles mainly ranged from 2 to 10  $\mu\text{m}$  in diameter.

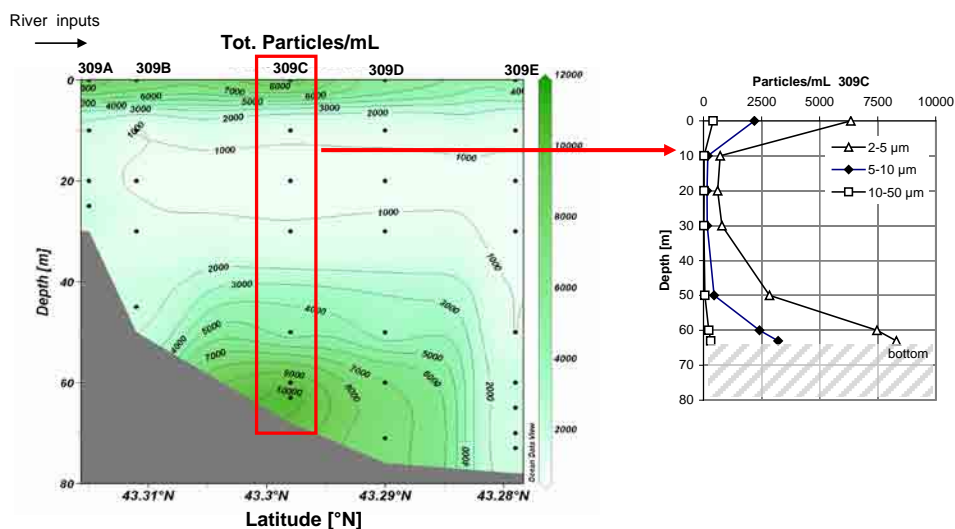


Figure 3

Figure 4 presents total particles concentration at Arles station versus Rhone water discharge from October 2007 to March 2008. Focus is made on two situations presenting a net evolution of the 10-50  $\mu\text{m}$  size class.

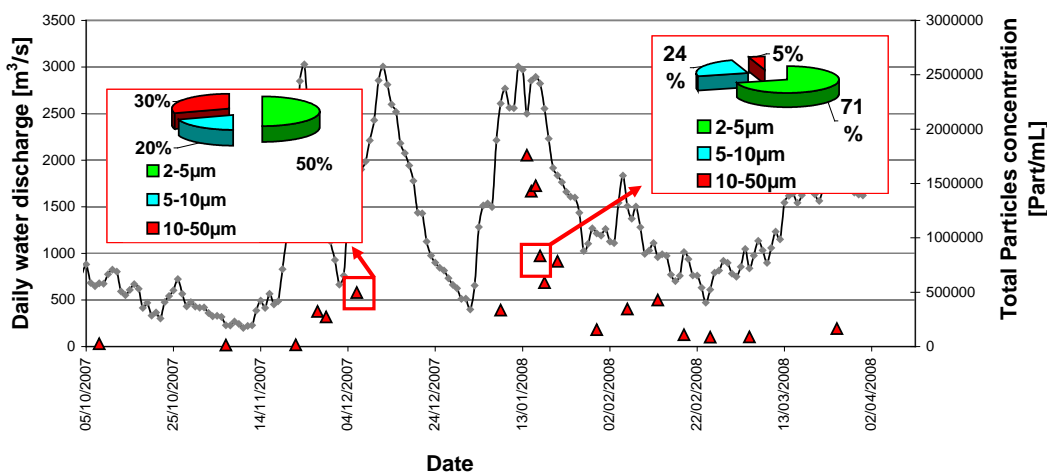


Figure 4

(2) The Malvern mastersizer gives the particles size distribution for particles ranging from 0.05 to 900  $\mu\text{m}$ . In contrast to the Met-one, the Malvern requires sufficiently charged water. Both Met-one and Malvern

measurements are done on punctual samples. The difficulty consists in obtaining sufficient resolution on profiles and time series. Using the Malvern instrument next to the particles counter allows to get complementary information on the variability and processes affecting particles. An application of Malvern is shown in Figure 5. This figure shows the evolution of the particles size distribution at Arles station during a flood event (22-24 April 2008).

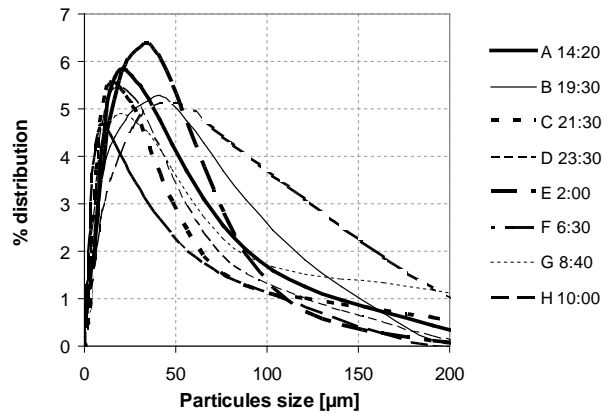


Figure 5

(3) The LISST-B instrument allows to obtain both in situ and highly resolved profiles for particles ranging from 1.2 to 250 µm. Size distributions at certain depths could be compared to those obtained via Niskin bottles and Malvern measurements. The problem we encountered during our cruises consisted in differences in depth and temperature scale between LISST and CTD data. Moreover, it's new expertise for our team. Expertises of colleague are warmly requested especially in deciphering and valuing LISST data files (what is the "best" way to confront in situ and continuous, i.e. depth profiles, size distributions: mean, median, kurtosis, skewness, etc...).

## Determination of the Particle Size Distribution Using Satellite Ocean Color Imagery: Applications and Assessment of Uncertainty

TS Kostadinov<sup>1</sup>, DA Siegel<sup>1</sup>, S Maritorea<sup>1</sup>

1. University of California Santa Barbara; ICES, Ellison Hall 6832, UC Santa Barbara, Santa Barbara, CA 93106-3060, USA; tiho@icess.ucsb.edu

The World Oceans' biota plays an important part in planetary carbon cycling. Oceanic ecosystem structure and function have been linked to the size distribution of the populations of phytoplankton (Chisholm, 1992). For example, particle export rates, which are linked to organic carbon storage, are strongly dependent on particle sizes (Eppley and Peterson, 1979; Azam, 1998; Falkowski et al., 1998). Oceanic particle size distributions (PSD's) most often follow the Junge-type (Junge, 1963) hyperbolic size distribution (e. g. Sheldon et al., 1972; Gin et al., 1999; Boss et al., 2001), which has been implicated to have ecological significance (Platt and Denman, 1977; Cavender-Bares et al, 2001; Chisholm, 1992; Rinaldo et al., 2002). The differential number concentration as a function of particle diameter of such a PSD spectrum has the form

$$N(D) = N_o \left( \frac{D}{D_o} \right)^{-\xi}$$

where  $N(D)$  is the number of particles per volume of seawater normalized by the size bin width [ $m^{-4}$ ],  $D$  is the particle diameter [ $m$ ],  $D_o$  is a reference diameter ( $2 \mu m$ ),  $N_o=N(D_o)$ , and  $\xi$  is the hyperbolic slope of the PSD. The slope  $\xi$  and  $N_o$  are the two parameters of this Junge-type size distribution.

In-situ measurements of oceanic PSD's are rare, especially in the open ocean. Satellite sensors are necessary in order to provide global synoptic coverage that would allow for PSD measurements to be used in global ecosystem and biogeochemical models. Bio-optics provides the link between PSD's and space-borne measurements. Optical properties of particle assemblages, including the particle backscattering coefficient, depend on the particle composition as well the PSD, and can be predicted using Mie theory (Mie, 1908). On the other hand, the backscattering coefficient analytically related to the spectrum of satellite-observed normalized water-leaving radiance,  $LwN(\lambda)$ , (Gordon et al., 1988; Reynolds et al., 2001). The Loisel et al. (2000) algorithm can retrieve the total backscattering coefficient spectrum,  $b_{bp}(\lambda)$ , from satellite derived  $LwN$ 's. Therefore,  $b_{bp}(\lambda)$  can be theoretically linked to the PSD parameters and is also retrievable from space.

The particulate backscattering spectrum is often modeled as a hyperbolic function as follows

$$b_{bp}(\lambda) = b_{bp}(\lambda_o) \left( \frac{\lambda}{\lambda_o} \right)^{-\eta}$$

(e.g. Morel, 1973; Garver and Siegel 1997). Loisel et al. (2006) used SeaWiFS observations to calculate  $\eta$  from ocean color data using the spectrally retrieved  $b_{bp}(\lambda)$  at 490, 510 and 550 nm. Figure 1 illustrates their retrieval for August of 2007. Loisel et al. (2006) demonstrated that 1)  $\eta$  can be retrieved reliably from space, and 2) there exist global spatial and temporal patterns of  $\eta$  that correlate to chlorophyll- $a$  (Chl) distribution in the different ecological zones of the World Ocean. Fig. 1 reveals that high  $\eta$  values are found in the oligotrophic subtropical gyres, where Chl is low, whereas low  $\eta$  values are found in coastal, Equatorial and high latitude waters, where Chl is higher due to enhanced productivity.

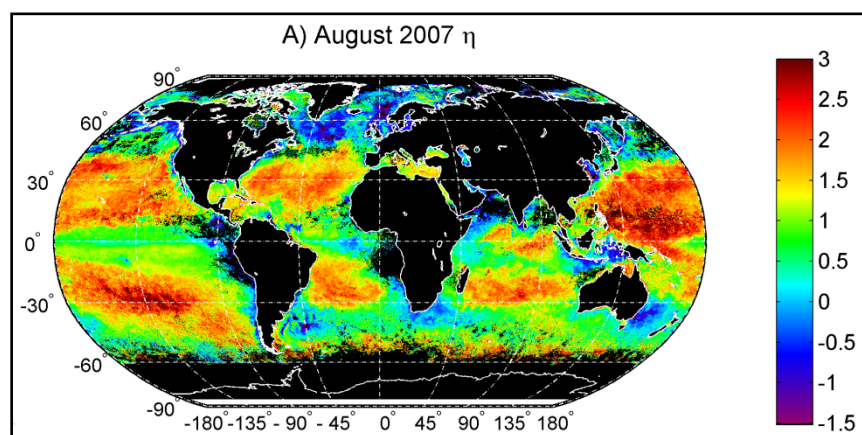


Figure 1. Map of the global distribution of the spectral slope of  $b_{bp}(\lambda)$ ,  $\eta$  for August of 2007. After Loisel et al., 2006.

Here, a novel bio-optical model is presented that is capable of retrieving the parameters ( $\xi$  and  $N_o$ ) of a Junge-type PSD using parameterizations based on Mie theory (Mie, 1908). The algorithm builds on the results of Loisel et al. (2006) by using their global retrievals of the  $b_{bp}(\lambda)$  spectral slope  $\eta$  in order to parameterize the slope of the Junge-type PSD. Further,  $\eta$  and the value of  $b_{bp}(440)$  are used to retrieve the differential number concentration of backscattering particles at a reference diameter of 2  $\mu\text{m}$ . In summary, a Junge-type PSD was assumed and a Mie model was run while varying the input hyperbolic PSD slope from 2.5 to 6 and picking the rest of the Mie parameters (bulk complex index of refraction, maximum and minimum diameter of integration) from realistic distributions in a Monte Carlo exercise aimed at assessing model uncertainties due to their variability, termed here endogenous uncertainties. The spectral slope of the resulting modeled  $b_{bp}(\lambda)$  was calculated for each Monte Carlo run and used to construct single run LUT's  $\eta = f(\xi)$  and  $\eta = g(\log_{10}(b_{bp}(440)/N_o))$ . All the Monte Carlo  $f$  and  $g$  tabular functions were used in the inverse mode to arrive at the operational mean inverse LUT's  $f^{-1}$  and  $g^{-1}$ , with the associated uncertainties.

The algorithm was then applied to August 2007 monthly global mapped SeaWiFS data that has been resampled at a resolution of 27 km/pixel. Fig. 2A is a map of the retrieved Junge PSD slope  $\xi$  for August of 2007. 78.4% of the pixels have values between 3.5 and 5, the mean is 4.22, and the median - 4.15. Fig. 2B is a map of the corresponding  $N_o$  parameter in log<sub>10</sub>-space. The mean is 15.58, the median - 15.71, and the standard deviation - 0.75. Obvious global spatial patterns in the Junge-type PSD parameters emerge in Fig. 2. Notably, the oligotrophic subtropical gyres are characterized by relatively high PSD slopes and low particle differential number concentrations at 2  $\mu\text{m}$ , as compared to the coastal, upwelling and high latitude regions, which tend to have lower PSD slopes and higher particle concentrations. This general pattern is consistent with the idea that low productivity, low Chl areas are characterized by predominantly smaller particles, whereas relative contribution of large particles increases in high Chl, high productivity areas (Chisholm, 1992; Falkowski et al., 1998; Reynolds et al., 2001; Loisel et al, 2006). There is strong negative correlation between  $\xi$  and  $\log_{10}(N_o)$ ,  $r = -0.96$ . Thus, areas of high particle concentrations are also characterized by relatively higher dominance of bigger particles and vice-versa.

Validation of the products of the PSD algorithm using a compilation of global Coulter counter in-situ data is satisfactory on large temporal and spatial scales, whereas individual point comparisons leave room for improvement. Comparisons with BATS bacterial counts are satisfactory. There are multiple reasons why the in-situ validation data is expected to differ from the satellite retrievals. First, the in-situ Coulter counter data sets have a narrower diameter range (2-20  $\mu\text{m}$ ) than the diameter range mostly contributing to backscattering (Stramski et al., 2004). Importantly, the satellite data is averaged over very large temporal (one month) and spatial (27 km pixels) scales as compared to the scales of in-situ data collection (meters, minutes). Finally, the Coulter counter is sensitive to particle volume, whereas Mie theory and measured backscattering are sensitive

to particle effective cross-sectional area. Deviations from sphericity will cause these two types of measurements to differ (Lee-Karp Boss et al., 2007).

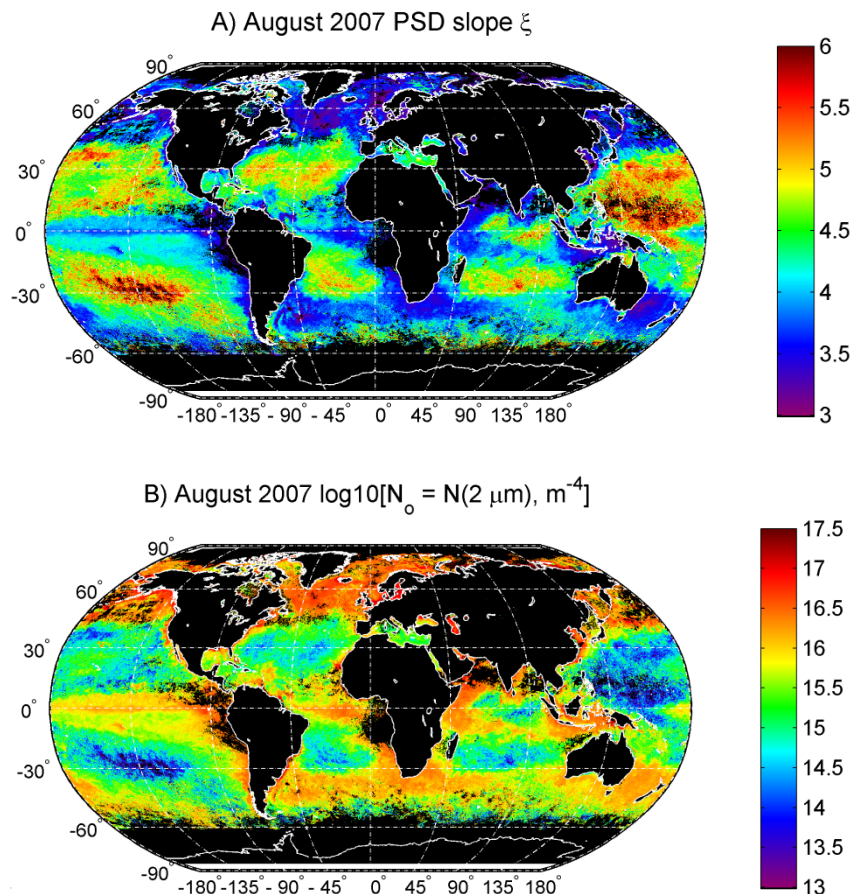


Figure 2. Base products of the PSD algorithm for August of 2007. A) Map of the retrieved PSD Junge slope,  $\xi$ ; B) map of the retrieved value of  $N_0$  in  $\log_{10}$  space. The hyperbolic slope  $\xi$  and  $N_0$  are strongly anti-correlated ( $r = -0.96$ ).

Various important biogeochemical and ecological parameters can be derived once the PSD slope  $\xi$  and  $N_0$  are known. Here, particle number concentration and percent volume contribution in the ecologically significant size ranges corresponding to picoplankton ( $< 2 \mu\text{m}$ ), nanoplankton ( $2- 20 \mu\text{m}$ ), and microplankton ( $20$  to  $50 \mu\text{m}$ ) (Sieburth et al, 1978; Vidussi et al., 2001) are calculated by integrating the retrieved Junge-type PSD in the respective size-ranges. Fig. 3A is a map of the number concentration of phytoplankton-sized particles for August 2007 in the  $0.5 \mu\text{m}$  to  $50 \mu\text{m}$  diameter range. The overall range of number concentrations barely spans three orders of magnitude. Figs. 3B-D show the partitioned number concentration among pico-, nano-, and microphytoplankton-sized particles. The maps exhibit a couple of important characteristics: 1) for all three size classes particle number concentration is higher in the productive regions (at least by a couple of orders of magnitude) than it is in the oligotrophic subtropical gyres, and 2) the spatial variability of pico-sized particle number concentration is about 2 orders of magnitude, nano-sized particles vary about 4 orders of magnitude, whereas micro-sized particles vary up to 9-10 orders of magnitude. Picoplankton-sized particles (which can be associated with the microbial loop and regenerative production, e.g. Azam, 1998) are numerically dominant everywhere in the ocean.

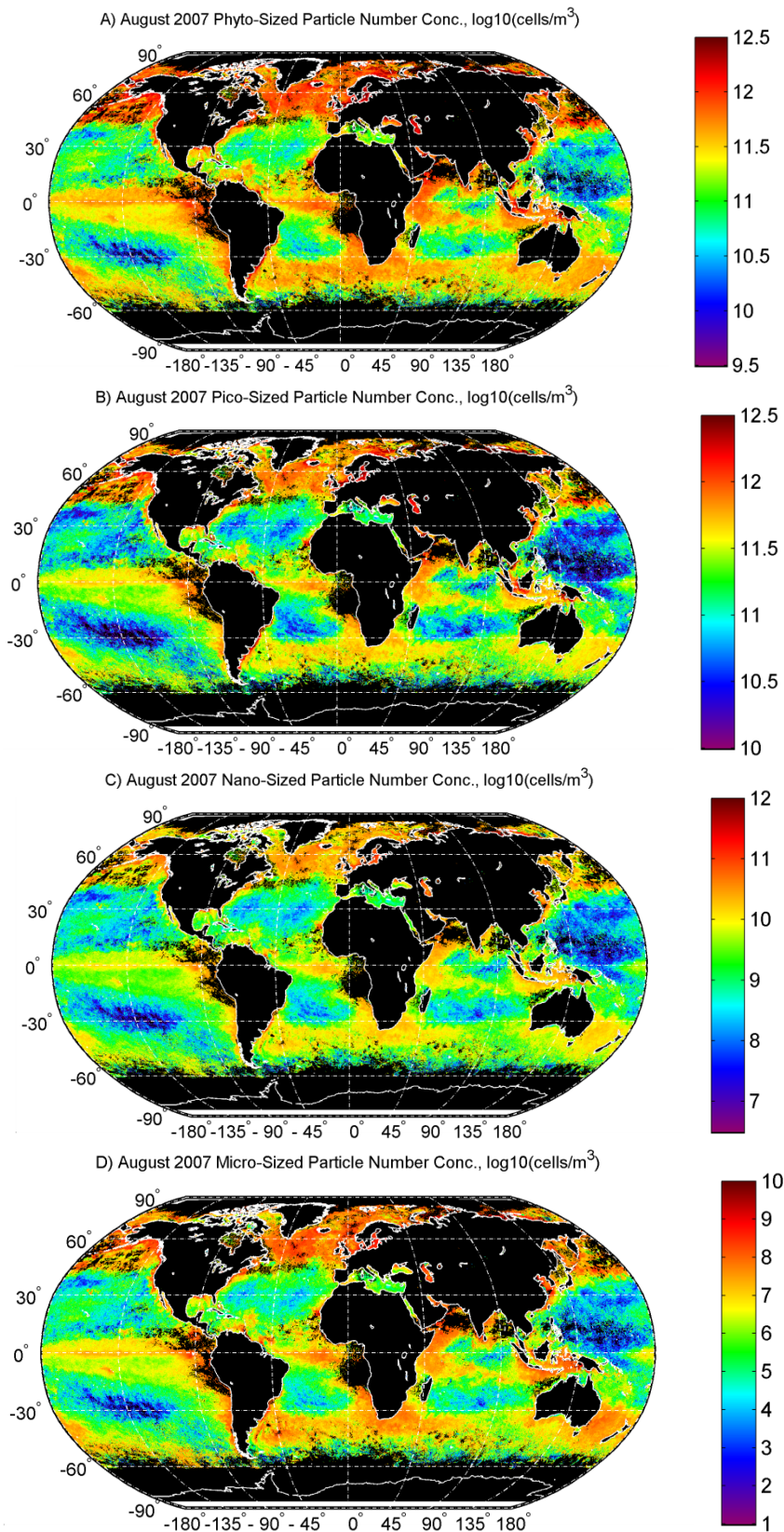


Figure 3. Global maps of A) Total number concentration of phytoplankton-sized particles, from  $0.5 \mu\text{m}$  to  $50 \mu\text{m}$ ; B) Number concentration of picoplankton-sized particles; C) Number concentration of nanoplankton-sized particles; D) Number concentration of microplankton-sized particles. Units are particles/ $\text{m}^3$  of seawater; maps are plotted on a  $\log_{10}$ -space.

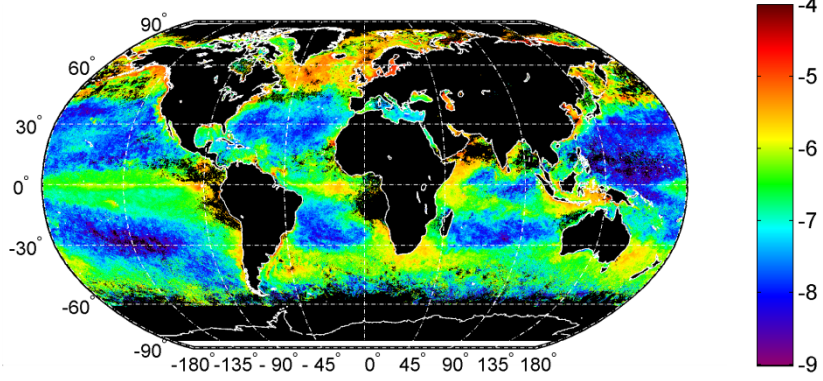
Fig. 4A is a map of the volume concentration of phytoplankton-sized particles for August of 2007. These estimates are useful because volume, rather than number concentrations are related to biomass and carbon content (e.g. Gin et al., 1999 and refs. therein). As expected, productive areas of the ocean exhibit relatively high particle volume, whereas the subtropical gyres exhibit the lowest particle volume concentrations. Figs. 4B-D are maps of the volume concentration contribution of the three phytoplankton size classes to total volume in the entire size range. The maps exhibit the following global characteristics: 1) Picoplankton-sized particles dominate the volume concentration in all five subtropical gyres of the World Ocean (60-100%); 2) Nano-sized particles are prevalent in transitional, upwelling, coastal and higher latitude regions, but their contribution rarely exceeds 50%. The areas where their contribution is about 50% covers a significant fraction of the oceans (Fig. 4C); 3) Micro-sized particles contribute up to 50-60% of the volume concentration only in select regions known for their high productivity, such as coastal areas, the North Atlantic bloom area, the Equatorial and Eastern Boundary Current Upwelling zones, and higher latitudes. They are virtually absent in the subtropical gyres and much of their transition zones. These observations support the idea that picoplankton are ubiquitous and constantly in the background, whereas episodic blooms and increases in Chl are caused by large, microplankton cells, and these events can be associated with sinking/export (Falkowski et al, 1998; Uitz et al., 2006).

The maps of Figs. 3 and 4 pertain to the entire particle load that has contributed to backscattering in the respective size classes, not just living or organic matter. In order for the maps to have a valid ecosystem and biogeochemical interpretation, it is assumed that living particles and their covariates are the first order driver of the backscattering particle assemblage and its variability on global and monthly and longer scales. The high correlation of Chl retrievals with the volume concentration values of Fig. 4 ( $r = 0.82$ ) suggests that the primary driver of the particle load variability is indeed biological activity and its established global scale patterns (e.g Falkowski et al., 1998).

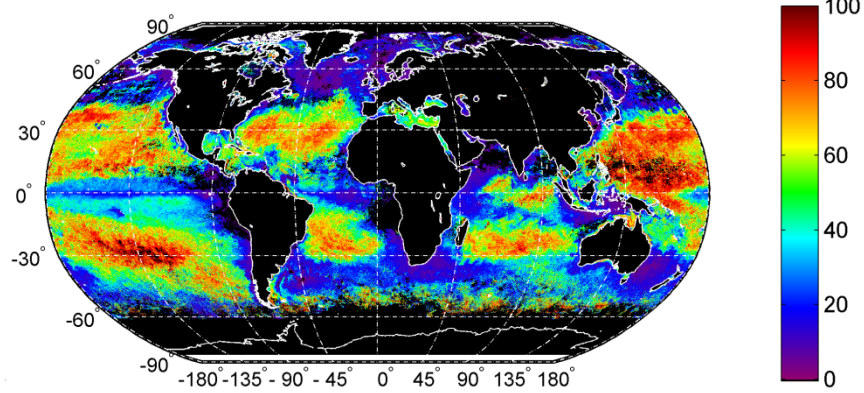
The Monte Carlo simulation used in the development of the mean operational LUT's allows for the estimation of the model endogenous uncertainties. The highest uncertainties in the Junge slope retrieval occur at the lowest (negative)  $\eta$  values, whereas lowest uncertainties are associated with higher  $\eta$  values. These uncertainties are driven primarily by a combination of the imaginary index of refraction and the maximum diameter of integration. The spatial distribution of  $\eta$  (Fig. 1) suggests that for most of the ocean area (the subtropical oligotrophic gyres and their transition zones) the endogenous uncertainty in the Junge slope retrieval is minimal. Higher uncertainty tends to occur in higher productivity areas (Fig. 5A). In contrast to the Junge slope uncertainty pattern, the uncertainty in  $N_o$  retrieval (in log-10 space) is more uniform across all values of the  $b_{bp}(\lambda)$  slope (Fig. 1), which results in a more uniform spatial pattern of  $N_o$  uncertainty (Fig. 5B). The  $N_o$  uncertainty is driven primarily by the variability in the real index of refraction.

The endogenous uncertainties of the base products (Fig. 5A and 5B) were propagated to the derived products. Fig. 5C maps the propagated uncertainty of the number concentration of microplankton-sized particles. It is obviously driven in large part by the  $N_o$  uncertainty, as it has a similar magnitude and spatial distribution. Fig. 5D is a map of the endogenous uncertainty in the percent particle volume due to microplankton-sized particles. The oligotrophic gyres and their transition zones exhibit virtually zero uncertainty, whereas the high productivity and coastal and high latitude areas are subject to only up to 6% uncertainty. This is very encouraging and is a reflection of the fact that the calculation of this parameter does not require knowledge of  $N_o$ ; thus the percent volume contribution derived products are very reliable as compared to products that are absolute numbers.

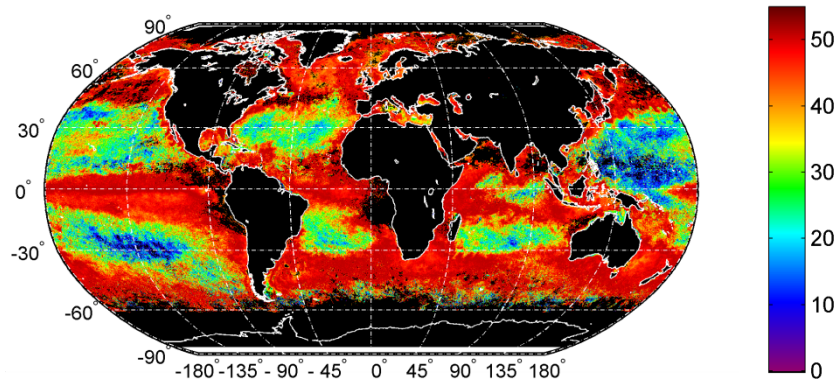
A) August 2007 Phyto-Sized Particle Volume Conc.,  $\log_{10}(\text{volume of cells}/\text{volume of seawater})$



B) August 2007 Pico-Sized Percent Volume



C) August 2007 Nano-Sized Percent Volume



D) August 2007 Micro-Sized Percent Volume

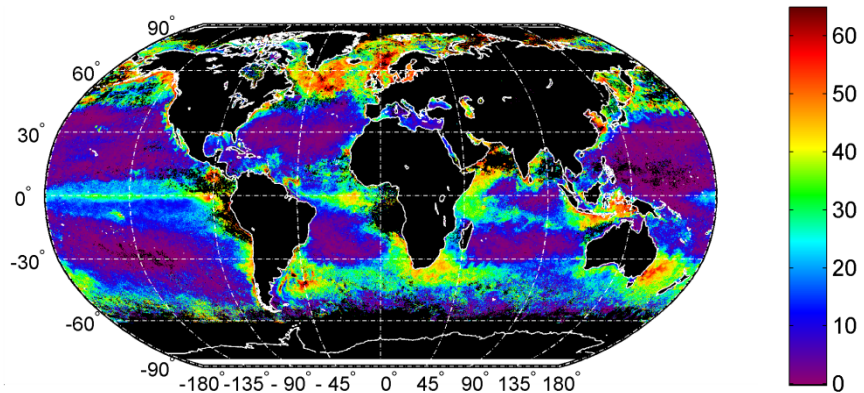


Figure 4. Global maps of A) Total Biovolume,  $\log_{10}(\text{total particle volume}/\text{volume of seawater})$  – sizes between  $0.5 \mu\text{m}$  and  $50 \mu\text{m}$  were considered; B) Percent biovolume due to picoplankton-sized particles; C) Percent biovolume due to nanoplankton-sized particles; D) Percent biovolume due to microplankton-sized particles.

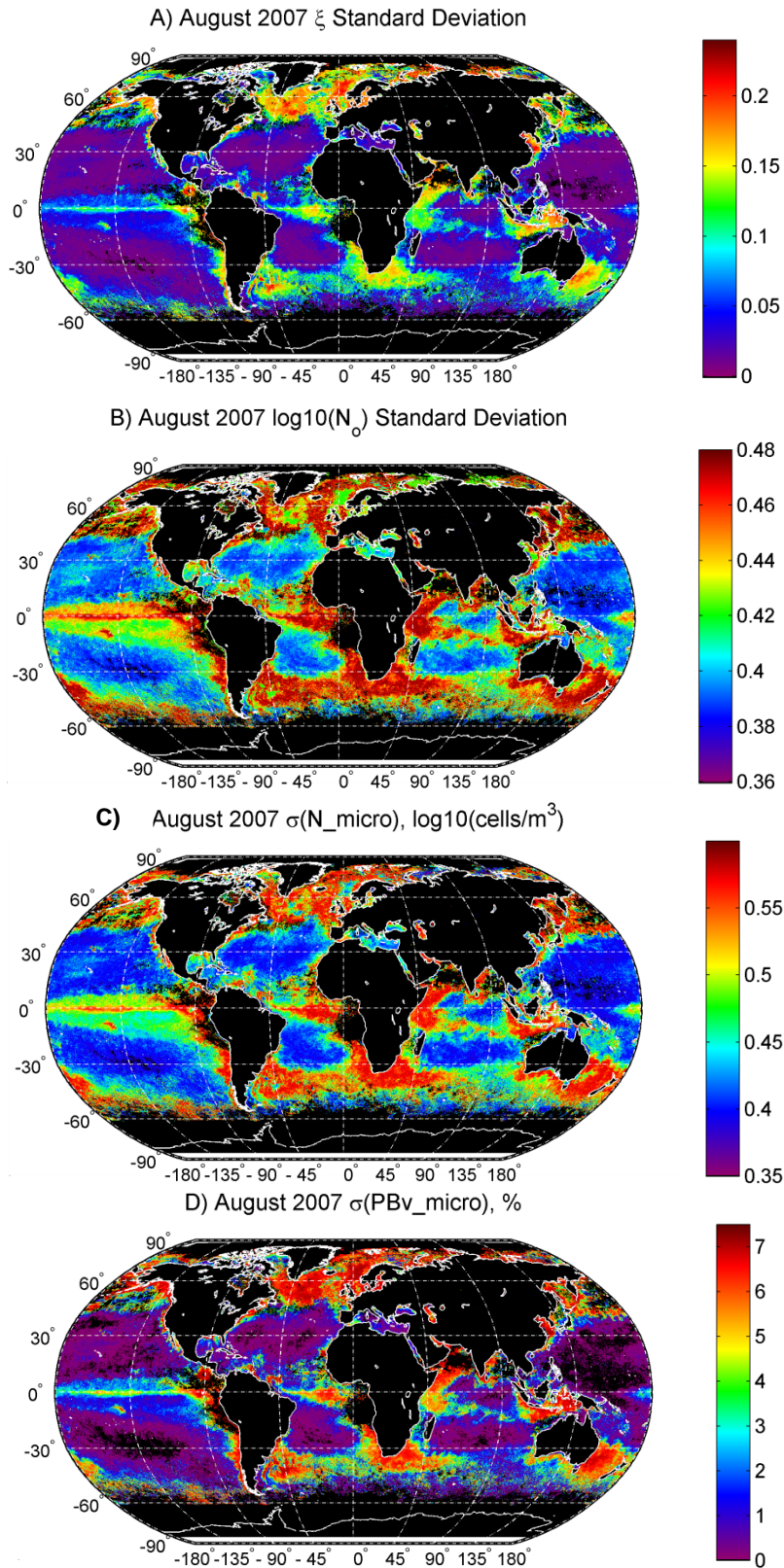


Figure 5. Examples of base and derived product endogenous uncertainty calculated using the Monte Carlo simulations. Global maps for August of 2007 of A) Standard deviation of the PSD Junge slope retrieval; B) Standard deviation of the  $\log_{10}(N_0)$  retrieval; C) Standard deviation of number concentration of microplankton-sized particles,  $\log_{10}(\text{particles}/\text{m}^3)$  – sizes between  $20 \mu\text{m}$  and  $50 \mu\text{m}$  were considered; D) Standard deviation (in percent) of the percent biovolume due to microplankton-sized particles.

Exogenous algorithm uncertainties are due to the assumptions of Mie theory and various other assumptions; they cannot be quantified easily. Firstly, there is uncertainty associated with the algorithm's input remote sensing products, imagery of the backscattering coefficient spectrum and the calculated  $b_{bp}(\lambda)$  spectral slope. It is outside the scope of this work to analyze these sources of uncertainty. The parameterization of the PSD is itself an assumption. In most cases real particle size distributions in the ocean usually follow the Junge parameterization closely (e.g. Sheldon, 1972; Gin et al., 1999; Cavender-Bares et al., 2001); however events such as phytoplankton blooms can cause spikes in the distribution. The algorithm presented here makes the assumption that the Junge-type PSD is valid over the entire diameter range of optically significant particles. Submicron particles play an important role in backscattering (Stramski et al., 2004); however most measurements and fits to a Junge slope do not include the submicron particles (e.g. the validation data sets used here). There is lack of agreement in the literature as to whether small particles exhibit even steeper slopes (Loisel et al., 2006), or whether the smallest particles are not as abundant as a hyperbolic PSD would predict (Risovic, 2002).

Mie theory assumes that all particles are spherical and homogeneous in their composition. Most particles, including phytoplankton are generally not spherical (Jonasz, 1987; Clavano et al., 2007) and/or homogeneous. The effects of non-sphericity on backscattering are difficult to generalize (Bohren and Huffamn, 1983, p. 401; Clavano et al., 2007). Clavano et al. (2007) conclude that backscattering of spheroids is likely to be up to 7x larger than equal-volume spheres. Regarding the effects of non-homogeneity on backscattering, the consensus in the literature is that non-homogeneous spheres tend to backscatter more than their homogeneous analogs (Kitchen and Zaneveld (1992); Quirantes and Bernard (2004); Quirantes and Bernard (2006)). Furthermore, spectral changes are reported (Quirantes and Bernard, 2004 and refs. therein). This is key, as the absolute values of the modeled and measured backscattering coefficients are not important for retrieving the Junge slope. Thus, the large errors in backscattering associated with shape or homogeneity effects would cancel out if the spectral shape is unaffected and the percent biovolume calculations will be unaffected.

Big particles, which tend to dominate in coastal and high productivity areas, are expected to deviate more from sphericity (Jonasz, 1987) and they are likely to also deviate more from homogeneity, for example by having a large vacuole. Thus, the exogenous uncertainty of the PSD model is likely to be largest in these zones, which coincides with larger endogenous uncertainties as well (Fig. 5). Other exogenous uncertainties, such as uncertainty in  $\tau$  are also likely to be highest in high productivity and coastal zones. In these situations it may be advisable to combine the algorithm presented here with alternative approaches, such as the pigment-based approach of Uitz et al. (2006), the absorption-based approach of Mouw et al. (pers. comm.), the reflectance-based approach of Alvain et al. (2005), as well as the holistic approach of Raitsos et al. (2008).

The ability to assess the total particle volume in any given size class presents unprecedented opportunities to estimate carbon biomass from space on global scales. Previous state-of-the-art studies have relied on constant scaling from the values of  $b_{bp}(\lambda)$  at one wavelength (Behrenfeld et al. (2005)). Their approach demonstrated the ability to estimate phytoplankton physiology from independent retrievals of Chl and living carbon biomass. The advance in counting particles from space presented here has the potential to improve quantitative estimation of phytoplankton carbon and physiology; carbon fixation rates and possibly export ratios can thus be assessed.

## Acknowledgements

The authors would like to acknowledge NASA for their financial support of this work. We acknowledge Hubert Loisel for providing us with their algorithm code, Emmanuel Boss and Wayne Slade for their optimized Mie code (based on Bohren and Huffamn, 1983), and Giorgio Dall'Olmo, Mike Behrenfeld, Emmanuel Boss and Greg Mitchell for providing us with validation data. We would also like to thank Emmanuel Boss and Craig Carlson

for useful discussions.

## References

- Alvain, S., C. Moulin, Y. Dandonneau, and F.-M. Bréon (2005), Remote sensing of phytoplankton groups in case 1 waters from global SeaWiFS imagery, *Deep Sea Res., Part I*, 52, 1989-2004.
- Azam, F. (1998), Microbial control of oceanic carbon flux: the plot thickens, *Science*, 280, 694–696.
- Behrenfeld, M. J., E. Boss, D. A. Siegel, and D. M. Shea (2005), Carbon-based ocean productivity and phytoplankton physiology from space, *Global Biogeochem. Cycles*, 19, GB1006, doi:10.1029/2004GB002299.
- Bohren, C.F. & Huffman, D.R. (1983), *Absorption and Scattering of Light by Small Particles*, New York, Wiley.
- Boss, E., Twardowski, M.S. & Herring, S. (2001), The shape of the particulate beam attenuation spectrum and its relation to the size distribution of oceanic particles, *Applied Optics*, 40, 4885–4893.
- Cavender-Bares K. S., A. Rinaldo, and S. W. Chisholm, (2001), Microbial size spectra from natural and nutrient enriched ecosystems, *Limnol. Oceanogr.*, 46, 778-789.
- Chisholm, S. W. (1992), Phytoplankton size. In P. G. Falkowski and A. D. Woodhead (Eds.), *Primary Productivity and Biogeochemical Cycles in the Sea*. New York, Plenum Press, p. 213-237.
- Clavano, W. R., Boss, E., and Karp-Boss, L. (2007), Inherent optical properties of non-spherical marine-like particles – from theory to observation, *Oceanography and Marine Biology, An Annual Review*, 45, 1–38.
- Eppley, R. W., Peterson, B. J. (1979), Particulate organic matter flux and planktonic new production in the deep ocean, *Nature*, 282, 677-680
- Falkowski, P.G., R.T. Barber, V. Semtacek (1998), Biogeochemical controls and feedbacks on ocean primary production, *Science*, 281, 200–206.
- Garver, S. A., and D. A. Siegel (1997), Inherent optical property inversion of ocean color spectra and its biogeochemical interpretation, 1, Time series from the Sargasso Sea, *J. Geophys. Res.*, 102, 18,607 – 18,625.
- Gin, Karina Y. H., Sallie W. Chisholm, Robert J. Olson, (1999), Seasonal and depth variation in microbial size spectra at the Bermuda Atlantic time series station, *Deep Sea Research Part I*, 46(7), 1221-1245.
- Gordon, H. R., O. B. Brown, R. H. Evans, J. W. Brown, R. C. Smith, K. S. Baker, and D. K. Clark (1988), A semianalytic radiance model of ocean color, *J. Geophys. Res.*, 93(D9), 10909–10924.
- Jonasz, M. (1987), Nonsphericity of suspended marine particles and its influence on light scattering, *Limnology and Oceanography* 32, 1059–1065.
- Junge, C.E. (1963), *Air Chemistry and Radioactivity*. New York: Academic Press.
- Karp-Boss, L., L. Azevedo, and E. Boss (2007), LISST-100 measurements of phytoplankton size distribution: evaluation of the effects of cell shape, *Limnol. Oceanogr.: Methods*, 5, 396–406.
- Kitchen, J. C. and J. R.V. Zaneveld (1992), A Three-Layered Sphere Model of the Optical Properties of

Phytoplankton, *Limnology and Oceanography*, **37**(8), pp. 1680-1690.

Loisel, H., and D. Stramski (2000), Estimation of the inherent optical properties of natural waters from irradiance attenuation coefficient and reflectance in the presence of Raman scattering, *Appl. Opt.*, **39**, 3001–3011.

Loisel, H., J.-M. Nicolas, A. Sciandra, D. Stramski, and A. Poteau (2006), Spectral dependency of optical backscattering by marine particles from satellite remote sensing of the global ocean, *J. Geophys. Res.*, **111**, C09024, doi:10.1029/2005JC003367.

Mie, G. (1908), Beiträge zur Optik trüber Medien, speziell kolloidaler Metallösungen, *Annalen der Physik*, **25**, 377–445.

Morel, A. (1973), Diffusion de la lumière par les eaux de mer. Résultats expérimentaux et approche théorique. In: *AGARD Lectures Series Optics of the Sea 6*, Technical Editing and Reproduction, London (1973), pp. 1–76 3.1–1.3.

Mouw et al. (2008), in prep...

Platt, T., Denman, K.L. (1977), Organization in the pelagic ecosystem, *Helgolander Wiss. Meeresunters* **30**, 575-581.

Quirantes, A. & Bernard, S (2004), Light scattering by marine algae: two-layer spherical and nonspherical models, *Journal of Quantitative Spectroscopy and Radiative Transfer* **89**, 311–321.

Quirantes, A. & Bernard, S (2006), Light-scattering methods for modelling algal particles as a collection of coated and/or nonspherical particles, *Journal of Quantitative Spectroscopy and Radiative Transfer* **100**, 315–324.

Raitsos, D. E., S. J. Lavender, C. D. Maravelias, J. Haralabous, A. J. Richardson, P. Reid (2008), Identifying four phytoplankton functional types from space: An ecological approach, *Limnol. Oceanogr.*, **53**(2), 605–613.

Reynolds, R. A., D. Stramski, and B. Greg Mitchell (2001), A chlorophyll-dependent semianalytical reflectance model derived from field measurements of absorption and backscattering coefficients within the Southern Ocean, *J. Geophys. Res.*, **106**(C4), 7125–7138.

Rinaldo, A., Maritan, A., Cavender-Bares, K. K. and Chisholm, S. W. (2002), Cross-scale ecological dynamics and microbial size spectra in marine ecosystems, *Proc. Roy. Soc. Lond. B.*, **269**, 2051-2059.

Risovic, D. (2002), Effect of suspended particulate-size distribution on the backscattering ratio in the remote sensing of seawater, *Appl. Opt.*, **41**, 7092–7101.

Sheldon, R.W., Prakash, A. & Sutcliffe, W.H. Jr. (1972), The size distribution of particles in the ocean, *Limnology and Oceanography*, **17**, 327–340.

Sieburth, J. M., V. Smetacek, and J. Lenz (1978), Pelagic ecosystem structure: heterotrophic compartments of the plankton and their relationship to plankton size fractions, *Limnol. Oceanogr.* **23**, 1256-1263.

Stramski, D., E. Boss, D. Bogucki, and K. J. Voss (2004), The role of seawater constituents in light backscattering in the ocean, *Prog. Oceanogr.*, *61*, 27– 55.

Uitz, J., H. Claustre, A. Morel, and S. B. Hooker (2006), Vertical distribution of phytoplankton communities in open ocean: An assessment based on surface chlorophyll, *J. Geophys. Res.*, *111*, C08005, doi:10.1029/2005JC003207.

Vidussi, F., H. Claustre, B. B. Manca, A. Luchetta, and J. C. Marty (2001), Phytoplankton pigment distribution in relation to upper thermocline circulation in the eastern Mediterranean Sea during winter, *J. Geophys. Res.*, *106*(C9), 19,939–19,956.



## An overview of video measurements of estuarine mud flocculation.

Andrew J. Manning<sup>1,2</sup>

1. Coastal Processes Research Group, School of Earth, Ocean and Environmental Sciences, University of Plymouth, Drake Circus, Plymouth, Devon, PL4 8AA, UK (contact address)
2. Coasts & Estuaries Group, HR Wallingford, Howbery Park, Wallingford, OX10 8BA, UK; andymanning@yahoo.com

### 1. Introduction

Tidal estuaries are dominated by muddy sediments; typically a mixture of clay minerals and various types of organic matter. When this cohesive sediment is entrained into suspension, the particles tend to flocculate (Kranck and Milligan, 1992). An individual floc may comprise up to  $10^6$  individual particulates. These flocs are less dense, but faster settling than their constituent particles. As flocs grow their effective density (i.e. bulk density less the water density) generally decrease (Tambo and Watanabe, 1979), but their settling rates rise due to a Stokes' Law relationship (Dyer and Manning, 1998). As a result, the sizes ( $D$ ) and settling velocities ( $W_s$ ) of flocs are regarded as key parameters in the modelling of cohesive sediment transport in coastal locations (e.g. Geyer *et al.*, 2000; Cheviet *et al.*, 2002).

Early attempts to measure floc settling velocities in situ by the gravimetric analysis of sediment samples collected by devices such as Owen tubes (Owen, 1976), were not wholly successful, and this data was at variance with the comparable laboratory based analysis of the time (e.g. the Andreason pipette method). Optical devices to measure concentration profiles such as those used by Spinrad *et al* (1989), Kineke *et al* (1989), and McCave & Gross (1991), have all sought to quantify the rate of water clearance, but they are unable, like earlier instrumentation, to measure particle size and settling velocity spectra both directly and simultaneously.

The development of optically-based video floc sampling devices during the past 15 years, has provided scientists with instrumentation with which floc size and settling velocities could both be measured simultaneously. This extended abstract will briefly review some of the recent insights made in the study of the flocculation process through the use of video image technology. Through computation processing, images from these video devices can be used to provide information of floc spectral physical properties, which include: floc size, settling velocity, effective density, porosity, floc mass and floc shape. Examples of both in situ estuarine measurements of flocs in turbulent tidal waters and flocs observed from controlled laboratory simulations will be presented.

### 2. Requirements For Reliable Floc Samplers

Mathematical descriptions of flocculation has proved very difficult, as it is a dynamically active process (van Leussen, 1988) which is directly influenced by environmental conditions. It is primarily dependent on a set of complex interactions among the sediment, fluid and the flow. Hayter and Mehta (1982) indicated that seventeen parameters need to be determined in order to fully describe a cohesive sediment type. Therefore the measurements of floc properties, in particular settling rates and mass settling fluxes (MSF), are a prerequisite for numerical sediment transport models.

The problem of obtaining good quality floc data which can be applied in numerical models is two-fold. Primarily, there are the problems attributed to the aggregate sampling, in particular the fragile, fastest settling, low (effective) density macroflocs (i.e.  $D > 160 \mu\text{m}$ ). Mud flocs, although stable in flowing turbulent water, can easily disaggregate when sampled. This is in response to the additional shear created during acquisition (Gibbs and

Konwar, 1983; Eisma *et al.* 1997). Secondly, there is the issue of using technology which permits the measurement of sufficient floc dynamical parameters which are of use in practical applications. For example particle sizers, although creating relatively low intrusion during floc sampling, only provide measurements of floc size. Thus no direct indication of settling velocity is given. Also laser-based particle sizers can struggle in highly turbid estuarine conditions. Few instruments satisfy these two requirements.

Video-based floc image sampling devices, such as the INSSEV instrument (Fennessy *et al.*, 1994; Manning and Dyer, 2002) and other such derivatives (e.g. van Leussen and Cornelisse, 1994; Mikkelsen *et al.*, 2004), can practically provide measurements of both floc size and settling velocity, simultaneously. From these observations, reliable estimates of floc effective density ( $\rho_e$ ) can be made using a modified Stokes' Law. Floc fragility has generally precluded the direct measurement of floc density. However, due to their low intrusive nature, video floc cameras tend to create minimal disturbance to the flocs during measurements of  $D$  and  $W_s$ , even when sampling flocs from within a naturally turbulent flow. A knowledge of effective density is very important in the calculation of vertical settling fluxes, as the rheological properties of flocculated matter are governed by volume concentrations, as opposed to mass concentrations (Dyer, 1989).

### 3. Example of In Situ Estuarine Video Floc Measurements

To illustrate how INSSEV can be applied to engineering and dredging related studies, the following example from Scheldt Estuary deployments will be used. To keep pace with growth in container shipments, construction of the Deurganckdok (DGD) tidal dock in the Port of Antwerpen (Belgium), commenced recently and the Flemish government commissioned a programme of field surveys. A significant feature of the Lower Sea Scheldt is the presence of a turbidity maximum zone (TMZ) with depth-averaged suspended particulate matter (SPM) concentrations spanning 50 to 500 mg l<sup>-1</sup>. This study examined the findings of the INSSEV floc property measurements for the HCBS1 (conducted in February 2005 prior to DGD construction) and HCBS2 (September 2006 when the dock was open and in operation) surveys. Data comparisons were made. Further details of these measurements are reported by Manning *et al.* (2007, 2009).

Floc size and settling velocity spectra were measured nominally 0.6 m above the estuary bed every 10-20 minutes (turbidity dependent), using various derivatives of the INSSEV instrument. This instrument permitted the accurate calculation of floc properties and MSF for modelling applications (Winterwerp *et al.*, 2006). To characterise the corresponding near-bed hydrodynamics, the turbulence was measured by a 3-D Acoustic Doppler Velocimeter and the turbidity monitored by an array of Optical Backscatter Sensors. Most sampling runs spanned a tidal cycle.

Within Deurganckdok (HCBS2), for 85% of the sampling run (ebb then early flood), the near bed turbulent shear stress fell within the zone Manning (2004) classifies as creating the optimum contacts and impact levels for maximising flocculation potential ( $\tau$  of about 0.2 – 0.4 Pa). This higher turbidity partly assisted in damping the ambient turbulence to the reported levels. Over 70% of the HCBS2 Day 3 MSF occurred during the TM passage through the dock on the flood. A peak settling flux of 13.2 gm<sup>-2</sup>s<sup>-1</sup> (35% of the time series total) was measured an hour into the flood.

The video floc images revealed that the majority of the matter suspended during the entire sampling run in DGD was in the form of macroflocs (as defined by Manning, 2001;  $D > 160 \mu\text{m}$ ), 53-85% by mass. These large DGD flocs fell at population-averaged  $W_{s_{\text{macro}}}$  of 2.5 mms<sup>-1</sup> to 5.3 mms<sup>-1</sup>. Thus the DGD floc dynamics produced a TMZ MSF over an order of magnitude greater than in the Scheldt TM.

When comparing the Scheldt Estuary and DGD floc dynamics over a tidal cycle, the floc data suggested the DGD macroflocs represented 73% of the ambient concentration and these macroflocs settled at a time series average  $W_{s_{\text{macro\_TS}}}$  of 3.5 mms<sup>-1</sup>. These macrofloc dynamics were 11% and 55% greater (respectively) than the Scheldt HCBS1 time series; these are both highly significant findings.

#### 4. Laboratory Video Floc Measurements

Although in-situ estuarine floc data is desirable for estuarine sedimentary process parameterisation, the use of laboratory analysis can provide a more controlled environment whereby a greater understanding of specific flocculation related phenomena can be studied in greater detail. There is a long history with laboratory studies on flocculation. These date from the early work of Krone (1963) where he performed extensive tests on cohesive sediments in a concentric cylinder viscometer, from which he derived the classic “orders of aggregation” flocculation theory. These are followed by examinations for the sanitary industry on polymeric flocculents (Argaman and Kaufman, 1970).

Much of the flocculation laboratory studies have been concerned with identifying how various estuarine mud floc properties react to changes in turbulence, concentration or both. These included research by: Gibbs, 1985; Tsai *et al.*, 1987; Burban *et al.* (1989), and Lick *et al.* (1993). However, these studies were unable to take advantage of low intrusive video floc sampling techniques, as no proven apparatus was available for laboratory use at that time. Therefore, as part of the European Commission MAST III funded COSINUS project (Berlamont, 2002), the LabSFLOC system was developed by Manning (2006). LabSFLOC is a laboratory derivation of the successful *in-situ* INSSEV instrument, which means that flocs properties can now also be measured in laboratory studies using suspended particulate matter (SPM) concentrations of several grammes per litre.

#### 5. Example of Laboratory Video Floc Measurements

The flocculation of suspended cohesive matter can significantly alter the sediment transport patterns throughout an estuary. Estuarine floc characteristics vary both temporally and spatially. It is recognised that turbulent shear generated within the water column has an influence on their properties, however very little is understood about the extent to which turbulence effects the structure of an individual floc population.

Therefore, as part of the European Commission MAST III funded COSINUS project (Berlamont, 2002), a number of laboratory studies on the settling and mass properties of flocculated sediments were conducted at the Laboratoire des Ecoulements Geophysiques et Industriels (LEGI) in Grenoble, France (Mory *et al.*, 2002).

The purpose of this laboratory study was to shear mud suspensions with turbulent shear ranging between  $3 \text{ s}^{-1}$  and  $21 \text{ s}^{-1}$  (approximate equivalent turbulent shear stress values: 0.18-2.4 Pa) with concentrations ranging from  $200 \text{ mg l}^{-1}$  to  $8.6 \text{ g l}^{-1}$ , within a Plexiglas tank, using an oscillating grid. Three different muds were used: Natural Tamar estuary (UK) mud, natural Gironde estuary (France) mud, and Gironde mud pre-treated to remove the organic component. The floc samples were then carefully extracted and examined in the clear water settling column of the LabSFLOC instrument (Manning, 2006). For more details of this experimental programme, refer to Gratiot and Manning (2004).

The results of the low concentration natural Tamar estuary (UK) mud when exposed to high shear, revealed the largest flocs produced were  $210 \mu\text{m}$  in diameter, which was smaller than the Kolmogorov eddy size of  $219 \mu\text{m}$  (Gratiot and Manning, 2007). The high velocity particle collisions resulted in both macroflocs ( $> 160 \mu\text{m}$ ) and microflocs having settling velocities of only  $0.6 \text{ mms}^{-1}$ . Lowering the shear for the same mud improved flocculation, and raised the macrofloc settling velocity to  $1.8 \text{ mms}^{-1}$ . This translated into the macroflocs constituting 64% of the floc mass, and 80% of the mass settling flux. In contrast, low concentrations of natural Gironde mud displayed significantly faster settling macroflocs at each turbulent shear increment than the Tamar mud, but the largest flocs were of the same order as the Tamar mud flocs. The suspended matter distribution showed the macroflocs only constituted 20-30% of the particulate mass. However, the fast settling rate transformed the low macrofloc mass into 62% of the settling flux. The removal of the organic matter from the Gironde mud resulted in very few flocs exceeding the pre-sieving mesh diameter of  $125 \mu\text{m}$ , at all concentration and shear stress levels. Results of the high concentration suspension experiments are reported by Gratiot and Manning (2008).

## 6. Summary & Conclusions

Quantitatively, video floc devices have the unique ability of allowing the size-spectrum division of the mass settling flux and associated floc characteristics to be calculated for a representative floc population. This is of great importance for both accurate numerical sediment transport model calibration and parameterisation (e.g. Baugh and Manning, 2007; Manning and Dyer, 2007).

From a qualitatively perspective, the high quality INSSEV and LabSFLOC video images have shown, at both a microscopic and macroscopic level, the complex variability of floc types which exist in an estuarine water column, both throughout changing tidal conditions and within an individual floc sample record. The INSSEV floc observations show that fractal-type representations (e.g. Kranenburg, 1994) may only provide a first approximation to the structure and characteristics of natural mud flocs. Therefore in situ floc data collection is a necessity and instruments which cannot measure all important floc components accurately can leave the analysis of such data open to misinterpretation.

The INSSEV and LabSFLOC instruments have significantly contributed towards the understanding of estuarine floc formation and the characteristics demonstrated by such flocs during varying levels of turbulence and suspended particulate matter concentrations. Successful floc measurements have been made from within both dilute suspensions and concentrated benthic suspension (CBS) layers close to the estuary bed; the latter where SPM concentrations can approach  $8 \text{ g l}^{-1}$ . Video floc analysis has been conducted on flocculated sediment (either in situ or in laboratory simulations) from the following estuarial locations: Tamar (UK), Gironde (France), Dee (UK), Scheldt (Belgium), Medway (UK), Orwell (UK), Sydney Harbour (Australia), and San Francisco Bay (USA); plus the non-tidal, freshwater environments of Lake Apopka (USA) and Lake Tahoe (USA).

## References

- Argaman Y., and Kaufman W. J., (1970). Turbulence and flocculation. *J. Sanitary Eng.*, ASCE, Vol. 96, 223-241.
- Baugh, J.V. and Manning, A.J., (2007). An Assessment of a New Settling Velocity Parameterisation for Cohesive Sediment Transport Modelling. *Continental Shelf Research*, doi:10.1016/j.csr.2007.03.003.
- Berlamont, J.E., (2002). Prediction of cohesive sediment transport and bed dynamics in estuaries and coastal zones with integrated numerical simulation models. In: J.C. Winterwerp and C. Kranenburg, (eds.), *Fine Sediment Dynamics in the Marine Environment - Proc. in Mar. Sci. 5.*, Amsterdam: Elsevier, pp. 1-4, ISBN: 0-444-51136-9.
- Burban P-Y., Lick W., and Lick J., (1989). The flocculation of fine-grained sediments in estuarine waters. *J. Geophys. Res.*, Vol. 94 (C6), 8323-8330.
- Cheviet, C., Violeau, D., Guesmia, M., (2002). Numerical simulation of cohesive sediment transport in the Loire estuary with a three-dimensional model including new parameterisations. In: *Fine Sediment Dynamics in the Marine Environment - Proc. in Mar. Sci. 5.*, Amsterdam: Elsevier, J.C. Winterwerp and C. Kranenburg, (eds.), pp. 529-543.
- Dyer, K. R., (1989). Sediment processes in estuaries: future research requirements. *J. Geophys. Res.*, Vol. 94 (C10), 14327-14339.
- Dyer, K.R., Manning, A.J., (1998). Observation of the size, settling velocity and effective density of flocs, and their fractal dimensions. *Journal of Sea Research* 41, 87-95.
- Eisma, D., Dyer, K.R., van Leussen, W., (1997). The in-situ determination of the settling velocities of suspended fine-grained sediment – a review. In: *Cohesive Sediments – Proc. of INTERCOH Conf.* (Wallingford, England), Chichester: John Wiley & Son, Burt, N., Parker, R., Watts, J. (Eds.), pp. 17-44.
- Fennessy, M.J., Dyer, K.R., Huntley, D.A., (1994). INSSEV: an instrument to measure the size and settling velocity of flocs in-situ. *Marine Geology* 117, 107-117.

- Geyer, W.R., Hill, P.S., Milligan, T.G., Traykovski, P., (2000). The structure of the Eel River plume during floods. *Continental Shelf Research* 20, 2067-2093.
- Gibbs, R.J. and Konwar, L.N., (1983). Sampling of mineral flocs using Niskin bottles. *Environ. Sci. Technol.*, 17 (6): 374-375.
- Gibbs, R.J., (1985). Estuarine flocs: their size settling velocity and density. *Journal of Geophysical Research* 90 (C2), 3249-3251.
- Gratiot, N., Manning, A.J., (2004). An experimental investigation of floc characteristics in a diffusive turbulent flow. *Journal of Coastal Research Special Issue*, SI 41, 105-113.
- Gratiot, N. and Manning, A.J., (2007). A laboratory study of dilute suspension mud floc characteristics in an oscillatory diffusive turbulent flow. *Journal of Coastal Research*, SI 50, 1142-1146.
- Gratiot, N. and Manning, A.J., (2008). Flocculation processes in concentrated benthic suspension layer (CBS) using a laboratory diffusive turbulent grid tank. In: T. Kudusa, H. Yamanishi, J. Spearman and J.Z. Gailani, (eds.), *Sediment and Ecohydraulics - Proc. in Marine Science 9*, Amsterdam: Elsevier, pp. 53-68, ISBN: 978-0-444-53184-1.
- Hayter, E.J., Mehta, A.J., (1982). Modelling of estuarial fine sediment transport for tracking pollutant movement. Final Report No. UFL/COEL-8L/009, University of Florida.
- Kineke, G.C., Sternberg, R.W. and Johnson, R., (1989). A new instrument for measuring settling velocity in-situ. *Marine Geology*, 90, 149-158.
- Kranck, K. and Milligan, T.G., (1992). Characteristics of suspended particles at an 11-hour anchor station in San Francisco Bay, California. *J. Geophys. Res.*, 97, 11373-11382.
- Kranenburg, C., (1994). The fractal structure of cohesive sediment aggregates. *Est. Coastal Shelf Sci.*, 39, 451-460.
- Krone, R.B., (1963). A study of rheological properties of estuarial sediments. Hyd. Eng. Lab. and Sanitary Eng. Lab., University of California, Berkeley, Report No. 63-68.
- Lick, W., Huang, H. and Jepsen, R., (1993). Flocculation of fine-grained sediments due to differential settling. *J. Geophys. Res.*, 98 (C6): 10,279-10,288.
- Manning, A.J., (2001). A study of the effects of turbulence on the properties of flocculated mud. Ph.D. Thesis. Institute of Marine Studies, University of Plymouth, 282p.
- Manning, A.J., (2004). The Observed effects of turbulence on estuarine flocculation. *J. Coastal Res. Special Issue*, SI 41, 90-104.
- Manning, A.J., (2006). LabSFLOC – A laboratory system to determine the spectral characteristics of flocculating cohesive sediments. *HR Wallingford Technical Report*, TR 156.
- Manning, A.J., Dyer, K.R., (2002). The use of optics for the in-situ determination of flocculated mud characteristics. *Journal of Optics A: Pure and Applied Optics* 4, S71-S81.
- Manning, A.J. and Dyer, K.R., (2007). Mass settling flux of fine sediments in Northern European estuaries: measurements and predictions. *Marine Geology*, 245, 107-122, doi:10.1016/j.margeo.2007.07.005.
- Manning, A.J., Martens, C., de Mulder, T., Vanlede, J., Winterwerp, J.C., Ganderton, P. and Graham, G.W., (2007). Mud floc observations in the turbidity maximum zone of the Scheldt Estuary during neap tides. *Journal of Coastal Research*, SI 50, 832-836.
- Manning, A.J., van Kessel, T., Sas, M. and Winterwerp, J.C., (2009). On the cohesive sediment properties in the Lower Sea Scheldt. In: Proc. Mar. Sci., INTERCOH 2007, Elsevier, Amsterdam, The Netherlands (*submitted for peer review*).

- McCave, I.N. and Gross, T.F., (1991). In-situ measurements of particle settling velocity in the deep sea. *Marine Geology*, 99, 403-411.
- Mikkelsen, O.A., Milligan, T., Hill, P., P. Moffatt, (2004). INSSECT - an instrumented platform for investigating floc properties close to the bottom boundary layer, *Limnology and Oceanography: Methods* 2, 226-236.
- Mory, M., Gratiot, N., Manning, A.J., Michallet, H., (2002). CBS layers in a diffusive turbulence grid oscillation experiment. In: *Fine Sediment Dynamics in the Marine Environment* - Proc. in Mar. Sci. 5., Amsterdam: Elsevier, J.C. Winterwerp and C. Kranenburg, (eds.), pp. 139-154.
- Owen, M.W., (1976). Determination of the settling velocities of cohesive muds. Hydraulics Research, Wallingford, Report No. IT 161, 8p.
- Spinrad, R.W., Bartz, R. and Kitchen, J.C., (1989). In-situ measurements of marine particle settling velocity and size distributions using the remote optical settling tube. *J. Geophys. Res.*, 94 (C1), 931-938.
- Tambo, N., Watanabe, Y., (1979). Physical characteristics of flocs-I. The floc density function and aluminium floc. *Water Research* 13, 409-419.
- Tsai, C.H., Iacobellis, S. and Lick, W., (1987). Flocculation of fine-grained sediments due to a uniform shear stress. *J. Great Lakes Res.*, 13: 135-146.
- van Leussen, W., (1988). Aggregation of particles, settling velocity of mud flocs: a review. In: Dronkers, J., van Leussen, W. (Eds), *Physical Processes of Estuaries*, Berlin: Springer, pp. 347-403.
- van Leussen, W., Cornelisse, J.M., (1994). The determination of the sizes and settling velocities of estuarine flocs by an underwater video system. *Neth. J. Sea Res.*, 31 (3), 231-241.
- Winterwerp, J.C., Manning, A.J., Martens, C., de Mulder, T., Vanlede, J., (2006). A heuristic formula for turbulence-induced flocculation of cohesive sediment. *Est. Coastal Shelf Sci.*, 68, 195-207.

## Settling column flocculation experiments

Francesca Mietta<sup>1</sup>, Johan C. Winterwerp<sup>1,2</sup> and Claire Chassagne<sup>1</sup>

1. Delft University of Technology, Environmental Fluid Mechanics section, The Netherlands
2. Deltares (formerly WL | Delft Hydraulics), The Netherlands

### Introduction

The understanding of flocculation is of primary importance in sediment transport and harbor siltation studies. Research on flocculation is approached through both in situ observation and laboratory studies. The flocculation time and the equilibrium floc size distribution depend on hydrodynamic conditions, residence time, sediment characteristics, sediment concentration and water properties such as pH and salinity. The conditions under which a population is being formed are difficult to establish by means of *in situ* experiments, because of the highly dynamic conditions in the field. On the other hand, laboratory experiments are usually done using small containers, i.e. jar tests, in which the residence time is limited by floc settling. Moreover, direct measurement, f. i. through optical methods, is difficult and sampling is necessary to establish the floc size distribution.

The experiments introduced in this paper have been done in a 4 m high settling column in which a homogeneous turbulence field is generated with an oscillating grid. Sediment is continuously injected at the top of the column and a long residence time of flocs in the turbulence field is ensured by the height of the column, enabling equilibrium conditions.

Optical measurements are done at the bottom of the column; no sediment sampling is required. Gray scale pictures of flocs are taken using a CCD camera and flocs are enlightened from the side by a laser sheet. Gray scale images are converted into black and white using a home made particle detection routine and the properties of flocs are derived from the black and white images.

### Experimental setup

The settling column is depicted in Figure 1 and described more in detail in Maggi et al. (2002). A highly-concentrated suspension, continuously mixed in the storage tank, is injected into the buffer tank mounted on top of the settling column, where two counter rotating vanes mix the suspension to ensure a uniform distribution at the top of the settling tube. The concentration in the column is kept constant to the test concentration  $c_c$  via a controlled system which tunes the intensity of the injection pump, taking into account the mass concentration measured in the buffer tank. The sediment concentration is measured with an OSLIM (Optical Silt Measuring Device, Deltares) at three different locations in the column: in the buffer tank to control the injection pump, in the middle and the bottom of the column.

The settling column is 4.7 m high and 280 mm in diameter. Herein, a homogeneous turbulence field, produced by an oscillating grid, induces flocculation. The grid is 4 m high and consists of meshes of 75 mm size with square cross-sectioned rods and deck distance of 75 mm. The relation between oscillation frequency and shear rate  $G$  has been obtained from LDA measurement in Maggi (2005).

At the bottom of the settling tube, a separation chamber allows the isolation of a small amount of flocs which are recorded in still water. The isolated flocs are enlightened by a thin laser sheet from the side and high resolution pictures are taken using CCD camera. The choice of the magnification factor has been done considering that a pixel should be small enough to record the smaller flocs and the 2048 x 2048 pixels window should be large enough to allow the recording of the same floc on consecutive images to measure the settling velocity. The pixel size is 3.16  $\mu\text{m}$ , which implies a window size of 6.4 mm x 6.4 mm.

The column is equipped with plugs at different heights and a sampling system which can be applied to the plugs

has been developed to observe the population. The system is conceived to minimize flocs breakup during sampling through compensation of the water pressure. The whole settling column is placed in a climatized room at  $T = 20\text{ }^{\circ}\text{C}$  to minimize temperature gradients and convective flows.

Experiments have been performed on kaolinite (China clay) with bulk density of  $\rho = 2560\text{ kg/m}^3$ , mineral size in the range of  $0.1 - 5\text{ }\mu\text{m}$  and primary particles of size  $L_p = 5 - 30\text{ }\mu\text{m}$ .

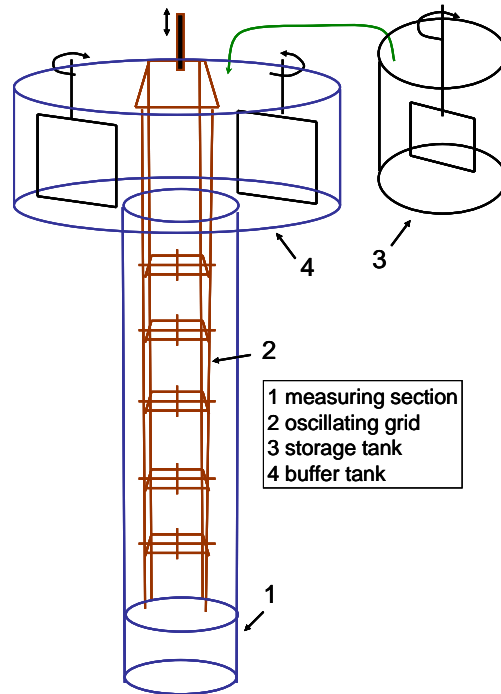
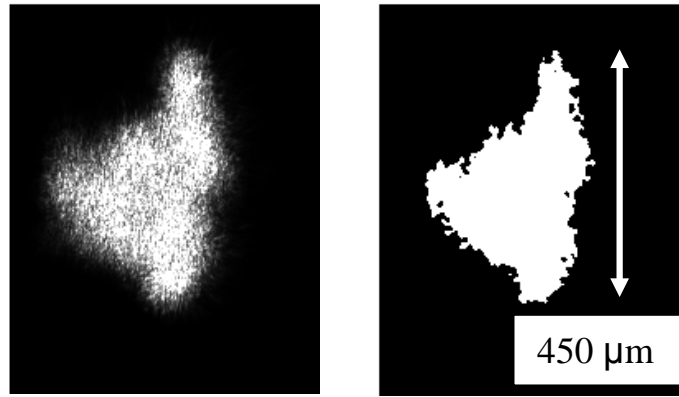


Figure 1. Sketch of the settling column

### Data processing

Our Matlab algorithm to process the gray scale images consists of three parts. The scope of the first part is data reduction while the second part aims at floc analysis and the third performs a statistical analysis. In the first part, flocs are isolated and the gray scale images, the size and the position of the window containing the flocs are saved in a separate data file. Flocs at the border of the image are not considered. Floc analysis is done on the reduced data and it starts with the detection and removal of the out of focus flocs. This is achieved through a combination of edge detection and threshold techniques. The black and white images are obtained through threshold and a morphological treatment, closure, bridging and cleaning, is applied to the converted image to reduce the noise, sharpen the image and better isolate the floc. Closure is used to remove small holes due to the irregular surface of flocs perpendicularly to the camera, bridging aims at connecting parts of the flocs separated by a darker area and cleaning is used to remove isolated pixels at the edges of the flocs. An example of flocs before and after processing is shown in Figure 2.



a) Gray Scale  
b) Black and white  
Figure 2. Image of a floc before and after conversion.

From the black and white image of the floc, floc size is computed as the size of the smallest box circumscribing the floc (box length) and the method developed by Maggi (2004) is used to derive the 3D fractal dimension of the flocs from the 2D projection. Statistical properties of the data are computed in the third part of the algorithm. The results shown in this paper focus on the floc size distribution.

## Results

In this section, the Floc Size Distribution (FSD) corresponding to two different shear rates is compared to the FSD at the entrance of the settling tube as well as to the one obtained with no turbulence. All data are normalized to have constant area under the distribution. In all cases the distributions can be approximated by one (mono-modal) or two (bimodal) log-normal distributions. An example of measured and fitted distributions is shown in Figure 3 for mono-modal distribution (a) and bimodal distribution (b). In the rest of this paper we plotted the log-normal distributions without data points to better visualize the results.

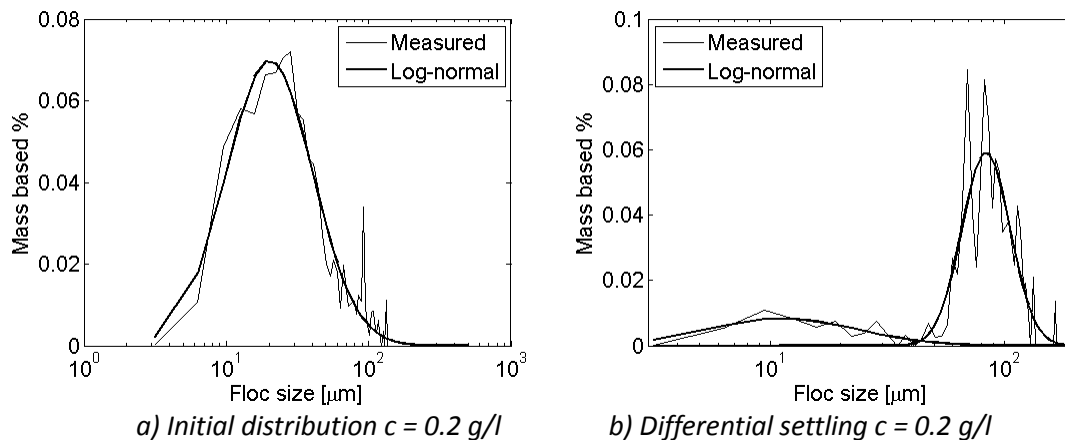


Figure 3. Fitted and measured floc size distributions in two different cases.

### Initial distribution

The floc size distribution at the entrance of the settling tube has been measured by removing the tube and placing the buffer tank straight on top of the measuring section. The injection system has been developed to minimize flocculation prior to the entrance in the settling tube and the mass based FSD corresponding to different sediment concentrations are shown in Figure 4 a) together with the FSD of kaolinite after ultrasonic treatment. This last distribution has been measured using a Malvern particle-sizer which can record particles with size range from nanometers to millimeters. The size of flocs at the entrance of the column is on average the double of the one obtained after ultrasonic treatment. This is due partly to the formation of small flocs in

the storage and buffer tanks and partly to the resolution of the camera used in the column which cannot see the smaller flocs. Although the standard deviation of the distributions varies with the concentration, the average values are rather constant.

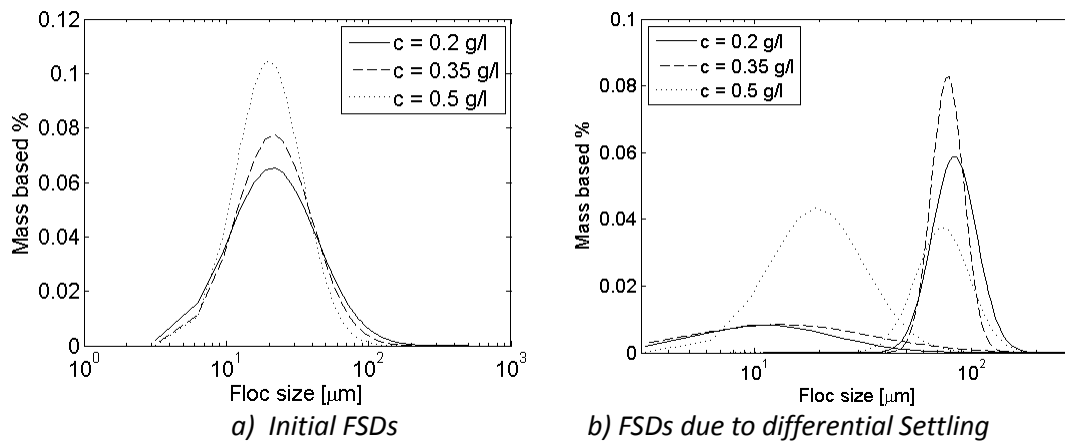


Figure 4. Mass based FSDs for different sediment concentrations.

### Differential settling

This experiment has been done with kaolinite settling in still water and no grid in the column; the same values of the concentration used in the first experiment have been used. Aggregation takes place when particles stick together after collision. The physical processes leading to particles collision are Brownian motion, negligible for particles larger than  $1\mu\text{m}$  (Hunt 1980), shear rate and differential settling. Collision due to differential settling occurs if large, rapidly settling particles get in contact with small, slowly settling particles. If no shear rate is applied, differential settling is the only process which can lead to particles aggregation.

For the three different concentrations considered, the observed mass based FSD becomes bimodal and the two distributions corresponding to the smaller and the larger peak are shown in Figure 4 b). The peak corresponding to small particles represents the non flocculated particles while the larger particles are formed through differential settling. The larger particles in the initial distribution settle faster than the small fraction and collect on their way the small particles. When the difference between the falling particles is large the trajectory of the small ones is deflected by the large ones falling and the probability of a collision is small (Stolzenbach and Elimelech, 1994). Formed flocs will more likely aggregate with other flocs rather than with primary particles and this would explain why a bimodal distribution is formed. These are the distributions after 4 m in the settling tube and further investigation is needed to understand if the equilibrium has been reached. To accelerate the flocculation process and investigate further the evolution of the distribution, the physicochemical properties of the suspension can be modified.

### Shear rate

The last experiment consists in the study of the influence of shear rate on flocculation and the sediment concentration used is  $c = 0.2\text{ g/l}$ . The time evolution of the average size of flocs is shown in Figure 5 together with the shear rate applied. Measurements are started after 30 hours from the beginning of the injection. This allows to reach a steady state and to ensure that the concentration is homogeneous throughout the column. The population reacts to variations in shear rate, and the steady state is reached within a few hours. The floc size distributions corresponding to the equilibrium population for different shear rates are shown in Figure 6 a). A decrease in shear rate leads to increase of the size distribution, Step 1 to Step 2; the process is reversible. The distribution obtained with a value of  $G$  equal to the initial value, Step 3, is very close to the initial distribution. The maximum size of particles is the same in Step 1 and 3 but in Step 1 there are more small particles than Step 3. When the shear rate increases all the large flocs are broken while not all the small flocs are broken to primary particles.

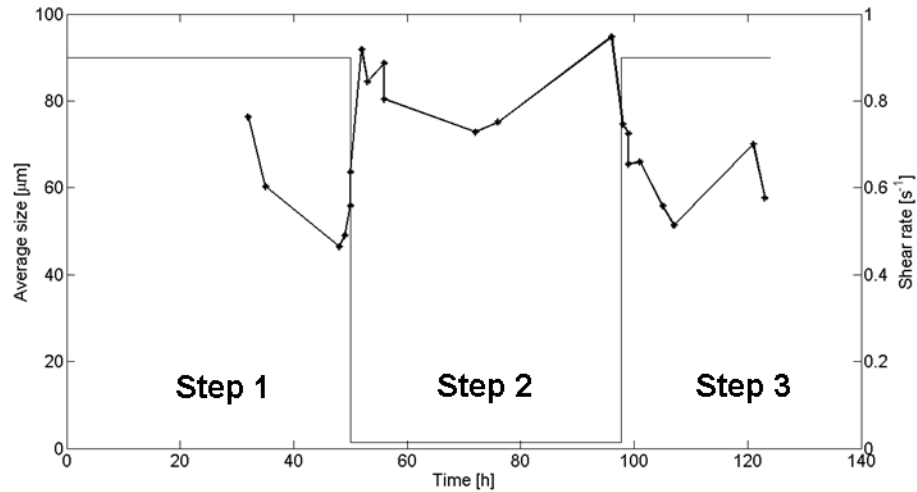


Figure 5. Time evolution of the average size at the bottom of the settling column (thick line) and applied shear rate (thin line).

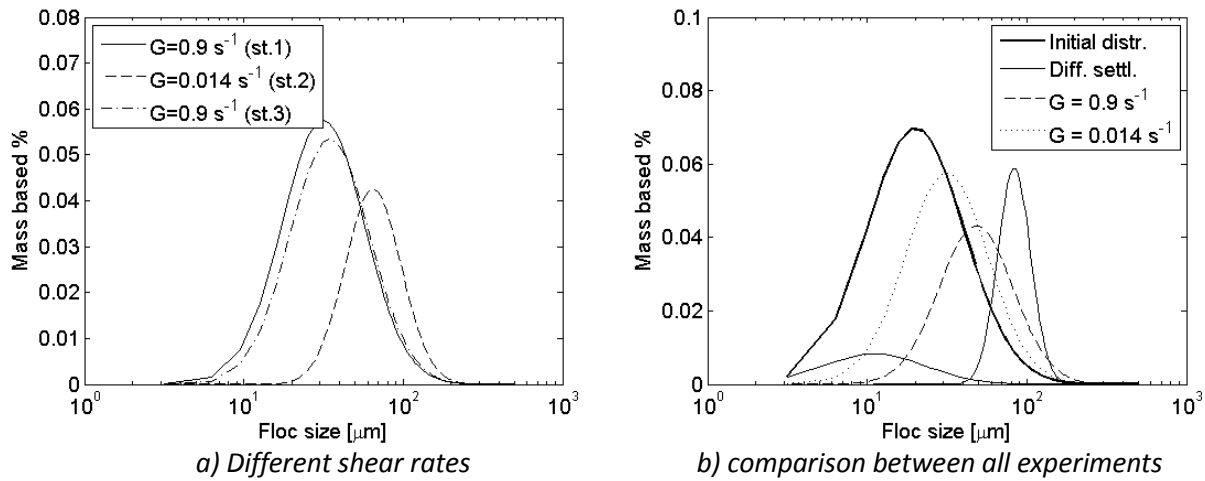


Figure 6. Mass based FSDs at  $c = 0.2$  g/l. In figure b) two log-normal distributions are plotted to represent the distribution obtained through differential settling.

### Discussion

In Figure 6 b) the distribution at the entrance of the column, the distribution obtained with differential settling and the ones corresponding to two different  $G$  values at  $c = 0.2$  g/l are compared. Flocculation takes place in the column when either differential settling or shear rate induces particles collision. The floc size increases with decreasing shear rate and the largest flocs are present when the shear rate is null and aggregation is due to differential settling. In still water, no breakup takes place and flocs can grow larger if there is aggregation as it is the case for differential settling.

### Conclusions and applications

The settling column is an efficient setup to reproduce the estuarine conditions with full control on the physical parameters. The most common experimental setup for flocculation is the stirred tank. Particles in a stirred tank are kept in suspension by the propeller and the dimensions of the tank are reduced to allow a more homogeneous turbulent field. If the jar is small the residence time of the sediment in the jar at low shear rate is small and this affects the measured distribution, especially for low flocculation rates. Moreover, it is very difficult to investigate the effect of differential settling within jars and similar devices. The results introduced in this paper show that the settling column can be a suitable instrument for investigation of flocculation at low or

null shear rate.

The data processing routine developed for this work allows for an automatic isolation of the in-focus flocs and a conversion from gray scale to black and white. This is done using a more compact dataset composed of the isolated gray scale flocs solely rather than of the full images.

Shear rate is important for the flocculation process and the time needed to reach equilibrium under the conditions used in the experiments here introduced is of the order of a few hours, comparable to the time scale of tidal variations. These conditions are close to the ones which can be observed in estuaries. To investigate the effect of tidal variations on the cohesive sediment our next step will therefore be to apply a variable shear rate to the settling column and monitor the variations in floc size.

### **Acknowledgments**

This research is supported by the Dutch Technology Foundation STW, applied science division of NWO and the Technology Program of the Ministry of Economic Affairs.

### **References**

Hunt J. R. (1980). Prediction of oceanic particles size distribution from coagulation and sedimentation mechanisms. *Advances in chemistry 189 - Particles in Water*, M. D. Kavanaugh and J. T. Kake Editors, *American Chemical Society*, 243-257.

Maggi F., Winterwerp J.C., Fontijn H.L., van Kesteren W.G.M. and Cornelisse J.M. (2002). A settling column for turbulence-induced flocculation of cohesive sediments. *Proceedings of HMEM2002 Conference*, Wahl T.L., Pugh

C.A., Oberg K.A. and Vermeyen T.B. Eds., Estes Park, Colorado, paper 93. DOI 10.1061/40655(2002)34.

Maggi F. and Winterwerp J. C.(2004). Method for computing the three-dimensional capacity dimension from two dimensional projections of fractal aggregates. *Physical review E* 69, 011405.

Maggi F. (2005). Flocculation dynamics of cohesive sediments. PhD Thesis TU Delft, Delft, The Netherlands.

Stolzenbach K .D. and Elimelech M. (1994). The effect of particle density on collisions between sinking particles: implication for particles aggregation in the ocean. *Deep Sea Research* 1, 41 (3), 469-483.

## **In the eye of the beholder: size distributions as seen by LISST and DFC.**

**TG Milligan<sup>1</sup>, PS Hill<sup>2</sup>, BA Law<sup>1</sup>, E Boss<sup>3</sup>**

1. Fisheries and Oceans Canada, Bedford Institute of Oceanography, PO Box 1006, Dartmouth NS, B2Y 4A2, Canada
2. Dalhousie University, Halifax NS, B3H 4J1, Canada
3. University of Maine, Orono ME, 04469-5741 USA

Studies carried out on in situ particle size with a LISST and a digital floc camera (DFC) have used a simple method to overlap the size distributions to produce a size spectra over a range from approximately 2.5  $\mu\text{m}$  – 1 cm. Under the arbitrary assumption that the DFC is sensing concentration correctly, a constant is determined for the region of overlap between the two size spectra that allows the LISST data to be “moved” to the DFC data. The data are re-calculated and a new volume (area) vs diameter spectrum is plotted. Recent improvements to the resolution of the DFC have increased the region of overlap. Using a suite of over 6000 concurrent DFC images and LISST size spectra collected as part of the ONR funded OASIS project conducted at the Martha’s Vineyard Coastal Observatory we re-examine the effectiveness of using a simple overlap method to create full in situ size spectra.



## Measuring the Mass Specific Absorption Spectra of Organic Detritus

Benjamin D. Moate<sup>1</sup>

1. Proudman Oceanographic Laboratory, Joseph Proudman Building, 6 Brownlow Street, Liverpool L3 5DA, UK.

Suspended particulate matter (SPM) typically includes mineral suspended solids (MSS), phytoplankton cells, and organic detritus. Interest in remote sensing primary productivity and suspended sediments has led previous studies to determine the mass specific absorption coefficients of both phytoplankton pigments ( $a_{PIG}^*$ ) and MSS ( $a_{MSS}^*$ ), using either statistical or physical retrieval methods. Statistical methods utilise multiple linear regression of SPM absorption on concentrations of MSS and phytoplankton pigments, whilst physical methods often utilise Quantitative Filter Pad (QFP) samples that are bleached and combusted to obtain absorption by phytoplankton pigments ( $a_{PIG}$ ) and MSS ( $a_{MSS}$ ) respectively. In contrast, there remains no equally simple method for determining the mass specific absorption for organic detritus ( $a_{OD}^*$ ). This is because the mass concentration of organic detritus ([OD]) can not be measured, and hence although organic detritus absorption ( $a_{OD}$ ) can be measured,  $a_{OD}^*$  can not be obtained. The problem is therefore two-fold: neither  $a_{OD}^*$  nor [OD] can currently be measured practically, and therefore optical models can not include organic detritus in a physically correct manner. The present study provides a solution to this problem, and presents a simple, statistical extraction method for the retrieval of  $a_{OD}^*$ . Here,  $a_{OD}$  was obtained by subtracting  $a_{PIG}$  and  $a_{MSS}$  from SPM absorption for a number of QFP samples. To obtain  $a_{OD}^*$ , a multiple linear regression of  $a_{OD}$  on a proxy for [OD] was performed. The resulting  $a_{OD}^*$  spectra appears physically correct, decreasing approximately exponentially from blue to red wavelengths. With  $a_{OD}^*$  determined, [OD] can be obtained by dividing measured  $a_{OD}$  by  $a_{OD}^*$ .



## Measurements of the acoustic backscattering characteristics of suspensions having broad size distributions

Benjamin D. Moate<sup>1</sup> and Peter D. Thorne<sup>1</sup>

1. Proudman Oceanographic Laboratory, Joseph Proudman Building, 6 Brownlow Street, Liverpool L3 5DA, UK.

### Abstract

Measurements are presented from a multi-frequency acoustic backscatter study of aqueous suspensions of spheres having broad particle size distributions. Exploiting the backscattered sound from a homogenous suspension, measurements were derived of the ensemble backscatter form function and total normalized scattering cross-section, over the probability density function of the particles in suspension. Two different size distribution types were examined, namely log-normal and bi-modal distributions, each covering a range of particles sizes similar to those observed to occur in marine environments near the seabed. The measurements presented here were used to assess the measurement methodology and are compared to predictions from spherical scattering theory. The results show that the ensemble scattering parameters are significantly altered by the presence of a size distribution.

### 1. Introduction

Suspended sediments significantly scatter underwater sound at megahertz frequencies, with both the mass concentration and the size of the sediments in suspension controlling the backscattered intensity (Hay, 1991; He and Hay, 1993; Thorne and Buckingham, 2004). In recent years, this premise has led to the development of multi-frequency Acoustic Backscatter Systems (ABS), designed to collect vertical profiles of suspended sediments in the bottom 1 – 2 m above the bed (Hess and Bedford, 1985; Hay, 1991; Schat, 1997; Thorne and Hardcastle, 1997). Acoustics offer the advantage that measurements can be obtained non-intrusively at high spatial and temporal resolution, with ABS typically providing measurements at centimetric resolution at turbulent and inter-wave timescales (Thorne and Hanes, 2002).

Non-empirical estimates of suspended concentration and particle size can be obtained from multi-frequency ABS data by performing analytical inversions of the backscattered acoustic signal (Crawford and Hay, 1993; Thorne and Hardcastle, 1997; Thosteson and Hanes, 1998). Such inversions require knowledge of the acoustic scattering properties of the particles in suspension, which are usually described in terms of two dimensionless parameters, namely the backscatter form function,  $f$ , and the normalised total scattering cross-section,  $\chi$ . Physically,  $f$  describes the backscattering characteristics of a particle relative to its geometrical size, whilst  $\chi$  quantifies the acoustical scattering by a given particle, over all angles, relative to its cross-sectional area, and is proportional to attenuation due to particle scattering losses.

For particles with regular shapes such as spheres, algebraic expressions describing  $f$  and  $\chi$  can be derived from acoustic scattering theory (Sheng and Hay; 1988; Thorne et al, 1993). Theoretical predictions show  $f$  and  $\chi$  to be significant functions of scatterer size and sound wavelength, and both are consequently often expressed in terms of a dimensionless parameter,  $x = ka$ , where  $k$  is the wavenumber and  $a$  the particle size. Measurements of  $f$  obtained from single spheres have shown excellent agreement with theoretical predictions, over a range of sound frequencies and particle sizes, and for a variety of materials (Thorne et al, 1992). In contrast, for irregularly shaped particles such as natural sediments, no analytical theoretical solution exists to describe  $f$  and  $\chi$ . Consequently, to facilitate the inversion of marine ABS data,  $f$  and  $\chi$  have been determined experimentally (Flammer, 1962; Hay, 1991; He and Hay, 1993; Schaafsma and Hay, 1997; Thorne and Buckingham, 2004). To enable the variation of  $f$  and  $\chi$  with  $x$  to be inferred for sediments, these experiments have focused on

sediments sieved into narrow  $\frac{1}{4} \Phi$  size fractions, where  $\Phi = -\text{Log}_2(d)$ , with  $d$  the particle diameter in mm. These  $\frac{1}{4} \Phi$  size fractions produce a nominally single size in suspension, with the standard deviation of the particle size distribution being  $\sim 5\%$  of the mean size.

Of course, natural marine suspensions contain a much broader range of particle sizes than those present in  $\frac{1}{4} \Phi$  size fractions (Bale and Morris, 1987; Krank and Milligan, 1991; Stavn and Keen, 2004). Measurements have shown that the size distributions of near-bed suspended sediments are often similar and related to the size distribution of the bed material (Sengupta, 1979; Krank and Milligan, 1991), which consistently covers a broad range of sizes throughout the worlds seas and oceans (Sval'nov and Alekseeva, 2006). For a suspension containing a range of particle sizes, the ensemble  $f$  and ensemble  $\chi$ , hitherto referred to as  $f_0$  and  $\chi_0$  respectively, can theoretically be determined by integrating values of  $f$  and  $\chi$  (being the single size or  $\frac{1}{4} \Phi$  size fraction values) over the particle size probability density function (PDF) of the suspension (Sheng and Hay, 1988; Thorne and Campbell, 1992; Thorne and Meral, 2008). The usual derivation of the integration expressions for  $f_0$  and  $\chi_0$  make use of an assumption that the particles are spherically shaped however, and there has been no reported validation of these theoretical expressions by direct measurement of  $f_0$  and  $\chi_0$  for broad size distributions of either spherical, or irregularly shaped particles. This is the aim of the current work. Here, we outline the adopted methodology and present our initial results obtained from suspensions of spheres using a four frequency ABS (0.5, 1, 2, and 4 MHz).

## 2. Modelling $\chi_0$ and $f_0$

For a suspension of spheres, the ensemble normalised total scattering cross-section,  $\chi_0$ , and the ensemble form function,  $f_0$ , are theoretically (Sheng and Hay, 1988; Thorne et al, 1993):

$$\chi_0 = \frac{\int_0^\infty an(a)da \int_0^\infty a^2 \chi(a)n(a)da}{\int_0^\infty a^3 n(a)da} \quad (1)$$

$$f_0 = \left[ \frac{\int_0^\infty an(a)da \int_0^\infty a^2 f(a)^2 n(a)da}{\int_0^\infty a^3 n(a)da} \right]^{1/2} \quad (2)$$

where  $a$  is particle radius, and  $n(a)$  is the PDF of the suspended size distribution. Thus, to determine  $\chi_0$  and  $f_0$  at a given sound frequency, for a suspension of spheres with a given PDF, Equations 1 and 2 are evaluated using the theoretical total normalised scattering cross-section described by (Hay and Mercer, 1985; Thorne and Campbell, 1992):

$$\chi(a) = \frac{2}{(ka)^2} \sum_0^\infty (2n+1) |b_n|^2 \quad (3)$$

and the backscattered form function described by:

$$f(a) = \frac{2}{ika} \sum_{n=0}^\infty (2n+1)(-1)^n b_n \quad (4)$$

where the coefficient  $b_n$  is provided by Gaunaurd and Uberall (1983).

### Measuring $\chi_0$ and $f_0$

All measurements of the scattering properties of suspended particles were obtained in a sediment tower specifically designed for ABS measurements. This apparatus has been described previously (Thorne and Buckingham, 2004), and generates a homogenous suspension within the immediate 1 m or so below the ABS transducers, the uniformity of which has been examined and presented elsewhere (Betteridge et al, 2008). The distributions examined in the present work were created by mixing together appropriate proportions of  $\frac{1}{4} \Phi$  size fractions, obtained by initially sieving the parent population of the spheres. The breadth of the distributions was characterised using the relative standard deviation,  $\kappa$ , being the ratio of the standard deviation,  $\sigma$ , to the mean size  $a_0$ . Three separate size distributions were created, a log-normal distribution and two bi-modal distributions, the PDFs of which are presented in Figure 1.

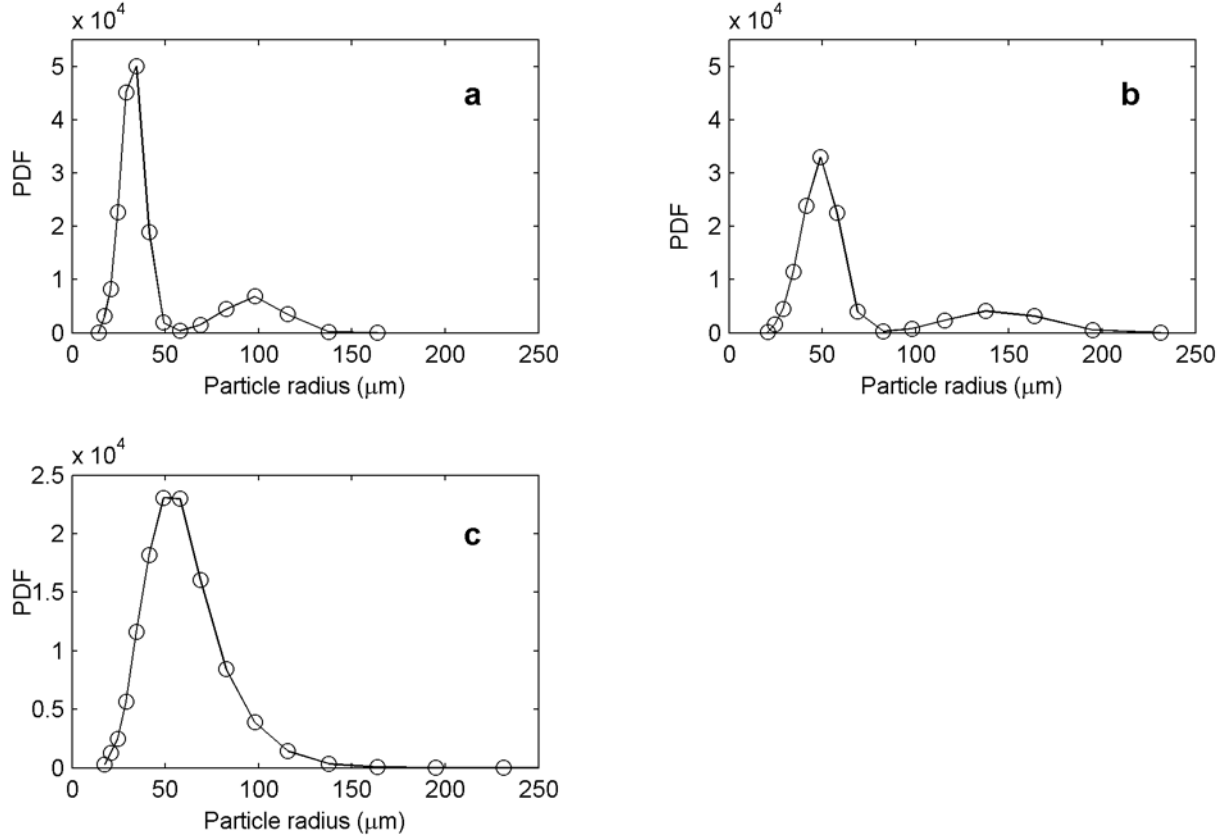


Figure 1 – Probability density function (PDF) for each size distribution examined. Distribution type and mean size were as follows: (a) bi-modal,  $a_0=49 \mu\text{m}$ , (b) bi-modal,  $a_0=73 \mu\text{m}$ , and (c) log-normal,  $a_0=61 \mu\text{m}$ . The solid line in each plot is for visualisation purposes only.

Assuming that the phase of the backscattered sound received by the ABS is randomly distributed between  $0 - 2\pi$ , the root mean square of the backscattered voltage can be written as (Thorne and Hanes, 2002):

$$V_{RMS} = \frac{K_t M^{1/2} f_0}{r \psi \sqrt{\rho_0 a_0}} e^{-2r(\alpha_w + \alpha_s)} \quad (5)$$

where  $r$  is the range from the transducer,  $M$  the mass concentration of suspended sediment,  $\rho_0$  the density of the sediment grains,  $\alpha_w$  is the absorption by water,  $\psi$  accounts for the departure from spherical spreading in the transducer near field (Downing et al, 1995), and  $K_t$  is a calibration constant.  $K_t$  incorporates the electronic response, the transmit and receive sensitivities, and the directivity response (beam pattern) of the transducer,

and is specific to a given ABS system. The normalised total scattering cross-section is contained within the sediment attenuation term,  $\alpha_s$ , given by:

$$\alpha_s = \frac{3\chi_0 M}{4\rho_0 a_0} \quad (6)$$

where all other terms are as previously defined.

Rearranging Equation 5, and taking the natural log transformation yields a linear function of  $\text{Log}_e(V_{RMS} r \psi)$  with range  $r$  from the transducer:

$$\text{Log}_e(V_{RMS} r \psi) = \text{Log}_e\left(K_t M^{1/2} f_0 / \sqrt{\rho_0 a_0}\right) - 2r\alpha \quad (7)$$

with  $\alpha = \alpha_w + \alpha_s$ . Thus, by measuring the variation of  $V_{RMS}$  with  $r$ , for a homogenous suspension of glass spheres, a profile mean value of  $\chi_0$  can be calculated from the slope of Equation 7, using Equation 6, with  $\alpha_w$  taken from the literature (Kaye and Laby, 1986). In this way, accurate estimates of  $\chi_0$  can be obtained providing that  $\alpha_s \geq \alpha_w$ . Where  $\alpha_s < \alpha_w$ , small errors in the estimate of the slope  $\alpha$  can diminish the accuracy of the estimated  $\chi_0$ . This limitation, combined with the maximum sediment concentration that could be maintained in suspension being  $\sim 1 - 2 \text{ gl}^{-1}$ , meant that measurements of  $\chi_0$  were only obtainable at the highest operating frequency of 4 MHz in the present study. Consequently, in order to utilise the ABS data at the other operating frequencies, the approach adopted in this study was to calculate  $f_0$  from the measured  $V_{RMS}$  by directly rearranging Equation 5 for each ABS bin, and using modelled values of  $\chi_0$  at the other (lower) operating frequencies to compute  $\alpha_s$ .

### 3. Results

Figure 2a shows a comparison between the theoretical predictions of  $\chi_0$  and measurements derived from the three separate suspensions examined (shown in Figure 1). For the log-normal and both bi-modal size distributions studied,  $\kappa$  was 0.36 and 0.61 respectively. No estimates of  $\chi_0$  could be derived at operating frequencies  $< 4 \text{ MHz}$  due to  $\alpha_s \leq \alpha_w$  at the suspended particle concentrations used. Whilst the number of measurements are limited, Figure 2a shows near perfect agreement between the measurements and the theoretical predictions. The error bars on all measured values denote  $\pm$  one standard deviation about the mean of measurements obtained at two different concentrations of  $\sim 0.5$  and  $1 \text{ gl}^{-1}$  for all three distributions shown in Figure 2a. By including the theoretical predictions for each size distribution as a function of  $x_0 = \kappa a_0$ , Figure 2a clearly illustrates the effect that the presence of a size distribution has on  $\chi_0$ . Relative to that predicted for a single size sphere, for both the log-normal and bi-modal distributions studied,  $\chi_0$  is elevated at values of  $x_0 < 2$ , whilst generally being diminished at  $x_0 > 2$ . Indeed, it can be seen in Figure 2a that at  $x_0 < 0.3$ , the theoretical predictions show that for the bi-modal distributions  $\chi_0$  is enhanced by an order of magnitude relative to the single size sphere case. Figure 2a also illustrates that as the relative standard deviation of the suspended size distribution is increased, the degree to which the ensemble scattering is altered relative to single size sphere scattering is also increased.

Measurements of  $f_0$ , derived from the acoustic backscatter data obtained from the same suspensions, are presented in Figure 2b. Figure 2b contains measurements of  $f_0$  obtained from all four ABS operating frequencies. This was achieved at all operating frequencies by modelling  $\chi_0$  using Equation 3 in Equation 1 with the appropriate PDFs, and deriving  $f_0$  from the measured acoustic backscatter by re-arranging Equation 5. Figure 2b shows close agreement between the measured values of  $f_0$  derived in this way, and the theoretical predictions, for both size distribution types and across an order of magnitude range in  $x_0$ . The effect of the presence of a size distribution on the backscattering is similar to that described above for  $\chi_0$ , namely backscattering is generally enhanced at  $x_0 < 2$ , whilst generally being diminished at  $x_0 > 2$ , with the degree of

alteration increasing as the size distribution width (relative standard deviation) increases. These changes are not as pronounced for  $f_0$  as they are for  $\chi_0$  however, with  $f_0$  being enhanced at low  $x_0$  by up to a factor of 3 for the bi-modal distributions shown in Figure 2b.

The theoretical predictions for  $\chi_0$  and  $f_0$  in Figure 2 show that an additional effect of the presence of a size distribution is to smooth the variations in the geometric scattering regime ( $x_0 > 1$ ) which are normally associated with sphere resonance (Thorne et al, 1993). The degree to which these sphere resonances are smoothed differs between the log-normal and bi-modal distributions (see Figure 2b), with a greater degree of smoothing being evident for the log-normal distribution despite the bi-modal distributions being broader, as indicated by the relative standard deviations of the distributions. This suggests that size distribution type may be an important mechanism in this smoothing process.

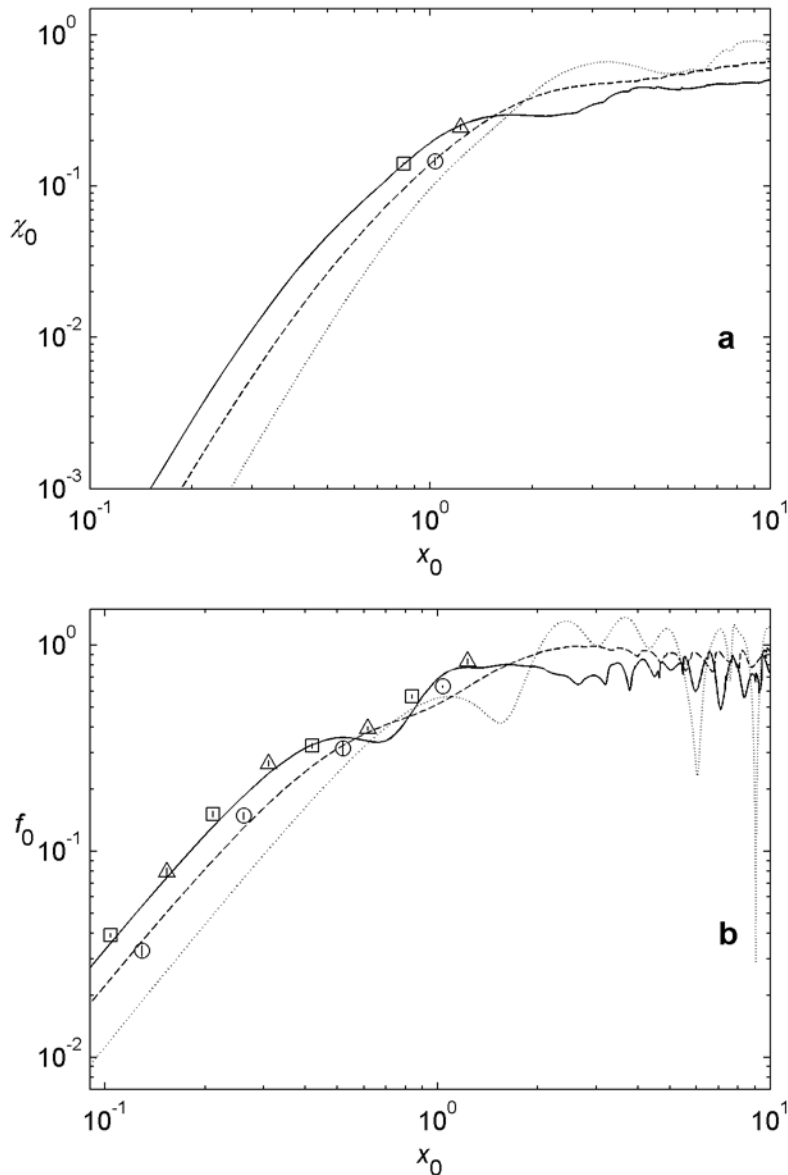


Figure 2 - Measurements of (a)  $\chi_0$ , and (b)  $f_0$ , obtained from the log-normal (circles) and bi-modal distributions (triangles and squares). The theoretical predictions for the log-normal (dashed lines) and bi-modal (solid lines) distributions are also shown. The dotted lines show the theoretical  $\chi$  and  $f$  for a single size sphere.

#### 4. Discussion

The results obtained from our sphere experiments were used to assess the measurement setup and adopted methodology. The scattering properties of spheres are well documented, and the integration theory has been tested previously for both narrow  $\frac{1}{4} \Phi$  size fractions (Thorne and Buckingham, 2004) and for a slightly broader Gaussian distribution having  $\kappa = 0.2$  (Thorne and Campbell, 1992). In this study, we evaluated Equations 1 and 2 for suspensions of spheres using three broader distributions with more complex size distribution types, namely log-normal and bi-modal distributions. For all three distributions, close agreement was observed between the measured scattering parameters,  $\chi_0$  and  $f_0$ , and their respective theoretical predictions. The near-perfect agreement between the modelled and measured values of  $\chi_0$  obtained at 4 MHz (Figure 2a), justified the approach of modelling  $\chi_0$  to obtain  $f_0$  from the ABS measurements at the lower operating frequencies, and suggested this would not introduce any significant source of error, or biasing.

Some degree of scatter did exist in the comparisons of measured and predicted  $f_0$  however (Figure 2b). It is possible that some or all of this scatter was associated with small uncertainties in the ABS calibration constants,  $K_t$ . As the measured values of  $f_0$  were inversely proportional to  $K_t$ , any error in  $K_t$  would propagate during the calculation of  $f_0$ , with the error being potentially different for each operating frequency. In contrast, the measured values of  $\chi_0$  were completely independent of  $K_t$ , as  $\chi_0$  was obtained from the slope of Equation 7 only. Following the usual rules of uncertainty propagation, i.e. that fractional uncertainties add in quadrature (Taylor, 1997), we estimate that if the  $K_t$  values were offset by only 1 standard deviation, the corresponding uncertainty in  $f_0$  would be  $\sim 10\%$  for each of the four operating frequencies. Errors of this magnitude would account for most of the departures from the theoretical predictions observed in Figure 2b.

The theoretical predictions show that the effect of a size distribution is to typically enhance scattering in the Rayleigh regime ( $x_0 < 1$ ), whilst diminishing scattering in the geometrical regime ( $x_0 > 1$ ). Our measurements would appear to validate these theoretical predictions, at least in the Rayleigh regime, for two different size distribution types, and for size distributions with  $\kappa$  comparable to those observed in marine environments. Both the theoretical predictions and measurements show that the degree to which changes in the ensemble scattering properties occur, increases with increasing  $\kappa$ . These results suggest therefore that knowledge of the size distribution of suspended particles is likely a key input for the inversion of ABS data collected in the marine environment. The next stage in these investigations is to determine if Equations 1 and 2, derived assuming a spherical particle shape, hold for suspensions of irregularly shaped quartz sediments.

#### 5. Acknowledgements

This work was jointly funded by the UK Natural Environment Research Council, as part of its small scale sediment process studies, and by the European HydralabIII-SANDS programme. The authors would like to thank AQUATEC SUBSEA Ltd for the loan of the 0.5 MHz transducer, and also Dr. Richard D. Cooke (Proudman Oceanographic Laboratory) for his assistance in maintaining and repairing the sediment tower.

#### References

- Bale, A.J. and Morris, A.W., 1987. *Estuar. Coast. Shelf Sci.*, 24, 253-263.
- Betteridge, K.F.E., Thorne, P.D. and Cooke, R.D., 2008. *Cont. Shelf Res.*, 28, 227-235.
- Crawford, A.M. and Hay, A.E., 1993. *J. Acoust. Soc. Am.*, 94 (6), 3312-3324.
- Downing, A., Thorne, P.D. and Vincent, C.E., 1995. *J. Acoust. Soc. Am.*, 97 (3), 1614-1620.
- Flammer, G. H., 1962. Geological Survey Bulletin No 1141-A, *United States Government Printing Office*, Washington.

- Hay, A.E., 1991. *J. Acoust. Soc. Am.*, 90 (4), 2055-2074.
- He, C. and Hay, A.E., 1993. *J. Acoust. Soc. Am.*, 94 (4), 2247-2254.
- Hess, F.R. and Bedford, K.W., 1985. *Marine Geology*, 66, 357-379.
- Kaye, G.W.C. and Laby, T.H., 1986. Tables of Physical and Chemical Constants, *Longman*, 477 pp.
- Krank, K. and Milligan, T.G., 1991. Grain size in oceanography. In: Syvitski, J.P.M. (Editor) Principles, methods, and application of particle size analysis. *Cambridge University Press*, pp 332-345.
- Schaafsma, A.S. and Hay, A.E., 1997. *J. Acoust. Soc. Am.*, 102 (3), 1485-1502
- Sengupta, S., 1979. *Sedimentology*, 26, 63-82.
- Sheng, J. and Hay, A.E., 1988. *J. Acoust. Soc. Am.*, 83 (2), 598-610.
- Stavn, R.H. and Keen, T.R., 2004. *Journal of Geophysical Research*, 109, C05005.
- Sval'nov, V.N. and Alekseeva, T.N., 2006. *Oceanology*, 46 (4), 545-556.
- Taylor, J.R., 1997. An Introduction to Error Analysis: The Study of Uncertainties in Physical Measurements, *University Science Books*, California, USA, 328pp.
- Thorne, P.D. and Buckingham, M.J., 2004. *J. Acoust. Soc. Am.*, 116 (5), 2876-2889.
- Thorne, P.D. and Campbell, S.C., 1992. *J. Acoust. Soc. Am.*, 92 (2), 978-986.
- Thorne, P.D. and Hanes, D.M., 2002. *Cont. Shelf Res.*, 22, 603-632.
- Thorne, P.D. and Hardcastle, P.J., 1997. *J. Acoust. Soc. Am.*, 101 (5), 2603-2614.
- Thorne, P.D., Hayhurst, L. and Humphrey, V.F., 1992. *Ultrasonics*, 30 (1), 15-20.
- Thorne, P.D., Manley, C. and Brimelow, J., 1993. *J. Acoust. Soc. Am.*, 93 (1), 243-248.
- Thorne, P.D. and Meral, R., 2008. *Cont. Shelf Res.*, 28, 309-317.
- Thosteson, E.D. and Hanes, D.M., 1998. *J. Acoust. Soc. Am.*, 104 (2), 820-830.



## **Observations Of The Effects Of Turbulence On Particle Size Distributions In An Estuarine Bottom Boundary Layer.**

**AJ Souza<sup>1</sup>, W Thurston<sup>1</sup>**

1. Proudman Oceanographic Laboratory, Liverpool, UK, ajso@pol.ac.uk

Estuarine bottom boundary layers (bbl's) are an area of intense interest to physical oceanographers. It is here that maximum levels of turbulence are found, due to high stress and shear rates. Sediment erosion and deposition also occurs in the bbl. The magnitude of turbulence is critical in determining the vertical flux of suspended particulate matter (SPM) and in the presence of cohesive particles the degree of flocculation as well.

Here we present continuous, concurrent observations of dynamics and SPM performed in the bbl of a macrotidal estuary during a 24 day period. The balance of turbulent kinetic energy is considered, in conjunction with variations in the concentration and size distribution of the SPM and its relationship with the turbulent shear rate. Both the turbulence and the SPM are found to vary over a number of tidal frequencies in addition to exhibiting a tidal asymmetry. Possible explanations for these findings are suggested and their implications considered.



## An assessment of the acoustic scattering properties of suspended sandy sediments and the implications for measuring suspension particle size and concentration.

Peter D. Thorne<sup>1</sup>, Ramazan Meral<sup>2</sup>

1. Proudman Oceanographic Laboratory, Joseph Proudman Building, 6 Brownlow Street, Liverpool, L3 5DA, UK. pdt@pol.ac.uk

2. Kahramanmaras Sutcu Imam University, Faculty of Agriculture, Department of Agricultural, Structures and Irrigation, 46060, Kahramanmaras, Turkey. rmeral@ksu.edu.tr

### ABSTRACT

Multi-frequency acoustics backscattering has been used for over a decade to estimate near-bed profiles of suspended sediment particle size and concentration. Central to obtaining the sediment parameters from the backscattered signal, is a description of the acoustic scattering properties of suspended sediments. Formulations are therefore required for the attenuation and backscattering properties of suspensions of sedimentary particles with size and acoustic frequency. There is no rigorous analytical solution or single formulation for these scattering properties and different researchers have used somewhat different expressions. Here we bring together four decades of published data on the acoustic scattering properties of suspensions of sandy sediments and formulate simple heuristic generic expressions to describe the sediment scattering properties.

### BACKGROUND

The multi-frequency acoustic backscatter systems, ABS, currently in use typically operate in transceiver mode, usually at frequencies in the range 0.5 MHz – 5MHz. They use the differential scattering characteristics of the scatterers with frequency to establish the suspended sediment particle size and concentration. Because ABS's are normally used in transceiver mode, it is the backscattering and attenuating characteristics of the suspended sediment which are required to convert the acoustic measurements into suspended sediment parameters. The relevant acoustic quantities are the backscatter form function,  $f$ , which describes the backscattering characteristics of the particles in suspension, and the normalized total scattering cross-section,  $\chi$ , which describes the attenuating characteristics.

The sphere scattering approach, using the  $f$  and  $\chi$  representation, was first adopted by Sheng and Hay [1] to explain the sediment attenuation observations of Flammer [2]. They used a rigid mobile sphere model which compared reasonably well with the measurements and they also formulated a simple heuristic expression which also provided good agreement with the data. Other publications [3-10] have adopted a comparable approach and presented similar, though somewhat different expressions, related to particular data sets. In this study the objective was to bring together all the published data on acoustic scattering by suspensions of sandy sediments and irregularly shaped particles. The aim being to provide simple expressions for  $f$  and  $\chi$  which compared well with all the data sets available and which can be used with a reasonable degree of confidence, in the interpretation of ABS data collected above sandy sediments.

### SCATTERING EXPRESSIONS

The backscattered signal from a multi-frequency ABS can be converted to concentration,  $M$ , and mean particle size,  $\langle a \rangle$ , using (5,6,8).

$$M = \left\{ \frac{V_{\text{rms}} \Psi \Gamma}{k_s k_t} \right\}^2 e^{4r(\alpha_w + \alpha_s)} \quad k_s = \frac{\langle f \rangle}{\sqrt{\langle a \rangle \rho}}, \quad \alpha_s = \frac{3}{4r\rho} \int_0^r \frac{\langle \chi \rangle M}{\langle a \rangle} dr \quad (1)$$

The above expression assumes the attenuation over a range bin is not substantial [3].  $V_{\text{rms}}$  is the root-mean-

square backscattered signal; this is an ensemble average over a number of backscatter returns.  $r$  is the range from the transceiver,  $\psi$  accounts for the departure from spherical spreading within the transducer nearfield,  $k_s$  and  $\alpha_s$  represent respectively the backscattering and attenuating properties of the sediments,  $\rho$  is the density of the sand grains in suspension,  $k_t$  is a system constant [11],  $\alpha_w$  is the attenuation due to water absorption and the other terms are given below.

$$\langle a \rangle = \int_0^{\infty} aP(a) da \quad (2)$$

$$\langle f(x_o) \rangle = \left\{ \frac{\int_0^{\infty} aP(a) da \int_0^{\infty} a^2 f(x)^2 P(a) da}{\int_0^{\infty} a^3 P(a) da} \right\}^{1/2} \quad (3)$$

$$\langle \chi(x_o) \rangle = \frac{\int_0^{\infty} aP(a) da \int_0^{\infty} a^2 \chi(x) P(a) da}{\int_0^{\infty} a^3 P(a) da} \quad (4)$$

Where  $a$  is the radii of the sediment grains in suspension,  $P(a)$  is the probability size distribution of the grains and  $x=ka$ , where  $k$  is the wave number of the sound in water and  $x_o=k\langle a \rangle$ . The variable  $x$  is non-dimensional and as will be seen below is an appropriate choice for describing the dependency of  $f$  and  $\chi$ . As a step towards the evaluation of equation (1), equations (3) and (4) need to be calculated and this requires expressions for  $f$  and  $\chi$ . The purpose of the present paper is to provide these expressions using all the presently available published data, so that marine scientists and sedimentologists can use them in a straightforward manner in the interpretation of ABS data.

## MEASUREMENTS

*Form function  $f$ .* The first quantitative suspended sediment measurements which were expressed in the form function format were collected on beach sands [3]. Acoustic backscatter measurements from a sediment jet were collected at 1.0 MHz, 2.25 MHz and 5.0 MHz, using sands sieved into  $\frac{1}{4}\phi$  size intervals and covering the radius range 58-231  $\mu\text{m}$ . Following on from these measurements, broadband scattering from the sediment jet were carried [4]. Data were collected on  $\frac{1}{4}\phi$  sieved sand samples with mean radii of 57.75  $\mu\text{m}$ , 98.0  $\mu\text{m}$  and 162.5  $\mu\text{m}$ , covering the frequency band 1.25-2.75 MHz in 0.2 MHz frequency intervals. Further measurements were reported [9] using sands collected from estuarine, beach and quarried locations. Observations were made in a sediment tower which generated a homogeneous suspension of sediments over a vertical range of about 1m. Data were collected over the particle radius range 45-390  $\mu\text{m}$  in  $\frac{1}{4}\phi$  sieved intervals. The acoustic frequencies used were 1.0 MHz, 2.0 MHz and 4.0 MHz. Finally a series of measurements have been published on scattering by single irregularly shaped particles [12]. Measurements were collected on particles in the radius range 0.72-2.5  $\mu\text{m}$  using a broadband system operating between 40-240 kHz and on particles with radius between 0.15-0.2  $\mu\text{m}$  using narrow band signals over the frequency range 0.6-2.2MHz.

*Normalized total scattering cross-section  $\chi$ .* The earliest useful published measurements on attenuation by suspensions of sandy sediments were reported over forty years ago [2]. These data were used [1] to provide the first contemporary description of suspended sediment attenuation using sphere scattering models. The measurements were collected over the radius range 26-455  $\mu\text{m}$ , at six discreet frequencies between 2.5-25.0 MHz at a fixed concentration of 2.65  $\text{kgm}^{-3}$ . Sheng and Hay [1], in their table 2, also presented attenuation data from other studies [13-15], which we have also included here. The next data set is from the suspended sediment jet work [3]. Measurements were made over a range of concentrations nominally between 0.3-24  $\text{kgm}^{-3}$ , using a selection of beach sands sieved into  $\frac{1}{4}\phi$  size intervals, at frequencies of 2.25 MHz, 4.5 MHz and

5.0 MHz. More recent [7] attenuation measurements were made on sandy sediments over the frequency range 2.25-100 MHz using  $\frac{1}{4}\phi$  sieved radii of 11.5  $\mu\text{m}$ , 24.5  $\mu\text{m}$ , 49  $\mu\text{m}$  and 98  $\mu\text{m}$ . Lastly, attenuation measurements were obtained from the gradient of the backscattered signal as part of the sediment tower study [9].

*Combine data sets.* The data from the four studies [3,4,9,12] on the form function for sandy suspensions and irregular shaped particles are shown in figure 1a. The data cover the range  $x=0.2-30$ . In general the observations are similar in form for the different data sets; this is indicative that the non-dimensional scattering parameters used on the abscissa and the ordinate are appropriate for scattering by irregularly shaped

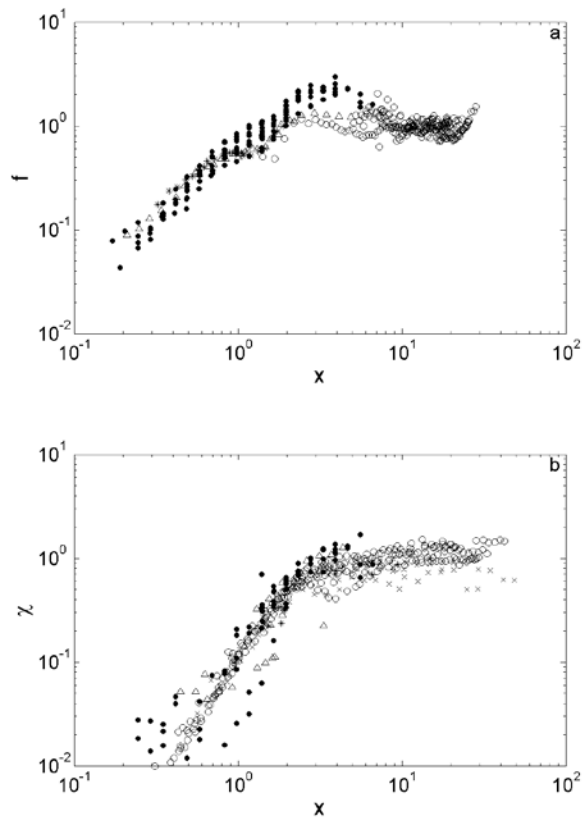


Fig. 1. a) Measurements of the form function,  $f$ , from; [4] (\*), [9] (●) and [12] (○). b) Measurements of the normalized total scattering cross-section,  $\chi$ , from; [2] (x), [1] (\*) (using the data [13-15]), [3] ( $\Delta$ ), [7] (○) and [9] (●).

particles. There is scatter in the data and this is considered to be associated with detailed differences in particle shape [7], different experimental procedures and experimental errors associated with the different data sets. As can be seen in figure 1a, between  $x=0.2-2$  there is seen to be a relatively steady increase in the form function with  $x$ , with the trend being nominally consistent for the different data sets. Above the value of  $x=2$ , the increase of  $f$  with  $x$  is no longer dominant and the data show somewhat less consistency. Above  $x=5$ , the data available is only for single irregularly shaped scatters and the trend is nominally constant as  $x$  increases. The complementary results for the measurements of the normalized total scattering cross-section [1-3,7,9,13-15] are presented in figure 1b. Data were obtained between  $x=0.3-50$ . Again, as with the form function, the different data sets of the normalized total scattering cross-section generally follow a similar trend. The data show increasing values for  $\chi$  with  $x$  up to a value of  $x=2$  and with a gradient steeper than was the case for the form function. Above  $x=2$  the rate of increase of  $\chi$  with  $x$  is significantly reduced and at higher values of  $x$ ,  $x > 10$ ,  $\chi$  appears to be nominally independent of  $x$ .

## FORMULATIONS

The data shown in figure 1 has a degree of scatter associated with the different data sources. To try and obtain the most representative expressions for the data a process of outlier ejection and data smoothing was applied, the details of which are given in [10] and the results are shown in figure 2. The essential form of the curves in figure 1 has been retained with a significant reduction in data scatter.

To represent the measurements, formulae were derived on a heuristic basis and following procedures presented in previous publications [1,6,8]. Asymptotic constraints were imposed such that for  $x \ll 1$ , the Rayleigh regime,  $f \propto x^2$  and  $\chi \propto x^4$  and for  $x \gg 1$ , the geometric regime,  $f$  and  $\chi$  were constant. For the form function the expression used was

$$f = \frac{x^2 \left( 1 - \varphi_1 e^{-((x-x_1)/\zeta_1)^2} \right) \left( 1 + \varphi_2 e^{-((x-x_2)/\zeta_2)^2} \right)}{1 + \delta_1 x^2} \quad (5)$$

For  $x \ll 1$ , the two bracketed terms tend to a constant,  $c_0$ , hence  $f = c_0 x^2$ . For  $x \gg 1$ ,  $f = 1/\delta_1$  which is constant and independent of  $x$ . The first bracket containing the exponential introduces the inflexion region around  $x=1-2$ . Physically this is associated with a back and forth movement of the particles in the water due to the propagating acoustic wave. The second bracket accounts for the observed peak in the form function at approximately  $x=2-4$ , before the onset of the expected constant value for  $f$  at the higher values of  $x$ . The bracketed terms have six independent variables and these were obtained by matching the predictions to the data in the local area where the bracketed terms have maximum influence and then by fine tuning equation (5) to minimizing the mean root-mean-square difference between the predictions and the data. The result was

$$f_e = \frac{x^2 \left( 1 - 0.35 e^{-((x-1.5)/0.7)^2} \right) \left( 1 + 0.5 e^{-((x-1.8)/2.2)^2} \right)}{1 + 0.9 x^2} \quad (6)$$

This simple expression, given by the solid line in figure 2a, captures the essential features of the data; Rayleigh scattering for  $x \ll 1$ , the curvature of the data in the region  $x=1-5$  and constant in the geometric scattering regime. For small values of  $x$ ,  $f_e = c_0 x^2$ , where  $c_0 = 1.25$ . For large  $x$ ,  $f_e = 1.1$ . These asymptotic expressions for  $x \ll 1$ ,  $x \gg 1$ , are respectively given by the dashed and dotted lines in figure 2a.

For the normalized total scattering cross-section the expression below was used, this is similar to the expression used in Ref [1,8].

$$\chi = \frac{\beta_1 x^4}{[\xi_1 + \xi_2 x^\kappa + \beta_2 x^4]} \quad (7)$$

Following the approach taken with the form function, for  $x \ll 1$ ,  $\chi = (\beta_1/\xi_1) x^4$  and  $\beta_1/\xi_1$  was obtained from the low  $x$  values. For  $x \gg 1$ ,  $\chi = \beta_1/\beta_2$ , this was obtained from the data.  $\xi_1$ ,  $\xi_2$  and  $\kappa$  were then adjusted to minimize the root-mean-square difference between equation (7) and the measurements. The result was

$$\chi_e = \frac{0.29 x^4}{[0.95 + 1.28 x^2 + 0.25 x^4]} \quad (8)$$

As shown in figure 3b, the solid line obtained using equation (8) represents all the main features of the data, with close agreement in the Rayleigh, intermediate and geometric regimes. For  $x \ll 1$ ,  $\chi_e = 0.3 x^4$  and for  $x \gg 1$ ,  $\chi_e = 1.16$ , these are respectively shown by the dashed and dotted lines in figure 2b.

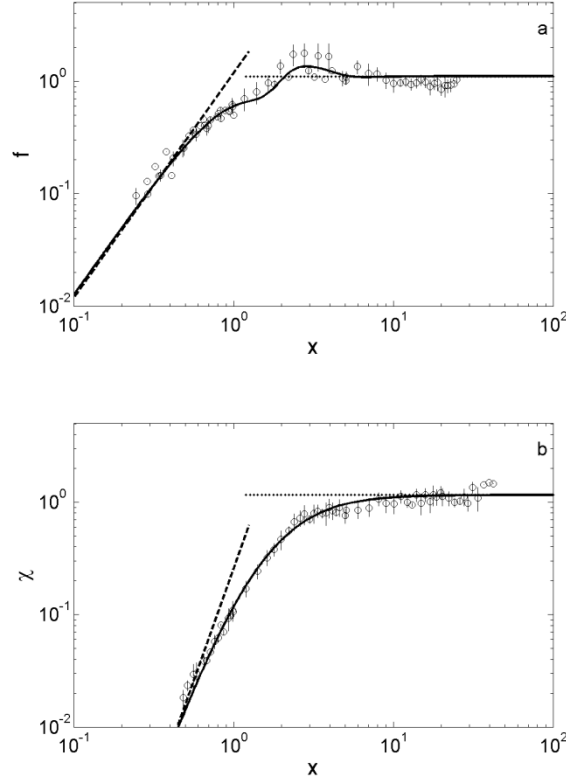


Fig. 2. a) Measurements of the filtered and smoothed form function (o), equation (6) (—), Rayleigh scattering (---) and geometric scattering (.....). b) Measurements of the filtered and smoothed normalized total scattering cross-section (o), equation (8) (—), Rayleigh scattering (---) and geometric scattering (.....).

#### PARTICLE SIZE DISTRIBUTION

Equations (6) and (8) provide the fundamental expressions for  $f$  and  $\chi$  for a suspension of nominally single size; ie with a  $\delta$  size distribution. These formulations for  $f$  and  $\chi$  need to be evaluated using equations (3) and (4) for use in the marine environment, since the suspended sediments will invariably have a broad size distribution. Therefore allowance has to be made for the impact a range of particle sizes have on  $f$  and  $\chi$ . To assess this impact, a log-normal size distributions,  $P_{ln}(a)$ , was used as described in equation (9). The mean

$$P_{ln}(a) = \frac{1}{a\sqrt{2\pi}\zeta} e^{-\frac{(\ln(a)-m_o)^2}{2\zeta^2}} \quad m_o = \ln\left(\frac{\langle a \rangle^2}{\sqrt{\langle a \rangle^2 + \sigma^2}}\right) \quad \zeta = \sqrt{\ln[(\sigma / \langle a \rangle)^2 + 1]} \quad (9)$$

size of the particles in suspension was given by  $\langle a \rangle$  and the standard deviation was set at  $\sigma = \kappa \langle a \rangle$  where for this study we have used  $\kappa=0.5$ . A value of  $\kappa=0.5$  results in  $d_{90}/d_{10} \approx 3$ , which represents a moderately well sorted sediment. Substituting equation (9), with equations (6) and (8), into equations (3) and (4), values for  $\langle f_e \rangle$  and  $\langle \chi_e \rangle$  were calculated and the results are shown in figure 3. The solid line in figures 3a and 3b is  $f_e$  and  $\chi_e$  and the dashed line is  $\langle f_e \rangle$  and  $\langle \chi_e \rangle$ . As seen in figure 3, the introduction of a size distribution impacts on both the form function and normalized total scattering cross-section. In the Rayleigh regime the ratio for  $\langle f_e \rangle / f_e \approx 3$  and for  $\langle \chi_e \rangle / \chi_e \approx 10$ . The impact of the size distribution in this scattering regime is therefore very significant. For the geometric regime the ratios are  $\langle f_e \rangle / f_e \approx 0.8$  and  $\langle \chi_e \rangle / \chi_e \approx 0.65$ . Although these changes are not as significant as in the Rayleigh regime, they are not inconsequential. The results in figure 3 show the importance of having a reasonable estimate for the relative standard deviation,  $\kappa$ . From results presented previously [10], this estimate

may be more important than knowing the precise form of the probability distribution used to represent the particles sizes in suspension.

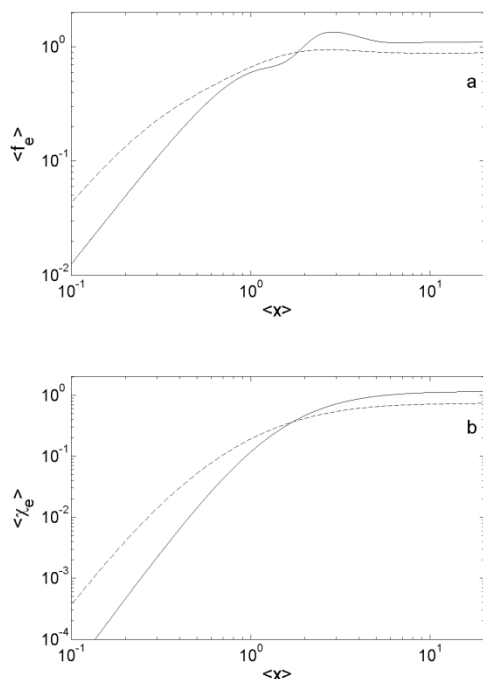


Figure 3. a) Plots of the form function from equation (6),  $f_e$  (-), and from equation (3),  $\langle f_e \rangle$  (---). b) Plots of the normalized total scattering cross-section from equation (8),  $\chi_e$  (-), and from equations (4),  $\langle \chi_e \rangle$  (---). For the evaluation of equations (3) and (4),  $P(a)$  was given by the log-normal distribution in equation (9) with  $\sigma(a)=0.5\langle a \rangle$ .

### CONCLUSION

The present work has sought to provide scattering expressions, for the interpretation of data collected using multi-frequency acoustic backscatter systems over sandy beds. To obtain simple formulations for the scattering properties, all the published data available on scattering by suspensions of sandy sediments were collated. These data have also been augmented by some measurements taken on single irregularly shaped particles. Simple heuristic expressions, in the form of equations (5) and (7) were put forward which encompassed Rayleigh scattering for  $x \ll 1$ , and geometric scattering for  $x \gg 1$ . Using the measurements in the Rayleigh and geometric scattering regimes, some of the constants in the expressions were established. Other constants were obtained by minimizing the root-mean-square difference between the predictions and the observations. This led to the expressions given in equations (6) and (8). To assess the impact a particle size distribution had on  $f_e$  and  $\chi_e$ , equations (3) and (4) were evaluated for a log-normal particle size distributions. The calculations showed the effect was significant particularly when  $x < 1$ . The departure of  $\langle f_e \rangle$  and  $\langle \chi_e \rangle$  from  $f_e$  and  $\chi_e$  were of sufficient magnitude, that the results indicated the effect of having a particle size distribution must be incorporated into acoustic inversions on backscatter data collected in the marine environment.

Finally, the aim of the present paper has been to provide those who use acoustics as a tool for studying sediment transport processes, with simple expressions for the scattering properties of suspensions of sandy sediments. Equations (6) and (8) represent a best fit to the published data available at present, with the constraint of Rayleigh scattering for  $x \ll 1$  and geometric scattering for  $x \gg 1$ . These equations, in conjunction with equation (3) and (4), provide a simple basis for interpreting data obtained using multi-frequency ABS over sandy seabeds.

## ACKNOWLEDGEMENTS

This work was supported by the ONR mine burial programme, the EU HydralabIII programme and NERC, UK. This paper is a précis of the results presented in [10].

## References

- [1] J. Sheng and A.E. Hay, "An examination of the spherical scatterer approximation in aqueous suspensions of sand", *J. Acoust. Soc. Am.* 83, 598-610 (1988)
- [2] G. H. Flammer, "Ultrasonic measurements of suspended sediments", Geological Survey Bulletin No 1141-A, United States Government Printing Office, Washington (1962)
- [3] A. E. Hay, "Sound scattering from a particle-laden turbulent jet", *J. Acoust Soc. Am.*, 90, 2055-2074 (1991)
- [4] C. He and A. E. Hay, "Broadband measurements of the acoustic scattering cross section of sand particles in suspension", *J. Acoust. Soc. Am.* 94(4) 2247-2254 (1993)
- [5] A. E. Hay and J Sheng, "Vertical profiles of suspended sand concentration and size from multifrequency acoustic backscatter", *J. Geophys. Res.* 97(C10). 15661-15677 (1992)
- [6] P. D. Thorne, P. J. Hardcastle, R. L. and Soulsby, "Analysis of acoustic measurements of suspended sediments", *J. of Geophysical Res.*, Vol. 98, No. C1, 899-910 (1993)
- [7] A. S. Schaafsma A. S. and A. E. Hay, "Attenuation in suspensions of irregularly shaped sediment particles: A two-parameter equivalent spherical scatterer model", *J. Acoust. Soc. Am.* 102, 1485-1502 (1997)
- [8] P. D. Thorne P.D. and D. M. Hanes, "A review of acoustic measurement of small scale sediment processes", *Continental Shelf Res.* 22, 603-632 (2002)
- [9] P. D. Thorne and M. J. Buckingham, "Measurements of scattering by suspensions of irregularly shaped sand particles and comparison with a single parameter modified sphere model", *J. Acoust Soc Amer.* 116 (5) 2876-2889 (2004)
- [10] P. D Thorne and R Meral, "Formulations for the scattering properties of sandy sediments for use in the application of acoustics to sediment transport", *Continental Shelf Research*, 28, 309-317 (2008)
- [11] K.F.E. Betteridge, P.D. Thorne and R. D. Cooke, "Calibrating multi-frequency acoustic backscatter systems for studying near-bed suspended sediment transport processes", *Continental Shelf Research*, 28, 227-235 (2008)
- [12] P. D. Thorne, K. R. Waters and T. J. Brudner, "Acoustic measurements of scattering by objects of irregular shape", *J. Acoust. Soc. of Am.*, 97(1), 242-251 (1995)
- [13] R. H. J Jansen, "The in-situ measurement of sediment transport by means of ultrasound scattering. A Delft Hydraulics Laboratory report", The Netherlands, publication number 203, pp13 (1978)
- [14] R. H. J. Jansen, "An Ultrasonic Doppler Scatterometer for Measuring Suspended Sand Transport", in *Ultrasonic International 79*, Conference Proceedings, edited by Z. Novak (Graz, Austria), UI 79, 366-371 (1979)
- [15] A. S. Schaafsma and W. J. G. J. der Kinderen, "Ultrasonic instruments for the continuous measurement of suspended sand transport", *Proceedings of the IHAR symposium on Measuring Techniques in Hydraulic Research* (editor A.C.E Wessels) held at Delft Hydraulics 22-24 April 1985 and published by A. A. Balkema Rotterdam in 1986. 125-136 (1985)



## **Modelling flocculation in sediment transport models: needs for in-situ particle size and settling velocity measurements**

**Romarc VERNEY<sup>1</sup>, Pierre LE HIR<sup>1</sup> and Philippe BASSOULLET<sup>1</sup>**

1. IFREMER, Dyneco-Physed, BP 70, 29280 Plouzané, France ; a. rverney@ifremer.fr

The fate of suspended particulate matter in natural systems depends on their size, shape and density impacting their settling velocity. Since the 1990<sup>th</sup>, experimental works and in situ measurements have revealed that particles characteristics were strongly influenced by flocculation/deflocculation processes. Over the past 20 years, sediment transport numerical models have been improved and refined in terms of processes accounted for. Therefore the need for in-situ calibration and validation data evolved similarly in complexity.

A size-class based flocculation model with explicit aggregation/break-up formulations has been recently developed to account for microflocs/macroflocs dynamics. In this model, the floc population is distributed in 15 classes, logarithmically scaled from 4  $\mu\text{m}$  to 2000  $\mu\text{m}$ . Flocs in each class are characterized by their size, density, volume and mass assuming their fractal distribution, and a given fractal dimension. Aggregation by shear and differential settling are considered while fragmentation is controlled by the shear rate. Computation of flocs settling velocities is performed by applying the Stokes law with the size and density of flocs, and modified to consider hindered settling. This model was successfully applied in 0D and 1DV models and compared to experimental works or other numerical models in terms of suspended sediment concentration, mean diameter, settling fluxes and grain-size distribution. This model will be implemented soon in 3D sediment transport numerical models.

Such models require validation in situ measurements within a tidal cycle: size spectrum and settling velocity every hour, if possible along a fortnightly tidal cycle. and ii) to extend our knowledge on key processes or parameters, such as the floc fractal dimension and its variability, the size spectrum of eroded material/sediment, floc break-up modes, etc.